Insights on the spatiotemporal organization of integrins and their ligands using quantitative biophysical tools

Alberto Sosa Costa

ICFO-Institut de Ciènces Fotòniques
Universitat Poltècnica de Catalunya
Barcelona, 2016

ICFO The Institute of Photonic Sciences

UNIVERSITAT POLITÈCNICA DE CATALUNYA
BARCELONATECH

Education and Culture DG
ERASMUS MUNDUS

euro PHOTONICS
ERASMUS MUNDUS

Thesis supervisor: Prof. Maria Garcia-Parajo (ICREA, ICFO-The institute of Photonic Sciences, Spain)

Thesis Co-Supervisor: Prof. Francesco S. Pavone (LENS-European Laboratory for Non-Linear Spectroscopy, Italy)

Thesis Co-Supervisor: Dr. Carlo Manzo (ICFO-The institute of Photonic Sciences, Spain)

Thesis Committee Members:

1. Dr. Marco Capitanio (LENS-European Laboratory for Non-Linear Spectroscopy, Italy)
2. Dr. Joaquín Teixidó (CIB- CSIC - The Biological Research Center- Spanish National Research Council)
3. Dr. Stefan Wieser (ICFO-The institute of Photonic Sciences, Spain)

Insights on the spatiotemporal organization of integrins and their ligands using quantitative biophysical tools

Alberto Sosa Costa

under the supervision of

Professor María F. García Parajó

Submitted this thesis in partial fulfillment of the requirements for the degree of

DOCTOR

by the

Universitat Poltècnica de Catalunya

Barcelona, 2016

A la memoria de mis dos Haydées

Acknowledgements

Since I started high school I felt a great passion for math. My curiosity about the idea that the world is governed by laws subjected to strict mathematical rules made me decide with no hesitation to further pursue a career in physics. As a physicist I learnt why objects fall, what electricity and magnetism is, the nature of light, and even flirted with quantum mechanics and the relativity theory. However, the complexity and perfection of living organisms remained an exciting and mysterious topic for me. How biologists were able to decipher the different mechanisms at the molecular level that orchestrate life was always intriguing for me. Once more my curiosity made me embark on the long journey of a PhD in biophysics. As in a real boat trip, I have experienced times of storm and apparent calm. Although challenging, it has been an enriching experience from both professional and personal side. Fortunately, I was not alone on the boat, but I was supported by a long crew without which it would have been impossible to succeed in my mission.

I would first like to thank my supervisor Maria for having accepted me to form part of such a multicultural and interdisciplinary group. From the very beginning she was always willing to support me both at the professional and the personal level, so much so that I am pretty sure she was about to ask Fidel Castro about the reasons of my delay in starting the PhD. Indeed, her passion and dedication to science has been a source of inspiration during my PhD. The door of her office was always open to answer doubts of any kind. From the endless meetings with her I learned how to think as a scientist and the effort that this profession demands. From her, I also learned the true meaning of the word “deadline”. I am really grateful for the time she has spent to make me grow as a scientist and for all she has taught me during these four years.

Another key person during my PhD has been Carlo. His capability of analysis and scientific thinking is really admirable to me. From him I have learned from how to align the laser to how to develop complex algorithms for the analysis of experimental data. Indeed, his guidance through these years has been decisive for the success of this thesis. We have not only shared office but also beers, meals and good moments that make me see him as a friend rather than as a colleague.

Otra persona a la que me gustaría agradecer sinceramente es a Merche. Cuando llegué a ICFO, nunca antes había entrado a un laboratorio. Merche fue esa persona que con tono jocoso y a la vez muy profesional me enseñó a sentirme cómodo en el laboratorio de Biología. Le agradezco por ayudarme, cada vez que lo necesité, a encontrar los reactivos que no veía aunque estaban justo en frente de mis narices, por cuidar cautelosamente de mis células, y por siempre sacarme una sonrisa incluso en los momentos de mayor frustración.

I would also like to thank Iza. From the first moment we formed a very good team that allowed us working together for more than two years. Indeed, the long chats during the endless experiments that we performed improved my English a lot. Her meticulousness and endeavor in the work are two qualities that I try to apply every time I enter in the lab.

Thanks a lot the rest of my group, those who are still on board and those who already left. We all have shared moments of ups and downs, successes and defeats, beers and cava. I would specially like to thank Kyra, who I consider as my younger and taller sister, for the discussions on biology, her advice about experiments and for always having a word to cheer me up. Thanks to Thomas, Bruno, Juanito, al francés malo malo (Mathieu), Erik, Pamina, Claude, Félix, Cati, Sarah, and María

También agradezco al Dr. Joaquín Teixidó por sus acertados consejos y fructíferas discusiones sobre biología. Gracias también a Sole por el continuo intercambio de conocimientos que mantuvimos mientras colaborábamos y todavía hoy mantenemos; y por las tediosas pero exitosas jornadas de experimentos. Gracias además a Silvia por su decisivo aporte al éxito del trabajo iniciado con Sole.

I would also like to acknowledge to Prof. Francesco Pavone and his group for their warm welcome at LENS. Grazie mille to Marco Capitanio for the time he devoted to me during my training in LENS and the collaboration that we have maintained afterwards. Thanks to the rest of the group: Lucia, Barbara, Alessia and Ali for making me feel as one of them since the moment I arrived in Florence.

My special thanks to the human resources team (Manuela, Anne, Mery, Laia, Cristina), for always making time to help with bureaucratic issues.

I would also like to thank all the good people I have met during these years at ICFO and with which I have shared more than a single beer: my adopted sister in law Bárbara, Juan Miguel, Miriam, Roland, Lisa, Martha, Miquel, Mark, Chiara, Mick, Pablito, Elsa, Claudia, Idoia, Peter, Rafa and Lukasz.

Por último, me gustaría agradecer a mi familia, que aunque lejos siempre está muy presente en mi vida y a quienes les debo en gran medida la persona que soy hoy en día. Mi más especial agradecimiento, sin dudas, va dirigido a la persona más importante en mi vida, mi gran amor, mi Noslen. Gracias por estar siempre a mi lado, por tu amor incondicional, por quererme incluso aquellos días en los que las células estaban “unhappy”. Juntos, somos el mejor de los equipos. Sin ti, no sólo hubiese sido incapaz de hacer este largo viaje sino que no hubiese tenido el menor sentido ni siquiera comenzarlo.

Table of Contents

Abstract

The migration of leukocytes from the blood stream to sites of injury and infection in the extravascular tissues is fundamental for the immune response. This process is mediated by receptors located at the cell membrane that rapidly respond to the action of chemical stimuli such as chemokines, and mechanical cues such as shear flow. Two of the main receptors involved in such interaction between leukocytes and the lining cells of the blood vessels are αLβ2 and α4β1, both integrins expressed on the leukocyte cell membrane. They bind to their respective ligands ICAM-1 and VCAM-1, both located on the endothelial cell membrane. The dynamic and lateral organization of integrins on the cell membrane has been shown to be crucial in the regulation of cell adhesion. Likewise, the organization of the ligands in small domains (clusters) would likely reinforce the bonds formed with the integrins. Hence, the study of the spatiotemporal behavior of receptors and ligands in the physiological context is crucial for the better understanding of the immune response at molecular level. In this thesis, different state-of-art microscopy techniques have been combined to visualize fast events taking place at the nanometer scale on the T-cell and endothelial cell (EC) membranes. Moreover, the use of different devices for cell mechanical stimulation allowed the simulation of the physiological conditions which cells are normally subjected to in our body. Furthermore, the use and development of new computational algorithm for extracting image features and data analysis has been decisive in this thesis.

In **Chapter 1**, the different steps of the leukocyte migration process and the main receptors involved in each of these steps are described. Then, the main characteristic of integrins with special emphasis on αLβ2 and α4β1 are also discussed. Moreover, a short review of the more recent microscopy techniques achieving high temporal and spatial resolutions is presented. In addition, an overview of the different biophysical tools used to mechanically stimulate the cells highlighting their main advantages and drawbacks, is also presented. Finally, the general methodology and the specific computational algorithms used for the analysis and quantification of images obtained using microscopy techniques are described.

In **Chapter 2**, we describe two of the main microscopy approaches used in this thesis, namely Stimulated Emission Depletion (STED) and Single Particle Tracking (SPT). Their working principles, main set-up characteristics, sample preparation conditions, and the methodology used to analyze the output data, are also described. Moreover, a custom-made stretching device and a parallel plate flow chamber, both used to exert mechanical forces on cells, are characterized. We further validate the performance of our SPT set-up on the stretching device by recording the lateral mobility of αLβ2 integrins before and after isotropic cell stretching. The results of these experiments showed an increase in the percentage of αLβ2 molecules immobilized and a decrease in the diffusion coefficient of the remaining mobiles as a consequence of mechanical force.

In **Chapter 3**, we describe the development of PLANT (Piecewise Linear Approximation of Noisy Trajectories), a segmentation algorithm for the detection of changes of slopes in curves affected by a Gaussian noise. We first describe the advantages and drawbacks of the method, explain the algorithm and then present a quantitative assessment of its performance obtained through extensive numerical simulations. By means of these simulations, we could address all the relevant parameters affecting the algorithm performance, including segment length, slopes and noise. Moreover, we empirically found the functional dependence of the power of detection on the slopes and the length of the segments composing the traces under analysis. Finally, we apply our algorithm on experimental data obtained from tracking individual lymphocytes migrating on ECs under the presence of a continuous shear flow. From the reconstructed traces we derived quantitative parameters such as migration velocity and the time of interaction between consecutive changes of velocities. The implementation of such an algorithm has enabled the analysis of the migratory response of leukocytes on mechanically stimulated endothelial cells, which is the major subject of Chapter 4.

In **Chapter 4**, we study the role of shear forces on the lateral distribution of ICAM-1 ligands on the endothelial cell membrane and their implications on the leukocyte migration. We showed that exposure of ECs to continuous shear flow caused a global redistribution of ICAM-1 to the up-stream of the flow. Moreover, shear flow induced a three-fold increase in ICAM-1 nanoclustering as compared to cells that were not previously subjected to shear stress. This ICAM-1 redistribution was probably driven by the actin cytoskeleton as confocal and STORM images revealed the formation of patch-like actin structures enriched with ICAM-1 upon shear flow stimulation. Moreover, perturbation of actin cytoskeleton using Cytochalasin D led to the suppression of the shear flow induced ICAM-1 nanoclusters. Furthermore, using the algorithm developed in Chapter 3 we quantified the mean velocity and the mean interaction time of T-cells migrating across ECs in the presence of shear flow. We demonstrated that in average T-cells move faster and interact for shorter period of times on ECs that were previously subjected to shear flow as compared to ECs no exposed to the flow. We rationalize these results on the basis of the motor-clutch model, according to which the strengthening of the clutches (αLβ2-ICAM-1 bonds) increases the velocity of the cell while stiffer substrates will induce early break of the clutches. We hypothesize that both conditions are fulfilled in our case as we show that shear flow increases both the clustering of ICAM-1 and its association with the actin cytoskeleton. While the first reinforces the strength of the clutches, the second increases the effective local stiffness due to the stronger anchorage to the cytoskeleton. Thus, the changes observed in leukocyte migration might indeed be the result of the spatial redistribution of ICAM-1 brought about by shear flow stimulation.

In **Chapter 5**, we investigate how the spatiotemporal behavior of α4β1 is affected by the stimulation with chemokines and/or ligands. We first showed a reduction of α4β1 lateral mobility together with a significant and transient increase in the percentage of integrins immobilized on the cell membrane upon CXCL12 stimulation. This increase in the number of α4β1 molecules immobilized was directly correlated with the activation of the integrin and recruitment of talin. Moreover, the addition of VCAM-1 in solution potentiated the effect of CXCL12 as it increased the percentage of integrins immobilized. Furthermore, immobilization of VCAM-1 led to a massive reduction in the mobility of α4β1, comparable to that induced by Mn^{2+}, a potent integrin activator. Confocal and superresolution images demonstrated that the nano-scale organization of primed α4β1 integrins remains unaffected upon chemokine and /or ligand addition. Finally, in **Chapter 6** we discuss the most important findings of this thesis and provide future directions to deepen and further extend the results obtained during this research.

Resumen

La migración de leucocitos desde el torrente sanguíneo a sitios de lesión e infección en los tejidos extravasculares es fundamental para la respuesta inmune. Este proceso está mediado por receptores localizados en la membrana celular que responden rápidamente a la acción de estímulos químicos, tales como quimioquinas y a señales mecánicas, como los flujos de cizallamiento. Dos de los principales receptores involucrados en la interacción entre leucocitos y las células que recubren los vasos sanguíneos son las integrinas αLβ2 and α4β1, las cuales se expresan en la membrana celular de los leucocitos. Ambas integrinas se unen a sus respectivos ligandos ICAM-1 y VCAM-1, los cuales se localizan en la membrana de las células endoteliales. Se ha demostrado que la dinámica y la organización lateral de las integrinas sobre la membrana celular son cruciales en la regulación de la adhesión celular. Asimismo, es muy probable que la organización de los ligandos en pequeños dominios (*clusters*) refuerce los enlaces formados con las integrinas. Por lo tanto, el estudio del comportamiento espacio-temporal de las integrinas y sus ligandos, en el contexto fisiológico, es crucial para una mejor comprensión de la respuesta inmune a nivel molecular. En esta tesis se han combinado diferentes técnicas de microscopía de última generación para visualizar eventos muy rápidos que tienen lugar a escala nanométrica en la membrana de las células T y las células endoteliales. Por otro lado, el uso de diferentes dispositivos para la estimulación mecánica de las células nos ha permitido emular las condiciones fisiológicas de flujo sanguíneo a las cuales las células de nuestro cuerpo están normalmente expuestas. También ha sido decisivo en esta tesis el uso y desarrollo de nuevos algoritmos computacionales, para la extracción de rasgos característicos de las imágenes y para el análisis de datos.

En el **Capítulo 1**, se describen los diferentes pasos en el proceso de migración leucocitaria y los distintos receptores implicados en cada uno de estos pasos. Luego se discuten las principales características de las integrinas, haciendo especial énfasis en αLβ2 y α4β1. Además se presenta una breve reseña de las técnicas de microscopía más recientes, capaces de proporcionar excelente resolución temporal y espacial. Adicionalmente, también se presenta una descripción general de las diferentes herramientas biofísicas usadas para estimular las células, mecánicamente, resaltando sus principales ventajas e inconvenientes. Por último, se describe la metodología general y los algoritmos computacionales específicos usados para el análisis y la cuantificación de las imágenes obtenidas por medio de diferentes técnicas de microscopía.

En el **Capítulo 2**, se describen dos de las principales técnicas de microscopía usadas en esta tesis, a saber STED y SPT. También se describen sus principios de funcionamiento, las principales características de sus correspondientes montajes experimentales, las condiciones de preparación de las muestras y la metodología usada para analizar los datos resultantes en cada caso. Además se caracteriza un dispositivo de estiramiento celular hecho a medida y una cámara de flujo de placa paralela, ambos usados para ejercer fuerzas mecánicas sobre las células. Posteriormente, se valida el desempeño de nuestro equipo de SPT en combinación con el dispositivo de estiramiento, registrando la movilidad lateral de la integrina αLβ2 antes y después de estirar las células isotrópicamente. Los resultados de estos experimentos mostraron un aumento en el porcentaje de moléculas αLβ2 inmovilizadas y una reducción en el coeficiente de difusión de las restantes móviles, como consecuencia de las fuerzas mecánicas.

En el **Capítulo 3**, se describe el desarrollo de PLANT (Aproximación lineal por tramos de trayectorias ruidosas), un algoritmo de segmentación para la detección de cambios de pendientes en curvas afectadas por ruido Gaussiano. Primero se explica el algoritmo y se describen sus ventajas e inconvenientes, y luego se evalúa, cuantitativamente, su rendimiento mediante exhaustivas simulaciones numéricas. Por medio de estas simulaciones hemos podido encontrar todos los parámetros relevantes que afectan el rendimiento del algoritmo, como la longitud de los segmentos, las pendientes y el ruido. Además, se encontró, empíricamente, la dependencia funcional del poder de detección del algoritmo con los valores de las pendientes y las longitudes de los segmentos de las trazas analizadas. Finalmente, el algoritmo se aplicó a datos experimentales obtenidos al rastrear la migración de linfocitos individuales sobre células endoteliales bajo la acción de un flujo continuo. De las trazas reconstruidas se obtuvieron parámetros tales como la velocidad de migración y el tiempo de interacción entre consecutivos cambios de velocidad. La implementación de este algoritmo permitió el análisis de la respuesta migratoria de leucocitos sobre células endoteliales mecánicamente estimuladas, lo cual constituye el tópico principal del Capítulo 4.

En el **Capítulo 4**, se estudia el rol de las fuerzas de cizallamiento en la distribución lateral de los ligandos ICAM-1, localizados en la membrana de las células endoteliales, y sus implicaciones en la migración de leucocitos. Se mostró que la exposición de las células endoteliales a un flujo continuo causa una redistribución global de ICAM-1 en el sentido contrario al flujo. Además el flujo incrementó tres veces el grado de *nanoclustering* de ICAM-1 comparado con células que no fueron previamente sometidas a estrés mecánico. Esta redistribución de ICAM-1 fue probablemente dirigida por el citoesqueleto de actina, ya que imágenes de confocal y de STED revelaron el surgimiento de estructuras de actina en forma parches, enriquecidas con ICAM-1, tras la estimulación con flujo. Además, la perturbación del citoesqueleto de actina usando Citocalasina D condujo a la supresión de los *nanoclusters* de ICAM-1 inducidos por el flujo. Adicionalmente, usando el algoritmo desarrollado en el Capítulo 3, se cuantificó la velocidad media y el tiempo medio de interacción de las células T durante su migración sobre las células endoteliales, en presencia de flujo. Así, se demostró que, en promedio, las células T se mueven más rápido e interactúan por períodos de tiempos más cortos sobre células endoteliales que han sido expuestas a un flujo de cizallamiento, en comparación con células que no han estado sujetas a tal flujo. Estos resultados han sido racionalizados sobre la base del modelo de motor-embrague, de acuerdo con el cual, el fortalecimiento de los embragues (enlaces de αLβ2-ICAM-1) aumenta la velocidad de la célula, mientras que la rigidez del sustrato induce la ruptura temprana de los embragues. Nosotros hipotetizamos que ambas condiciones se satisfacen en nuestro caso, ya que anteriormente mostramos que el flujo aumenta el *clustering* de ICAM-1 y su asociación con el citoesqueleto de actina. Mientras que el primero refuerza los embragues, el segundo aumenta la rigidez efectiva local debido a un anclaje más fuerte al citoesqueleto. Por lo tanto, los cambios observados en la migración de los leucocitos podrían ser, seguramente, el resultado de la redistribución espacial de ICAM-1 provocada por la estimulación mecánica con flujo.

En el **Capítulo 5**, se investiga cómo el comportamiento espacio-temporal de α4β1 es afectado por la estimulación con quimioquinas y/o ligandos. Primero se mostró una reducción en movilidad lateral de α4β1 junto con un aumento significativo y transitorio en el porcentaje de integrinas inmovilizadas en la membrana celular tras la estimulación con CXCL12. Este aumento en el número de moléculas de α4β1 inmovilizadas estuvo directamente correlacionado con la activación de la integrina y el reclutamiento de talina. Por otro lado, la adición de VCAM-1 en solución potenció el efecto de CXCL12, ya que aumentó el porcentaje de integrinas inmovilizadas. Además la inmovilización de VCAM-1 provocó una reducción masiva en la movilidad de α4β1, comparable a la inducida por Mn^{2+}, un potente activador de las integrinas. Imágenes de confocal y de superresolución demostraron que la organización a nano-escala de integrinas α4β1 activadas no se afecta tras la estimulación con quimioquinas y/o ligandos. Por último, en el **Capítulo 6** se discuten los hallazgos más importantes de esta tesis y se proporcionan orientaciones futuras para profundizar y ampliar los resultados obtenidos durante esta investigación.

Chapter 1

Introduction & General review in the field

Migration of leukocytes out of the circulatory system is a crucial process for the proper response of the immune system. Their “trek” across the lining cells of blood vessels is mediated by integrins, whose adhesiveness is rapidly modulated in response to mechanical cues provided by cell´s physiological environment, such as shear flow. In this introductory Chapter the different stages of the process of leukocyte migration are described, followed by an overview on the main properties of integrins receptors, with a particular emphasis on α4β1 and αLβ2 integrins. Then, a general overview of the different techniques developed to mechanically stimulate cells, such as shear flow and stretching devices, is presented. Next, state-of-the-art advanced fluorescent techniques such as single particle tracking and super-resolution microscopy are described. Finally, a general review of the main computational algorithms developed to analyze and quantify image data, is also presented.

1.1 The leukocyte migration process

A broad range of phenomena in health and disease are governed by cell adhesion and migration. When properly regulated, adhesion/migration enables morphogenesis, host defense and tissue healing (1, 2). However, when regulation fails, adhesion and/or migration mediate devastating pathologies such as cancer, autoimmune diseases and chronic inflammation (2-4). A clear example of the importance of adhesion and migration regulation is the firm arrest of circulating leukocytes and their extravasation to sites of inflammation and lymphoid tissues, both processes being crucial for correct regulation of the immune response.

An essential requirement to initiate the process of leukocyte extravasation is the activation of endothelial cells (ECs) lining blood vessels next to the sites of tissue injury or infection (5). This is achieved by the action of chemical signals such as cytokines (e.g., interleukin-1b [IL-1b] and tumor necrosis factor [TNF]) and endotoxin (e.g., histamine and PAF) that are released in response to inflammatory stimuli (6). These chemical signals induce upregulation of adhesion molecules on the EC surface that are involved in initiating rapid attachment of leukocytes to blood vessels. Under these favorable conditions leukocytes undergo a series of sequential but overlapping steps (termed the leukocyte-adhesion cascade) that ends with their extravasation (**Fig. 1.1)** (5, 7).

The different steps are primarily mediated by the concomitant action of cytokines and two major adhesion receptor families: selectins (expressed on leukocytes and ECs) and integrins (on leukocyte side) that bind to their respective counter-receptors on the opposite side. Initially, leukocytes are captured under flow on the inflamed endothelium in a process known as *tethering* that is followed by the *rolling* of leukocytes on the ECs (**Fig. 1.1)**. During the step of rolling, leukocytes slow down their speed through a dynamic process that requires the continuous formation and rupture of bonds. These two initial steps are mediated by the transient interaction between the glycoconjugates expressed on leukocytes and selectins on ECs (primarily E- and P-selectin) (8, 9). The exceptionally high on- and off-rate of the interactions between selectins and their ligands enable leukocytes to adhere to endothelium under blood flow conditions (10). Furthermore, the catch bond character of selectins strengthens each bond as shear stress is applied (11). In addition, it has been described that some integrins like α4β1 and α4β7 may also participate in the tethering and rolling of leukocytes (12, 13).

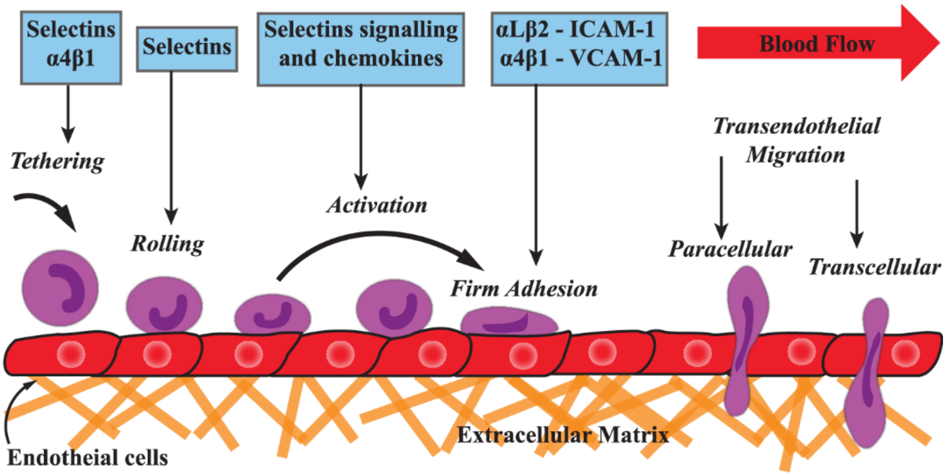

Figure 1.1 The leukocyte adhesion cascade. The main steps in the process of leukocyte migration are schematically depicted. Each step is mediated by the interaction between specific molecules on leukocytes and their counter-receptors on endothelial cells (blue boxes). Adapted from (7).

The decreased speed of leukocytes during rolling allows their interaction with chemokines present in the endothelium, such as CCL21, CXCL12 and CXCL13 (14-17). Chemokines, located on the apical surface of ECs, bind to G-protein-coupled receptors (GPCRs) present on the leukocyte membrane (18-20). Activation of these receptors triggers an intracellular signaling cascade that leads to activation of leukocyte integrins (inside-out signaling), which play a key role in the *firm adhesion* of leukocytes to the endothelium (**Fig. 1.1)** (14, 21). This process is crucial as circulating leukocytes maintain their integrins in an inactive state of low affinity, so the affinity of these molecules should increase to strengthen leukocyte adhesion (22). The inside-out signaling takes place under physiological conditions within a fraction of a second, which translates into an increase in firm adhesion of leukocytes on the vascular endothelium (22). Two of the most relevant integrins mediating such adhesion are α4β1 (VLA-4) and αLβ2 (LFA-1) which interact with the immunoglobulin superfamily molecules VCAM-1 and ICAM-1, respectively (23). The adhesion of leukocytes on the luminal endothelium may be reversible, i.e., if leukocytes stop receiving chemical signals that stimulate their transendothelial migration, they can return to the bloodstream (5). When receiving the proper signals, leukocytes polarize and migrate across the endothelium following a gradient of chemoattract factors. Transmigration or diapedesis across the endothelium is the final step in the process of leukocyte migration to sites of inflammation and can be performed via *paracellular*, or sometimes even via *transcellular* (**Fig. 1.1**) (5, 7).

Despite an ever increasing understanding on the inner workings of cell biochemistry regulating cell adhesion and migration in the immune system, very little is known about mechanical aspects of cell adhesion and mechanotransduction in the context of immunology. Although leukocytes are subject to high shear-stress conditions and constant changes on cell contractility during homing with other cells, little is known on how physical factors are sensed and produce appropriate responses to regulate cell adhesion *in-vivo*.

1.2 Integrins

As mentioned above, integrins are receptors that mediate leukocyte adhesion and migration, by binding to specific ligands located in the extracellular matrix, on the cell surface or in solution. They constitute a large family of heterodimeric transmembrane proteins composed of two non-covalently associated α and β subunits with large extracellular domains, single spanning transmembrane domains and short cytoplasmatic domains. In humans, 18 alpha and 8 beta subunits have been identified that combine to form at least 24 different heterodimers (24, 25). Despite the general structure of all integrins is similar, half of α subunits have an inserted I-domain (also called A-domain) in the ligand binding site (e.g. αLβ2) that is absent in the other 9 α subunits (e.g. α4β1). In the integrins without the I-domain, ligands bind to the junction where α and β subunits connect (**Fig. 1.2**).

Adhesion capacity of a single receptor to its ligand in solution defines the affinity of integrins. On basal conditions integrins interact with their ligands with rather low affinity. Hence, in order to increase the binding affinity, integrins must undergo extensive structural and topological changes. At least three different conformational states that differ in ligand binding affinity have been reported, namely the bent, extended closed headpiece and extended open headpiece conformation (**Fig. 1.2**) (26). They respectively have a low, intermediate and high affinity for their ligands. However, small perturbations induce integrins to continuously transit among the different conformations. Thus, each conformational state must be understood as a dynamic equilibrium rather than a static and immutable state.

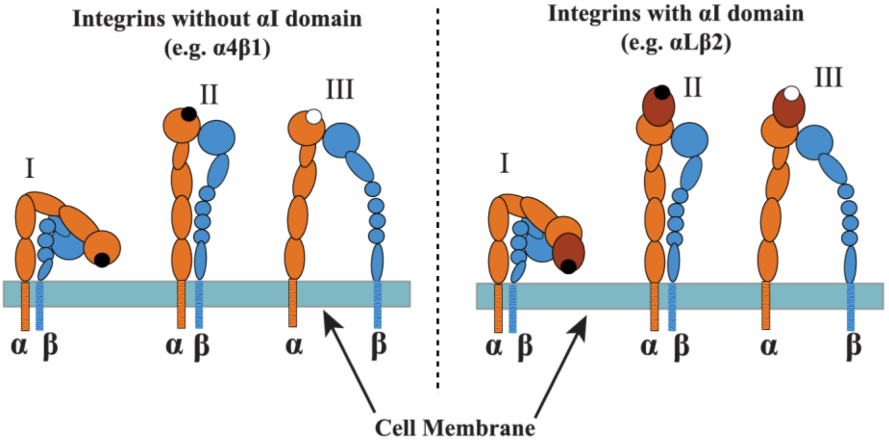

Figure 1.2 Integrins structure. Different conformational states of integrins with (right panel) and without (left panel) the αI domain, are associated to the degree of affinity to their ligands: I) Bent conformation (low affinity), II) Extended closed headpiece (intermediate affinity) and III) Extended open headpiece with cytoplasmatic tails separated (high affinity). Adapted from (27).

The activation of integrins inducing their high affinity state is a bidirectional process that can be regulated either via intracellular (*inside-out*) or extracellular stimulation (*outside-in*). In the first case, signaling is triggered by stimulation of cell surface receptors, as T cell receptor (TCR), B cell receptor (BCR) or chemokine receptors. In the case of chemokines it is known that they induce, within seconds, the extension of previously bent integrins and opening of the ligand binding site resulting in an affinity increase (28). Moreover, interactions of proteins such as talin and kindlin with specific cytoplasmic motifs on the β tail subunit represent a critical step for inside-out integrin activation. These proteins contribute to stabilization of the extended conformation of the integrin by providing a connection with the actin cytoskeleton through the cytoplasmatic β tail. On the other hand, binding of integrins to their ligands or exposure of cells to PMA (phorbol 12-myristate 13-acetate) or ions (such as Mn^{2+}, Mg^{2+} or Ca^{2+}) results in the transmission of information into the cell by outside-in signaling. While some models suggest that ligand by itself is not able to bring the integrin to the extended conformation, others suggest that extension of integrins occur upon ligand binding (29, 30). Nevertheless, both models agree with the notion that conformational changes in the integrin headpiece facilitate ligand binding. Furthermore, chemokine-induced integrin activation facilitates binding to its ligand. Thus, despite inside-out and outside-in signaling processes are conceptually distinct, they concurrently cooperate to increase integrin affinity for the ligand and to stabilize and prolong the arrest of circulating leukocytes.

Besides affinity, integrin adhesiveness is also regulated by its avidity which depends on the cooperative binding strength of a multitude of receptors. Organization of integrins in clusters increases the lifetime of integrin/ligand bonds formed and facilitates the formation of new ones, thus strengthening integrin adhesion and thereby their avidity. However, whether integrin clustering precedes ligand binding or is a consequence of it remains controversial (31-33). Whatever is the case, the formation of clusters requires integrins to move laterally on the plasma membrane. Indeed, it has been shown that integrins exhibit different diffusion behaviors on the cell membrane. Moreover, different studies strongly suggest a tight correlation between affinity and lateral mobility of αLβ2 integrin (34-36). Furthermore, lateral mobility might also facilitate the integrin encounter with its ligand on the opposing surfaces.

Mechanical forces likely provide an additional regulatory mechanism for integrins adhesion. In fact, it has been shown that mechanical signals that involve the combination of force from shear flow and immobilized chemokines tightly regulates firm integrin adhesiveness on T cells (37). Moreover, shear flow is necessary to reinforce selectin bonds that support initial tethering of T-cells to endothelium. On the other hand, measurements of αLβ2/ICAM-1 bond kinetics showed that small pulling forces enhance αLβ2 affinity (38). Furthermore, F-actin flow might also provide mechanical forces contributing to αLβ2 activation and ICAM-1 binding at the immunological synapse interface (39). Thus, fundamental understanding on the spatio-temporal organization of cell adhesion receptors in response to external forces and local geometry changes of the surrounding is crucial for advancing our understanding on immune-related diseases providing a rationale for the development of advance immunotherapy approaches.

1.3 Mechanical manipulation tools

Besides cells of the immune system that are continuously subjected to shear stress, all the cells in our body are exposed to mechanical cues to a lesser or greater extent. The extracellular matrix (ECM) is the primary environment with which cells interact and thus, their mechanical properties, such as matrix stiffness strongly influence cell fate. Cells test the mechanical properties of their surrounding ECM using different mechanosensory proteins and cellular structures, being integrins one of the most important molecules. Mechanosensors, such as integrins, convert physical stimuli to biochemical signaling that convey information from the outside to the cell interior. To better understand the underlying mechanisms of cell mechanosensing and mechanotransduction, it is desirable not only to mimic the mechanical environment experienced by cells *in-vivo* but also to measure the forces exerted by cells on their surroundings. Multiple cell manipulation techniques that ideally suit this purpose have emerged and/or improved in the last two decades. Although some of these techniques are preferred to either exert forces on cells or to measure the forces exerted by cells, many of them can be used indistinctly for both purposes. Below we described some of the main techniques systematically used to study the molecular basis of cellular mechanotransduction.

The classical and probably the oldest technique used in cell mechanics is the micropipette aspiration. Its origins date back to 1954 when it was first used to measure elastic properties of sea urchin eggs (40). In this technique a pipette glass is used to aspire cellular material (**Fig. 1.3A**). By measuring the volume of cell outside and inside the pipette and taking into account the value of the applied vacuum pressure, different physical properties as cell elasticity and viscosity can be calculated (41). Its wide range of suction pressure (from 0.1 to ~10^5 pN/µm^2) and forces (from 10 pN to 104 nN) along with its low cost and easy implementation, it continues to be an important experimental tool for studying the mechanics of cells nowadays (41).

The development of nano- and microfabricated substrates with different geometrical and elastic properties is probably one of the simplest and more versatile approaches for cell mechanics experiments. This method enables to manipulate the lateral organization of the ECM proteins (**Fig.1.3B**) which in turn controls the distribution of forces on the cell membrane. The technique relies on the fabrication of substrates formed by "islands" of ECM components surrounded by nonadhesive regions (**Fig. 1.3C**). To create such "islands", an elastomeric mold is prepared by casting a liquid prepolymer of an elastomer against a master (usually fabricated by applying photolithography on a silicon wafer) with a pattern relief structure (**Fig.1.3D**) (42, 43). The elastomeric mold, usually made of poly-dimethylsiloxane (PDMS), is then coated with the desired protein and stamped to the surface of a substrate. The resulting patterns can have multiple shapes and their sizes can be as small as 100 nm over areas as large as ~1 m^2 (44). In addition, the stiffness of the substrate itself can be easily manipulated by using elastomer materials with variable degree of cross-linking (45). Hence, the stiffness of the substrate can be adjusted to values that range from 1kPa to ~100kPa (45, 46). Another related approach that not only enables to modify the rigidity of the substrate but also allows the direct measurement of traction forces exerted by the cells, is the fabrication of micropost array substrates (**Fig. 1.3E**) (47). By modifying the geometry, density and Young´s modulus of the microposts, the traction forces exerted by the cells can be modulated (48).

Taking advantage of the elastic properties of elastomer substrates, different devices has been designed to mimic the mechanical stress experienced by cells in *in-vivo* conditions. By using such devices, cells can be stretched in many different directions so that they can experience similar stresses and forces that would be present in the body. Thus, numerous cell stretching devices has been developed to apply strain in one direction (uniaxial), in two directions (biaxial), or equal strain in all directions (equibiaxial) (**Fig. 1.3F**). In this technique, force is

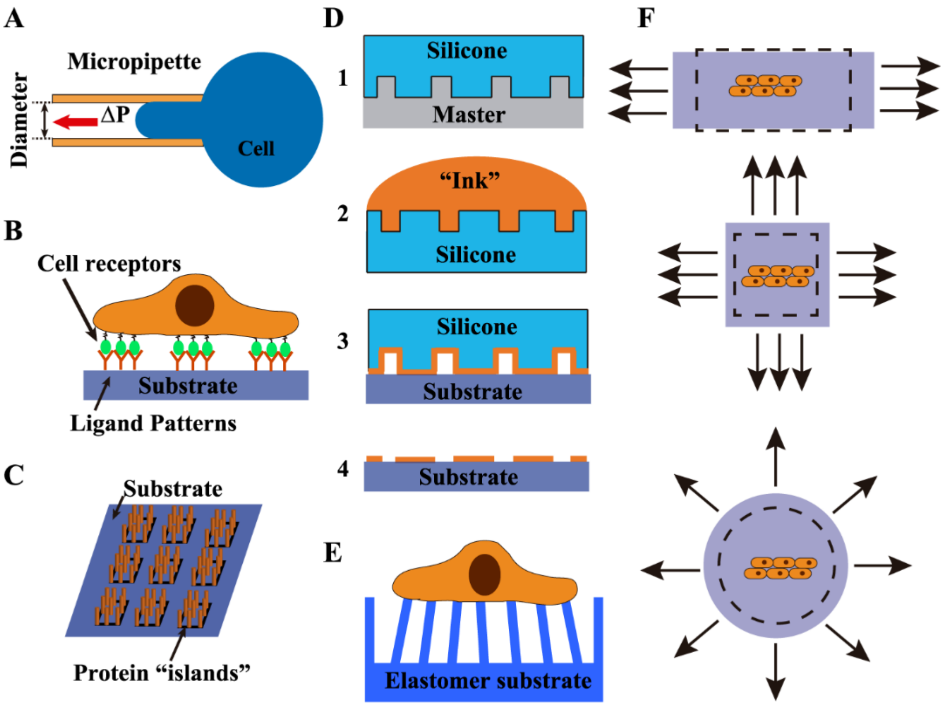

Figure 1.3 Techniques to exert and/or sense mechanical forces (Part I). (A) Micropipette aspiration: the force exerted on the cell membrane is proportional to the vacuum pressure; their inner tip diameters can range from 0.1 to 10 microns. **(B)** Lateral view representation of a cell spread on a patterned substrate. Controlling the distribution of ECM proteins modifies the lateral organization of receptors on the cell membrane, which in turn affects the spreading of the cell. **(C)** Schematic top view of a patterned substrate using microcontact printing technique. The size and shape of the proteins islands can be controlled at the nanometer scale. **(D)** Different steps in the microcontact printing process to create pattern substrates of different stiffness: A silicone mold is first fabricated from a master wafer (1). The mold is then coated with an "Ink" substance –usually a protein of the ECM - (2) and carefully stamped on the substrate (3) to finally obtain the patterned surface (4). **(E)** Micropost arrays: the traction forces exerted by the cells during the spreading (arrowheads) deflect the elastic microposts from their original positions, which in turn can be later used to calculate the magnitude of such forces. **(F)** Possible substrates stretching configurations: uniaxial (upper drawing), biaxial (central drawing) or equibiaxial (lower drawing).

transmitted to cells cultured -on an elastic membrane coated with an ECM protein- by stretching the underlying substrate. A variety of actuation systems including piezoelectric, electromagnetic, and pneumatic actuators have been used to control the stress of the substrate (49). The last one is probably the type of actuator most widely used due to its advantages such as simple setup, homogeneous strain actuation and not direct contact with the cells and /or the medium. Besides a few cell stretching systems available commercially, e.g. Flexcell (Flexcell International Corporation), Strex Systems for cell stretching (STREX Inc.) and ElectroForce (Bose Corporation), several other custom made stretching devices have been reported over the past decade (50-53). In Chapter 2 we describe in detail a custom made stretching device, based on pneumatic control, used in this thesis.

Since an important number of different cells in our body are subjected to fluid flow, another important set of devices for cell mechanics manipulation are those based on shear stress control. Three of the most used shear flow devices are the cone-and-plate system, the parallel plate flow chamber (PPFC), and microfluidic devices. Depending on the specific features of each device, they can generate different flow profiles, namely, laminar, transitional or turbulent flow. The physical magnitude that determines the different flow regimes is the Reynolds number (Re) (54). This dimensionless number is defined as the ratio of inertial forces to viscous forces and ultimately depends on the properties of the medium used (density, viscosity and velocity) and the geometry of the device. Hence, a fluid with $Re<2300$ is considered to be laminar and a flow with $Re>4000$ is defined as turbulent, otherwise ($2300<Re<4000$) the flow is said to be transitional. Manipulation shear flow devices are usually designed so that $Re < 100$ to ensure laminar streams as observed in physiological conditions (55). The cone-and-plate system is based on the geometry of a device commonly employed as viscometer (56). An inverted cone is placed on top of the surface of a plate where the cells are cultured in such a way that the cone axis in perpendicular to the plate (**Fig. 1.4A**). Depending on the cone taper and the angular velocity of the cone with respect to its axis, a wide range of shear stresses can be achieved (57). Alternatively, in a PPFC the fluid surrounding the cells moves by the action of a pressure difference between the inlet and outlet openings of a closed chamber formed by two parallel plates separated by a spacer gasket (**Fig. 1.4B**). This pressure difference can be achieved either via gravitational fluid flow or by using a fluid pump. Due to the much simpler geometry of the PPFC as compared to the cone-and-plate device, the first one provides a more stable laminar flow (58). A wide variety of PPFCs including pump perfusion systems can be found commercially available. In the next Chapter, we describe a commercial PPFC that we used in this thesis.

Other versatile types of devices, initially targeted at biomedicine applications, and that also allow flow control are the microfluidic devices (59). They consist of a micro-channel network with various inlet and outlet ports as well as flow control systems as pneumatic valves mixers and pumps. The diameters of the individual channels can be different and may range from 5 to

500µm (**Fig. 1.4C**). The value of Re can be finely tuned in each separately channel to obtain different shear flow regimes. In general, microfluidic devices can be fabricated by using silicon, glass or polymer materials. However, polymers like PDMS are usually preferred due to their good optical (transparent down to 230nm) and mechanical (flexible) properties together with their low cost (60). The fabrication process is based on soft lithography techniques, similar to that described above for creating micropatterned substrates (61). Some of the advantages of this type of devices are: reduction of sample and reagent consumption (10^{-9} to 10^{-8} litres), increase of automation thus reducing the analysis time, and detections with high resolution and sensitivity (62).

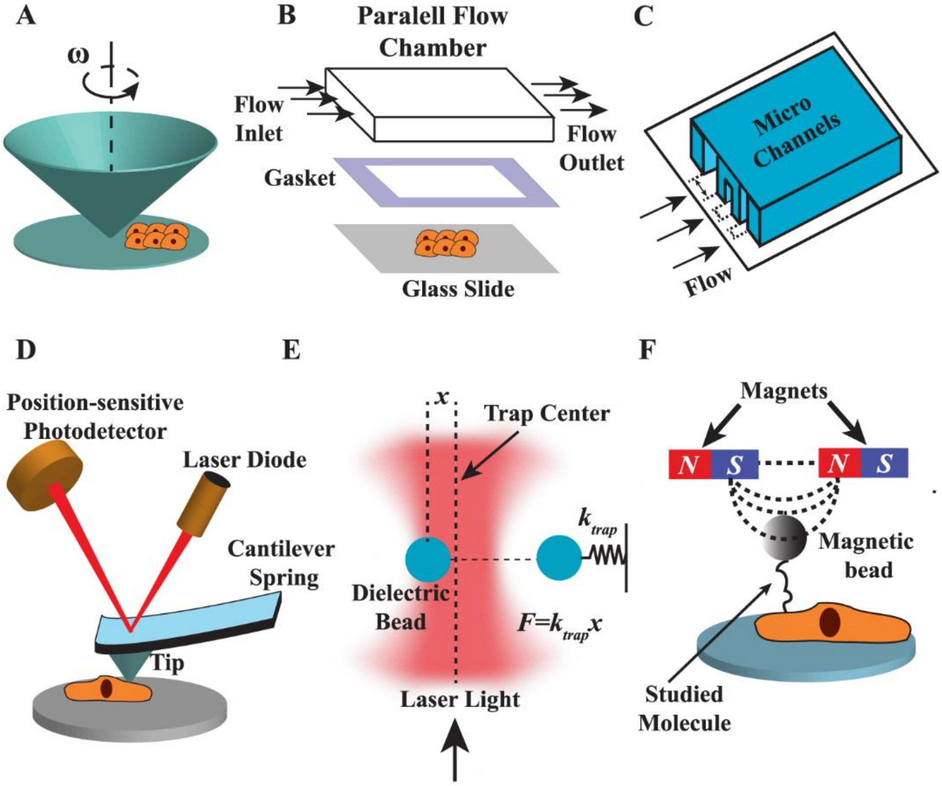

Figure 1.4 Techniques to exert and/or sense mechanical forces (Part II). (A) Cone-and-plate device. The shear flow experienced by the cells on the plate is proportional to the angular velocity of the cone. **(B)** General design of a PPFC. Cells are cultured on a glass slide that is then introduced in a parallel chamber provided with inlet and outlet flow ports. Both parallel surfaces are keeping apart by a rubber gasket. **(C)** Microchannels with different sizes fabricated using soft lithography techniques. **(D)** Typical set-up of an AFM. A tip fabricated onto a cantilever is used to scan the topography of the sample. A Laser light is reflected off the back of the cantilever onto the photodetector that accurately measures the deflection of the tip. **(E)** Working principle of an optical trap system. A Laser light with a strong electric field gradient attracts the dielectric bead to the center of the trap in a manner proportional to its displacement, just as with a simple spring system. **(F)** Basics of a magnetic tweezers setup. A strong magnetic field gradient induces forces on a probe (magnetic bead) functionalized with specific molecules that will bind to the counter-receptors on the cell surface.

There is another important set of techniques that not only allow the mechanical manipulation at the cell scale but also enable to apply and sense forces at molecular level; the most widely employed are: atomic force microscopy (AFM), optical tweezers and magnetic tweezers. The AFM uses a very sharp tip (probe) attached to a flexible cantilever to scan the surface of the sample (**Fig. 1.4D**) (63, 64). The displacements of the tip through the interaction with the sample are transmitted to the cantilever in a manner proportional to the interaction force. Any bending or twisting of the cantilever is tracked with very high precision (~2nm) (65) by a laser focused on the backside of the cantilever. AFM tips can be functionalized with proteins of the ECM or even cells. This leads to the possibility of applying forces in the order of piconewtons on nanoscale structures of the cell (66).

An alternative tool in cell mechanics is the optical tweezers or optical trap. Their physical principles, based on the ability of light to exert forces, were discovered in 1970 (67, 68). The classical optical tweezers system uses an infrared laser focused through a high numerical aperture objective to trap a transparent spherical bead (**Fig. 1.4E**) (69). When the incident photons encounter the bead, they are refracted thus changing their momentum, which results in a force on the bead. Such force is known to closely follow Hooke´s Law, i.e., force is proportional to the bead displacement. The bead displacement can be determined via imaging or with a higher precision using quadrant photodiodes. The forces exerted by optical tweezers systems can be up to 100pN (70). Similar to the tips of AFM, the beads can be functionalized with ECM proteins that can bind to receptors on the cell membrane.

A similar technique for cell mechanics studies that uses a spherical bead as a probe is the magnetic tweezers (71). However, unlike optical tweezers, the magnetic tweezers use a magnetic field gradient to apply discrete forces on the bead usually made in this case of a magnetic material (**Fig. 1.4F**). The forces are generated by an electromagnetic coil or a permanent magnet, and its magnitude is proportional to the intensity of the magnetic field. Magnetic tweezers can apply forces higher than 1nN (70). In contrast with optical techniques, magnetic tweezers induce little heat to the biological specimens. The main drawback of magnetic techniques, however, is their limited resolution in the position detection of the bead due to video based-detection.

Given the recognized importance of mechanical forces in the cell fate, the development of new mechanical manipulation tools is nowadays an active and growing field of research. Since the specific techniques are usually narrowly targeted to a specific application, very often they must be combined. Furthermore, in order to visualize and quantify the *in vivo* cell response, the different techniques are normally required to be compatible with optical microscopy techniques.

1.4 Imaging methods and nanoscopy

Optical microscopy has revolutionized the way in which living cells can be studied, since it allows the observation of the dynamics and organization of different molecular constituents of cells. Due to the low invasiveness of light, optical microscopy is better suited over other microscopy techniques when dealing with living organisms. Due to its high spatial lateral resolution ($\approx 250nm$), optical microscopy is able to resolve living micron-sized objects such as bacteria and cells. However, for the visualization of smaller objects, such as viruses or individual molecules, such as transmembrane proteins with a typical size of 1-10 nm and high expression levels (72), optical microscopy presents a major limitation. This is given by the so-called Abbe diffraction limit, which defines the maximum focusing power (d) of a microscope as $d \approx \lambda/2NA$ (73), where NA is the numerical aperture of the objective, d is the resolution of the microscope and λ is the wavelength of the excitation light. This limitation is due to the wave nature of light that makes the transmitted light emanating from a point in the specimen plane of the microscope to become diffracted at the edges of the objective aperture. The resulting diffraction pattern consists in a series of concentric rings having decaying intensities as the distance from the center increases (74). The bright region in the center of the pattern (known as Airy disk) determines the profile of the point spread function (PSF) of the microscope (75). The full width at half maximum (FWHM) of the Airy disk is ≈250 nm. Hence, two objects only can be resolved if their PSF do not overlap, or in other words, if their mutual distance is greater than 250nm (76). Since distances between proteins on the cell membrane are usually below 250nm, conventional optical microscopy cannot be used to resolve individual molecules.

Over the last decade different "super-resolution" fluorescence microscopy techniques have been invented to overcome the diffraction barrier, most of them based on the ability of precisely controlling the photophysics of individual fluorophores (77). One method to "break" the diffraction limit is by reducing the apparent density of molecules. This can be achieved by allowing the emission fluorescence of only a random subset of labeled proteins at the time. Under these conditions, the distances between labeled proteins are larger than the diffraction limit and thus the individual proteins can be spatially resolved (**Fig. 1.5A**) (73, 74). If this process is repeated several times, each time with a different group of fluorescence molecules emitting light, a superresolution image can be reconstructed. Since the localization accuracy of individual dyes is proportional to FWHM/√N (78) -with *N* being the number of emitted photons and the FWHM the size of the PSF of the microscope- the fluorescence molecules can be determined with nanometer accuracy at each frame. Techniques such as photo-activated localization microscopy (PALM) (79) and stochastic optical reconstruction microscopy (STORM) (**Fig. 1.5A**) (80) use the single molecule localization-based superresolution imaging principle.

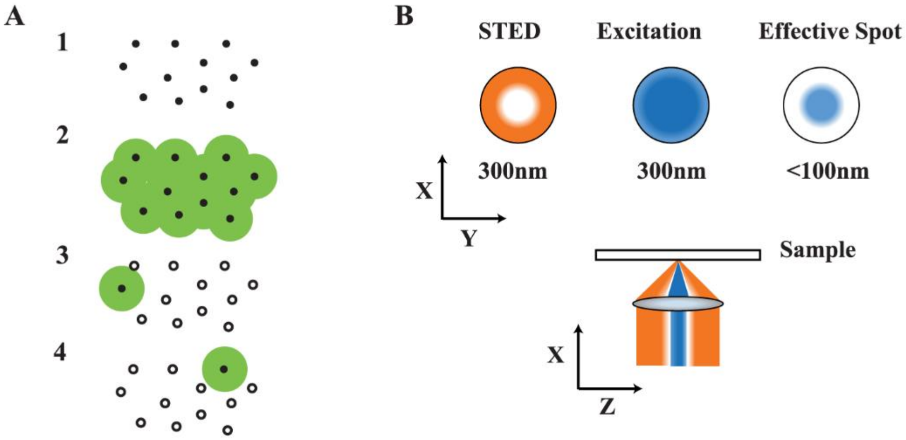

Figure 1.5 Examples of super-resolution techniques. **(A)** Working principle of PALM/STORM: In conventional fluorescence microscopy all the molecules are allowed to emit light at the same time and due to the diffraction limit of light, they cannot be individually resolved (1, 2). However, if only a subset of molecules is allowed to emit fluorescence at a given time, their positions can be determined with nm precision and a final superresolution image can be constructed after repeating the activation/localization cycle many times (3 and 4). **(B)** In STED nanoscopy, a diffraction-limited excitation laser (blue) is overlapped with a doughnut-shaped STED beam (orange). The diffraction limit is broken by de-exciting fluorophores under a doughnut shaped STED beam area, thus reducing the effective PSF. Taken from (81).

Another useful approach to attain a resolution far beyond the limit of diffraction, also based on the photophysics of a fluorophore, is the stimulated emission depletion (STED) microscopy (**Fig. 1.5B**) (82, 83). In STED, a number of dyes are excited with an excitation laser using diffraction limited optics, while a second laser is used to suppress the fluorescence emission from fluorophores located off the center of excitation, thus reducing the effective width of the PSF (77). Since STED microscopy has been extensively used during this thesis, it will be more thoroughly described in Chapter 2.

1.5 Fluorescence approaches to measure dynamics

Although super-resolution techniques offer detailed imaging with nanometer resolution, they suffer from poor temporal resolution. Thus, to gain access to the temporal information of diffusing proteins on the cell membrane, others techniques should be used. The most popular technique for several decades used is fluorescence recovery after photobleaching (FRAP) (**Fig. 1.6A**) (84, 85). In FRAP, a region of the sample is illuminated with a high intensity laser causing the fluorophores within that region to become photobleached. Diffusing fluorescently labeled molecules located in the periphery of the photobleached area will gradually diffuse into the photobleached space. Hence, the overall mobility of the fluorescently labeled molecules can be determined by measuring the recovery of the fluorescence within the photobleached area (**Fig. 1.6A**). Since FRAP is an ensemble averaging imaging technique, it cannot access any sensitive dynamic information within potentially different subpopulations of the molecule of interest. An alternative technique to FRAP is fluorescence correlation spectroscopy (FCS) (**Fig. 1.6B**) (86, 87). In FCS, a fixed region (usually a confocal volume) of the sample is continuously illuminated and the resulting florescence emission of molecules traversing the illuminated region is recorded over the time (**Fig. 1.6B**). The analysis of fluorescence intensity fluctuations over the time allows determining various parameters such as the diffusion coefficient and the number of molecules. However, the spatial resolution of FCS is diffraction limited and thus the influence of local variations in the structure of the cell membrane on the diffusion of the molecule of interest cannot be easily extracted. To overcome this limitation, two different methods have been developed that reduce the illumination area beyond the diffraction limit: STED-FCS and NSOM-FCS (88, 89). Both techniques allow assessing the influence of local variations, e.g., confinement zones <100 nm on the diffusion of molecules. Single Particle tracking (SPT) is another imaging approach that provides high temporal resolution and single molecule sensitivity (90, 91) (see details in Chapter 2). In SPT the position of individual diffusing molecules can be detected over sequential images with nanometer accuracy and time resolution in the order of milliseconds. The trajectories of single molecules can be fully reconstructed by reconnecting the centroid position of each fluorescent spot throughout the different frames (**Fig. 1.6C**) (92). To avoid possible mismatching during the reconnection process, SPT experiments must be performed at lower labeling conditions than those used for superresolution imaging. As a consequence, only a subset of molecules can be tracked at the time. Therefore, in order to obtain statistically relevant information on the dynamic of the molecule of interest, a large set of data must be collected.

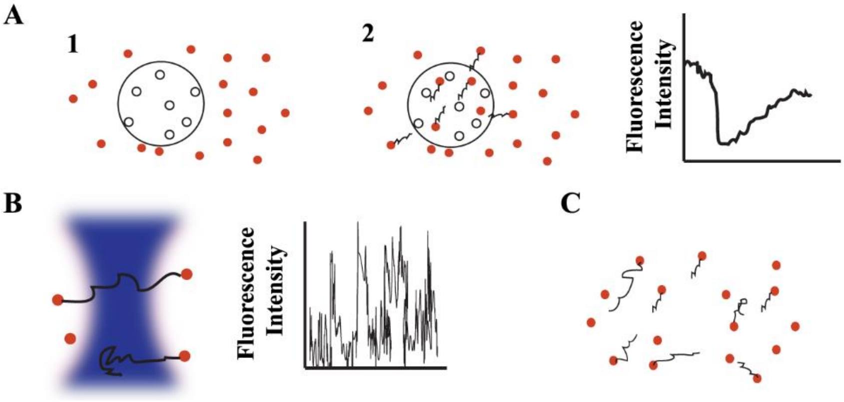

Figure 1.6 Different microscopy techniques to assess the temporal behavior of diffusing molecules. (A) Working principles of FRAP: (1) A subregion of the sample is photobleached by an intense laser illumination. (2) The molecules outside the photobleached area diffuse towards the photobleached region. The diffusion of the molecules of interest can be calculated from the analysis of the recovery of the fluorescence intensity in time (plot on the right). (**B**) In FCS, the fluorescence fluctuations from molecules crossing the excitation volume are recorded in time. By analyzing the autocorrelations in the fluorescence intensity different quantities of interest can be extracted. (**C**) In SPT, the spatial positions of individual diffusing molecules are recorded as a function of time and joined to subsequently build individual trajectories. Taken from (81).

1.6 Computational algorithms for data analysis

As previously discussed, recent advances in optics and fluorescence imaging have enabled the visualization of biological processes that occur in the cells at the nanoscale. However the manual extraction and further quantification of the features of interest in the images recorded is generally a tedious if not even an impossible option. Moreover, analysis of the dynamics of single proteins using techniques like SPT requires the reconnection of hundreds to thousands of molecular positions over hundreds of frames. Consequently, manual tracking is also an almost unthinkable option. Furthermore, although human vision is highly sensitive in detecting patterns, it lacks the accuracy and repeatability required for proper image data quantification. Thus, computational algorithms constitute a powerful tool that provides unbiased and accurate approaches for extracting information from image data. In addition, computational algorithms allow dealing with large amount of data for statistical analysis that otherwise would be highly time consuming and sometimes even impossible to handle (92).

Generally speaking, the image data analysis includes three different steps: 1) preprocessing of the raw microscopy images to reduce the noise and enhance their contrast; 2) the extraction of particular features and patterns; 3) the quantification and statistical analysis of the data extracted from the images. The preprocessing step is usually achieved by using different filtering techniques, image resampling methods, mathematical operations or even manual corrections (93-95). After pre-processing, several computational techniques can be applied for automatic detection of the desired features in the images. The main methods developed to fulfill this purpose are grouped in the category of image segmentation algorithms. Moreover, when dealing with sequential images, where the object of interest should be followed in time, tracking algorithms must be used. Finally, having the biological features of interest identified, post-processing of the images allow deriving quantitative information from them. To this aim, different strategies can be used, including the direct calculation of physical quantities from the data, data pattern recognition algorithms and colocalization algorithms (96, 97).

The principal aim of image segmentation algorithms is to separate objects of interest in a static image from their surroundings. As objects can be differentiated from the surrounding using multiple criteria, namely, color, intensity, texture or boundary continuity, several segmentation methods have been developed including: thresholding techniques (98, 99), clustering (100, 101), variational methods (102), template matching (103, 104), and Bayesian analysis (105, 106). For example, for the analysis of STED images obtained in this thesis we have used a Bayesian approach to reveal nanoclustering of the receptors of interest (see Chapter 2 for details).

On the other hand, tracking algorithms focus on reconnection of object positions through a sequence of images. Hence, tracking algorithms include a first part of image segmentation, in which the objects of interest are identified at each frame, and a second step that reconnects the positions of the objects through the different frames. The simplest approach for the reconnection problem is to link every segmented object in any given frame to the nearest neighbor in the next frame. Though “nearest” is usually referred to the spatial distance it can be also related to other quantities such as intensity, volume, orientation, and others attributes. When tracking multiple objects at the same time, the performance of the reconnection algorithms depends on the heterogeneity of any of these quantities among the different object of interest. Hence, the more similar are the objects of interest within a given frame (in terms of shape, intensity, volume, etc.) the higher will be the probability of mismatching reconnections between objects in consecutive frames. Numerous approaches have been developed to efficiently track objects surrounded by others with similar appearances, e.g., graph-based optimization algorithms (107, 108) and Bayesian estimation approaches (109-111). In this thesis we have used two different tracking algorithms. First, in Chapter 3 we describe a tracking algorithm based on the cross-correlation function to follow the motion of T-cells in the presence of shear flow. The cross-correlation function allows identifying different cells by their characteristic shapes. On the other hand, in SPT experiments as performed in Chapter 5, the automatic tracking was carried out by reconnecting the nearest fluorescence probes between consecutive frames. In addition, the abrupt variations in the intensity of the fluorescence molecules were used to detect possible mismatching events.

Once the objects of interest have been identified in a static image or reconnected through a sequence of images, different quantitative information can be extracted in order to understand the biological process under study. For example, in Chapters 4 and 5 of this thesis we extract information on the size and the intensity of individual spots observed in static STED images to latter quantify the degree of clustering of the proteins of interest. In the case of SPT experiments (as described in Chapter 5), the trajectories of the fluorescent probes can be used to calculate their mean square displacements (MSDs) and further characterize the diffusive behavior of the molecules of interest. In Chapter 3 we developed a segmentation algorithm to detect changes of velocities within trajectories obtained by tracking the centroid position of T-cells while moving under the influence of a continuous flow.

1.7 Concept of this thesis

In this thesis we have combined different state-of art optical techniques to assess the mobility and lateral organization of the two main integrins involved in the arrest and migration of leukocytes on the blood vessel: αLβ2 and α4β1. Moreover, we have used shear-flow devices to study the role of mechanical forces on the regulation of leukocyte migration on ECs. In this Chapter 1, we have provided a general description of the process of leukocyte extravasation with special emphasis on the role of the integrins α4β1 and αLβ2 studied during this research. We have also introduced the concepts of state-of-the-art biophysical techniques including mechanical manipulation tools, high spatial and temporal resolution optical microscopy, and computational algorithms for data analysis. In Chapter 2, the specific biophysical techniques used throughout this thesis are presented together with a study of the effect of stretching forces on the lateral mobility of αLβ2 on T-cells. In Chapter 3, a new algorithm for piecewise segmentation of time trace curves is described. In Chapter 4, we studied the influence of shear forces in the lateral organization of αLβ2 ligands, namely ICAM-1, on ECs and its influence on the leukocyte migration. In Chapter 5, the effect of *inside-out* and *outside-in* signaling on the lateral distribution and organization of the α4β1 integrin, is addressed. Finally, in Chapter 6, the general conclusions and future perspectives of this thesis are discussed.

1.8 References

1. Friedl P. and Wolf K., Tumour-cell invasion and migration: diversity and escape mechanisms. *Nature Rev. Immunol.*, (2003) **3**, 362-374.
2. Benedict S.H., Holding body and cell together – adhesion molecules and the medicine of the future. *Trends Cell Biol.*, (1998) **8**, 214.
3. Zecchinon L., Fett T., Bergh P.V., Desmecht D., Bind another day: The LFA-1/ICAM-1 interaction as therapeutic target. *Clin. Applied Immunol. Rev.*, (2006) **6**, 173-189.
4. Kumar S. and Weaver V. M., Mechanics, malignancy, and metastasis: The force journey of a tumor cell. *Cancer Metastasis Rev.*, (2009) **28**, 133-127.
5. Muller W.A., Getting Leukocytes to the Site of Inflammation. *Vet Pathol*, (2013) **50**, 7-22.
6. Prober J. S, Gimbrone M. A., Lapierre L. A., Mendrick D. L., Fiers W., Rothlein R., and Springer T. A. Overlapping patterns of activation of human endothelial cells by interlukin , tumor necrosis factor, and immune interferon. *J. Immunol.*, (1986) **137**, 1893-1896.
7. Ley K., Laudanna C., Cybulsky M. I., and Nourshargh S., Getting to the site of inflammation: the leukocyte adhesion cascade updated. *Nat Rev. Immunol.*, (2007) **7**, 678-689.
8. McEver, R. P., Selectins: lectins that initiate cell adhesion under flow. *Curr. Opin. Cell Biol.*, (2002) **14**, 581–586.
9. Rosen, S.D., Ligands for L-selectins: Homing, Inflammation, and beyond. *Annu. Rev. Immunol.*, (2004) **22**, 129-156.
10. Ronen Alon, Hammer D A., and Springer T. A. Lifetime of the P-selectin carbohydrate bond and its response to tensile force in hydrodynamic flow. *Nature*, (1995) **374**, 539-542.
11. Marshall B. T., Long M., Piper J. W., Yago T., McEver R. P., and Zhu C., Direct observation of catch bonds involving cell-adhesion molecules. *Nature*, (2003) **423**, 190-193.
12. Grabovsky V., Feigelson S., Chen C., Bleijs D. A., Peled A., Cinamon G., Baleux F., Arenzana-Seisdedos F., Lapidot T., van Kooyk Y., Lobb R. R., and Alon R., Subsecond Induction of a4 Integrin Clustering by Immobilized Chemokines Stimulates Leukocyte Tethering and Rolling on Endothelial Vascular Cell Adhesion Molecule 1 under Flow Conditions. *J. Exp. Med.*, (2000) **192**, 495–505.

13. Berlin, C., Bargatze R. F., Campbell J. J., von Adrian U. H., Szabo M. C., Hasslen S. R., Nelson R. D., Berg E. L., Erlandsen S. L., and Butcher E. C., α4 integrins mediate lymphocyte attachment and rolling under physiologic flow. *Cell*, (1995) **80**, 413-422.
14. Campbell J., Hedrick J., Zlotnik A., Siani M., Chemokines and the arrest of lymphocytes rolling under flow condititons. *Science*, (1998) **249**, 381-384.
15. Shamri R., Grabovsky V., Feigelson S.W., Dwir O., van Kooyk Y., and Alon, Chemokine stimulation of lymphocyte α4 integrin avidity but not of leukocyte function-associated antigen-1 avidity to endothelial ligands under shear flow requires cholesterol membrane rafts. *J. Biol. Chem*., (2002) **277**, 40027-40035.
16. Kanemitsu N., Ebisuno Y., Tanaka T., Otani K., Hayasaka H., Kaisho T., Akira S., Katagiri K., Kinashi T., Fujita N., Tsuruo T., and Miyasaka M., CXCL13 is an arrest chemokine for B cells in high endothelial venules. *Blood*, (2005) **8**, 2613-2618.
17. Bleul C. C., Fuhlbrigge R. C., Casasnovas J. M., Aiuti A., and Springer T. A., A highly efficacious lymphocyte chemoattractant, stromal cell-derived factor 1 (SDF-1). *J. Exp. Med.*, (1996) **184**, 1101-1109.
18. Alon R. and Feigelson S., From rolling to arrest on blood vessels: leukocyte tap dancing on endothelial integrin ligands and chemokines at sub-second contacts. *Semin. Immunol.*, (2002) **14**, 93-104.
19. Johnson Z., Proudfoot A. E., and Handel T. M., Interaction of chemokines and glycosaminoglycans: A new twist in the regulation of chemokine function with opportunities for therapeutic intervention. *Cytokine Growth Factor Rev*., (2005) **16**, 625–636.
20. Middleton J., Patterson A. M., Gardner L., Schmutz C., and Ashton B. A., Leukocyte extravasation: chemokine transport and presentation by the endothelium. *Blood*, (2002) **100**, 3853-3860.
21. Gunn M. D., Tangemann K., Tam C., Cyster J. G., Rosen S. D., and Williams L. T., A chemokine expressed in lymphoid high endothelial venules promotes the adhesion and chemotaxis of naive T lymphocytes. *Proc. Natl. Acad. Sci. USA*, (1998) **95**, 258–263.
22. Laudanna C. and Alon R., Right on the spot. Chemokine triggering of integrin–mediated arrest of rolling leukocytes. *Thromb. Haemost.*, (2005) **95**, 5-11.
23. Bevilacqua M. P., Endothelial-Leukocyte Adhesion Molecules. *Annu. Rev. Immunol.*, (1993) **11**, 767-804
24. Hynes, R.O., Integrins: Bidirectional, Allosteric Signaling Machines. *Cell*, (2002) **110**, 673–687.

25. Huhtala M., Hino J., Casciari D., de Luise A., and Johnson M. S., Integrin evolution: Insights from ascidian and teleost fish genomes. *Matrix Biol.*, (2005) **24**, 83-95.

26. Takagi J., Petre B. M., Walz T., and Springer T. A., Global conformational rearrangements in integrin extracellular domains in outside-in and inside-out signaling. *Cell*, (2002) **110**, 599-611.

27. Springer, T.A. and M.L. Dustin, Integrin inside-out signaling and the immunological synapse. *Curr. Opin. Cell Biol.*, (2012) **24**, 107-115.

28. Montresor A., Toffani L., Constantin G., and Laudanna C., Chemokines and the signaling modules regulating integrin affinity. *Front. Immunol.*, (2012) **3**, 127.

29. Arnaout, M.A., Integrin structure: new twists and turns in dynamic cell adhesion. *Immunol. Rev.*, (2002) **186**, 125–140.

30. Luo B-H, Carman C. V., and Springer T. A., Structural Basis of Integrin Regulation and Signaling. *Annu. Rev. Immunol.*, (2007) **25**, 619–647.

31. Cambi A., Joosten B., Koopman M., de Lange F., Beeren I., Torensma R., Fransen J. A., Garcia-Parajo M. F., van Leeuwen F. N., and Figdor C. G., Organization of the integrin LFA-1 in nanoclusters regulates its activity. *Mol. Biol. Cell,* (2006) **17**, 4270–4281.

32. van Zanten T. S., Cambi A., Koopman M., Joosten B., Figdor C. G., and Garcia-Parajo M. F., Hotspots of GPI-anchored proteins and integrin nanoclusters function as nucleation sites for cell adhesion. *Proc. Natl. Acad. Sci. USA*, (2009) **106,** 18557–18562.

33. Kim M., Carman C. V., Yang W., Salas A., and Springer T. A., The primacy of affinity over clustering in regulation of adhesiveness of the integrin αLβ2. *J. Cell Biol.*, (2004) **167**, 1241–1253.

34. Bakker G. J., Eich C., Torreno-Pina J. A., Diez-Ahedo R., Perez-Samper G., van Zanten T. S., Figdor C. G., Cambi A., and Garcia-Parajo M. F., Lateral mobility of individual integrin nanoclusters orchestrates the onset for leukocyte adhesion. *Proc. Natl. Acad. Sci. USA*, (2012) **109**, 4869–4874.

35. Borgman K. J. E., van Zanten T. S., Manzo C., Cabezón R., Cambi A., Benítez-Ribas D., Garcia-Parajo M. F., Priming by chemokines restricts lateral mobility of the adhesion receptor LFA-1 and restores adhesion to ICAM-1 nano-aggregates on human mature dendritic cells. *PLOS One*, (2014) **9**, e99589.

36. Cairo C.W., Mirchev R., and Golan D. E., Cytoskeletal regulation couples LFA-1 conformational changes to receptor lateral mobility and clustering. *Immunity*, (2006) **25**, 297-308.

37. Woolf E., Grigorova I., Sagiv A., Grabovsky V., Feigelson S. W., Shulman Z., Hartmann T., Sixt M., Cyster J. G., and Alon R., Lymph node chemokines promote sustained T lymphocyte motility without triggering stable integrin adhesiveness in the absence of shear forces. *Nat. Immunol.*, (2007) **8**, 1076-1085.

38. Chen W., Lou J., and Zhu C., Forcing switch from short -to intermediate- and Long-lived States of the aA Domain Generates LFA-1/ICAM-1 catch bonds. *J. Biol. Chem.*, (2010) **285**, 35967–35978.

39. Comrie W. A., Babich A., and Burkhardt J. K., F-actin flow drives affinity maturation and spatial organization of LFA-1 at the immunological synapse. *J. Cell Biol.*, (2015) **208**, 475–491.

40. Mitchison J. M. and Swann M. M., The mechanical properties of cell surface. *J. Exp. Biol*., (1954) **31**, 443-460.

41. Hochmuth, R. M., Micropipette aspiration of living cells. *J. Biomech.*, (2000) **33**, 15-22.

42. Kane R. S., Takayama S., Ostuni E., Ingber D. E., and Whitesides G. M., Patterning proteins and cells using soft lithography. *Biomaterials*, (1999) **20**, 2363-2376.

43. Ruiz S. A. and Chen C. S., Microcontact printing: A tool to pattern. *Soft Matter*, (2006) **3**, 168–177.

44. Weibel D. B., DiLuzio W. R., and Whitesides G. M., Microfabrication meets microbiology. *Nature Rev. Microbiol.*, (2007) **5**, 209-218.

45. Hohne D. N., Younger J. G., and Solomon M. J., Flexible microfluidic device for mechanical property characterization of soft viscoelastic solids such as bacterial biofilms. *Langmuir*, (2009) **25**, 7743-7751.

46. Balaban N. Q., Schwarz U. S., Riveline D., Goichberg P., Tzur G., Sabanay I., Mahalu D., Safran S., Bershadsky A., Addadi L., and Geiger B., Force and focal adhesion assembly: a close relationship studied using elastic micropatterned substrates., *Nat. Cell Biol.*, (2001) **3**, 466-472.

47. Li B., Xie L., Starr Z. C., Yang Z., Lin J-S, and Wang J. H-C., Development of micropost force sensor array with culture experiments for determination of cell traction forces. *Cell Motil. Cytoskeleton*, (2007) **64**, 509–518.

48. Saez A., Buguin A., Silberzan P., and Ladoux B., Is the mechanical activity of epithelial cells controlled by deformations or forces?, *Biophys. J.*, (2005) **89**, L52-L54.

49. Kamble H., Barton M. J., Jun M., Parkc S., and Nguyen N-T., Cell stretching devices as research tools: engineering and biological considerations. *Lab Chip*, (2016) **16**, 3193-3203.

50. Trepat X., Deng L., An S. S., Navajas D., Tschumperlin D. J., Gerthoffer W. T., Butler J. P., and Fredberg J. F., Universal physical responses to stretch in the living cell. *Nature*, (2007) **447**, 592-595.
51. Huang Y. and Nguyen N-T., A polymeric cell stretching device for real-time imaging with opticalmicroscopy. *Biomed. Microdevices*, (2013) **15**, 1043–1054.
52. Shao Y., Tan X., Novitski R., Muqaddam M., List P., Williamson L., Fu J., and Liu A. P., Uniaxial cell stretching device for live-cell imaging of mechanosensitive cellular functions. *Rev. Sci. Instrum.*, (2013) **84**, 114304.
53. Ursekar C. P., Teo S-K., Hirata H., Harada I., Chiam K-H., and Sawada Y., Design and construction of an equibiaxial cell stretching system that is improved for biochemical analysis. *PLOS One*, (2014) **9**, e90665.
54. Reynolds, O., An experimental investigation of the circumstances which determine whether the motion of water shall be direct or sinuous, and of the law of resistance in parallel channels. *Phil. Trans. R. Soc. Lond*., (1883) **174**, 935-982.
55. Young E. W. K. and Simmons C. A., Macro- and microscale fluid flow systems for endothelial cell biology. *Lab Chip*, (2009) **10**, 143-160.
56. Skarja G. A., Kinlough-Rathbone R. L., Perry D. W., Rubens F. D., and Brash J. L., A cone-and-plate device for the investigation of platelet biomaterial interactions. *J. Biomed. Mater. Res. A*, (1997) **34**, 427–438.
57. Buschmann M. H., Dieterich P., Adams N. A., and Schnittler H-J., Analysis of flow in a cone-and-plate apparatus with respect to spatial and temporal effects on endothelial cells. *Biotechnol. Bioeng.*, (2005) **89**, 493–502.
58. Wong A. K., Llanos P., Boroda N., Rosenberg S. R., and Rabbany S. Y., A Parallel-Plate Flow Chamber for Mechanical Characterization of Endothelial Cells Exposed to Laminar Shear Stress. *Cell Mol Bioeng*., (2016) **9**, 127-138.
59. Vanapalli S. A., Duits M. H. G., and Mugele F., Microfluidics as a functional tool for cell mechanics. *Biomicrofluidics*, (2009) **3**, 012006.
60. Sia S. K. and Whitesides G. M., Microfluidic devices fabricated in poly(dimethylsiloxane) for biological studies. *Electrophoresis*, (2003) **24**, 3563–3576.
61. Duffy D. C., McDonals Cooper, Schueller O. J. A., and Whitesides G. M., Rapid prototyping of microfluidic systems in Poly(dimethylsiloxane). *Anal. Chem.*, (1998) **70**, 4974-4984.
62. Whitesides, G. M., The origins and the future of microfluidics. *Nature*, (2006) **442**, 368-373.

63. Binning G. and Quate C. F., Atomic Force Microscopy. *Phys. Rev. Lett.*, (1986) **56**, 930-933.

64. Radmacher, M., Measuring the elastic properties of biological samples with the AFM. *IEEE Eng. Med. Biol. Mag.*, (1997) **16**, 47-57.

65. Ando T., Uchihashi T., Kodera N., Yamamoto D., Miyagi A., Taniguchi M., and Yamashita H., High-speed AFM and nano-visualization of biomolecular processes. *Eur. J. Physiol.*, (2008) **456**, 211–225.

66. Taubenberger, A., Cisneros D. A., Friedrichs J., Puech P-H., Muller D. J., and Franz C. M., Revealing Early Steps of α2β1 Integrin-mediated Adhesion to Collagen Type I by Using Single-Cell Force Spectroscopy. *Mol. Biol. Cell.*, (2007) **18**, 1634-1644.

67. Ashkin, A., Acceleration and trapping of particles by radiation pressure. *Phys. Rev. Lett.*, (1970) **24**, 156-159.

68. Ashkin A., Dziedzik J. M., Bjorkholm J. E., and Chu S., Observation of a single-beam gradient force optical trap for dielectric particles, *Opt. Lett.*, (1986) **11**, 288-290.

69. Bowman R. W. and Padgett M. J., Optical trapping and binding. *Rep. Prog. Phys.*, (2013) **76**, 026401.

70. Neuma K. C. and Nagy A., Single-molecule force spectroscopy: optical tweezers, magnetic tweezers and atomic force microscopy. *Nat. Methods*, (2008) **5**, 491-505.

71. Gosse C. and Croquette V., Magnetic Tweezers: Micromanipulation and force measurement at the molecular level. *Biophys. J.*, (2002) **82**, 3314-3329.

72. Saka S. K., Honigmann A., Eggeling C., Hell . W., Lang T., and Rizzoli S. O., Multi-protein assemblies underlie the mesoscale organization of the plasma membrane. *Nat. Commun.*, (2014) **5**, 4509.

73. Abbe E., Contributions to the theory of the microscope and microscopic perception (translated from German). *Arch Mikroskop Anat*, (1873) **9**, 413– 418.

74. Airy G. B., On the difraction of an object-glass with circular aperture. *Cambridge Phil. Soc.*, (1835) **5**, 283-291.

75. Yildiz A., Forkey J. N., McKinney S. A., Ha T., Goldman Y. E., Selvin P. R., Myosin V walks hand-over-hand: single fluorophore imaging with 1.5-nm localization. *Science*, (2003) **300**, 2061-2065.

76. Lord Rayleigh F.R.S., XXXI. Investigations in optics, with special reference to the spectroscope. *Philos. Mag.* (1879) **8**, 261-274.

77. Hell S.W., Far-Field Optical Nanoscopy. *Science*, (2007) **316**, 1153-1158.

78. Thompson, R.E., D.R. Larson, and W.W. Webb, Precise Nanometer Localization Analysis for Individual Fluorescent Probes. *Biophys. J.*, (2002) **82**, 2775-2783.

79. Betzig, E., Patterson G. H., Sougrat R., Lindwasser O. W., Olenych S., Bonifacino J. S., Davidson M. W., Lippincott-Schwartz J., and Hess H. F., Imaging Intracellular Fluorescent Proteins at Nanometer Resolution. *Science*, (2006) **313**, 1642-1645.
80. Rust M. J., Bates M., and Zhuang X., Sub-diffraction-limit imaging by stochastic optical reconstruction microscopy (STORM). *Nat Methods*, (2006) **3**, 793-796.
81. Torreno-Pina, J.A., Membrane protein nanoclustering as a functional unit of immune cells -from nanoscopy to single molecule dynamics-, *Doctoral dissertation* (2015)
82. Hell S.W., Toward fluorescence nanoscopy. *Nat. Biotech.*, (2003) **21**, 1347-1355.
83. Hell S.W. and Wichmann J., Breaking the diffraction resolution limit by stimulated emission: stimulated-emission-depletion fluorescence microscopy. *Opt. Lett.*, (1994) **19,** 780-782.
84. Axelrod, D., Koppel D. E., Schlessinger J., Elson E., Webb W. W. Mobility measurement by analysis of fluorescence photobleaching recovery kinetics. *Biophys. J.*, (1976) **16**, 1055-1069.
85. Reits E. A. J. and Neefjes J. J., From fixed to FRAP: measuring protein mobility and activity in living cells. *Nat. Cell. Biol.*, (2001) **3**, E145-E147.
86. Haustein E. and Schwille P., Fluorescence Correlation Spectroscopy: Novel Variations of an Established Technique. *Annu. Rev. Biophys*, (2007) **36,** 151-169.
87. Kim S. A., Heinze K. G., and Schwille P., Fluorescence correlation spectroscopy in living cells. *Nat. Methods*, (2007) **4**, 963-973.
88. Eggeling, C., Ringemann C., Medda R., Schwarzmann G., Sandhoff K., Polyakova S., Belov V. N., Hein B., von Middendorff C., Schonle A., and Hell, S. W., Direct observation of the nanoscale dynamics of membrane lipids in a living cell. *Nature*, (2009) **457**, 1159-1162.
89. Manzo C., van Zanten T.S., and Garcia-Parajo M.F., Nanoscale Fluorescence Correlation Spectroscopy on Intact Living Cell Membranes with NSOM Probes., *Biophys. J.*, (2011) **100**, L8-L10.
90. Kusumi A., Sako Y., and Yamamoto M., Confined lateral diffusion of membrane receptors as studied by single particle tracking (nanovid microscopy). Effects of calcium-induced differentiation in cultured epithelial cells. *Biophys. J.*, (1993) **65**, 2021-2040.
91. Saxton M.J. and Jacobson K., Single Particle Tracking: Applications to membrane dynamics. *Annu. Rev. Biophys*, (1997) **26**, 373-399.
92. Danuser G., Computer Vision in Cell Biology. *Cell*, (2011) **147**, 973-978.

93. Polesel A., Ramponi G., and Mathews V. J., Image enhancement via adaptive unsharp masking. *IEEE Trans. Image Process.*, (2000) **9**, 505-510.

94. Parker J. A., Kenyon R. V., and Troxel D. E., Comparison of Interpolating Methods for Image Resampling. *IEEE Trans. Med. Imag.*, (1983) **2**, 31-39.

95. Szeliski R., Computer vision: Algorithms and applications. *London: Springer* (2011).

96. Jain A. K., Duin R. P. W., and Jianchang M., Statistical pattern recognition: a review. *IEEE Trans. Pattern Anal. Mach. Intell,* (2000) **22**, 4-37.

97. Malkusch S., Endesfelder U., Mondry J., Gelléri M., Verveer, P. J., Heilemann M. Coordinate-based colocalization analysis of single-molecule localization microscopy data. *Histochem. Cell. Biol*., (2012). **137**, 1-10.

98. Cheriet M., Said J.N., and Suen C. Y., A recursive thresholding technique for image segmentation. *IEEE Trans. Image Process*., (1998) **7,** 918-921.

99. Osuna-Enciso, V., Cuevas E., and Sossa H., A comparison of nature inspired algorithms for multi-threshold image segmentation. *Expert Syst. Appl.*, (2013) **40**, 1213-1219.

100. Jain A. K. and Dubes R.C., Algorithms for clustering data. New Jersey (NJ): *Prentice Hall.* (1988).

101. Felzenszwalb P.F., Representation and Detection of Shapes in Images. *Doctoral dissertation* (2003).

102. Yuan Y. and He C., Variational level set methods for image segmentation based on both and Sobolev gradients. *Nonlinear Anal. Real. World Appl.*, (2012) **13**, 959-966.

103. Zou Y., Dong F., Lei B., Fang L., Sun S., Image thresholding based on template matching with arctangent Hausdorff distance measure. *Opt. Lasers Eng*., (2013). **51**, 600-609.

104. Chen C., Wang W., Ozolek J. A. and Rohde G. K., A flexible and robust approach for segmenting cell nuclei from 2D microscopy images using supervised learning and template matching. *Cytometry*, (2013) **83**, 495–507.

105. Li J., Bioucas-Dias J. M., and Plaza A., Spectral-Spatial Hyperspectral Image Segmentation Using Subspace Multinomial Logistic Regression and Markov Random Fields. *IEEE Trans. Geosci. Remote Sens*., (2012) **50**, 809-823.

106. Manzo C., van Zanten T. S., Saha S., Torreno-Pina, J. A., Mayor S., Garcia-Parajo M. F., PSF decomposition of nanoscopy images via Bayesian analysis unravels distinct molecular organization of the cell membrane. *Sci. Rep.*, (2014) **4**, 4354.

107. Sbalzarini I. F. and Koumoutsakos P., Feature point tracking and trajectory analysis for video imaging in cell biology. *J. Struct. Biol.*, (2005) **151**, 182-195.

108. Jaqaman K., Loerke D., Mettlen M., Kuwata H., Grinstein S. Schmid, S. L., Danuser G., Robust single-particle tracking in live-cell time-lapse sequences. *Nat. Methods*, (2008) **5**, 695-702.

109. Genovesio A., Liedl T., Emiliani V., Parak W. J., Coppey-Moisan M., Olivo-Marin J. C., Multiple particle tracking in 3-D+t microscopy: method and application to the tracking of endocytosed quantum dots. *IEEE Trans. Image Process.*, (2006) **15**, 1062-1070.

110. Smal I., Meijering E., Draegestein K., Galjart N., Grigoriev I., Akhmanova A., van Royen M. E., Houtsmuller A. B., and Niessen W., Multiple object tracking in molecular bioimaging by Rao-Blackwellized marginal particle filtering. *Med. Image Anal.*, (2008) **12**, 764-777.

111. Godinez, W.J., Lampe M., Wörz S., Müller B., Eils R., Rohr K., Deterministic and probabilistic approaches for tracking virus particles in time-lapse fluorescence microscopy image sequences. *Med. Image Anal.***,** (2009) **13**, 325-342.

Chapter 2

Biophysical tools for cell mechanical manipulation, imaging and data quantification used in this thesis

Super-resolution optical microscopy and single particle tracking techniques have emerged as important tools for assessing the spatiotemporal behavior of transmembrane proteins at the nanoscale. In addition, mechanical tools offer the possibility of mimicking the cell mechanical environment to which cells are normally exposed to in our body. Throughout this thesis we have combined distinct microscopy techniques and mechanical tools, as well as data analysis approaches, to gain more insight into the dynamic and spatial organization of two main adhesion receptors as well as their ligands in response to chemical and /or mechanical stimuli. In this chapter we describe the working principles of the different tools used in this thesis and present the methodological approaches that allow us to quantify nanoscopy images and single particle tracking data. Moreover, as a proof-of-concept validation of the integration of a mechanical stimulation device with a single molecule sensitive optical set-up, we have addressed the influence of isotropic stretching forces on the dynamic of αLβ2 integrins on T-cells.

2.1 Introduction

In the last decades, considerable progresses in different biophysical techniques for the visualization and manipulation of living cells have made possible a deeper and more detailed understanding of several functional processes occurring in living cells. In particular, the use of a multidisciplinary strategy, combining multiple techniques and tools, has been crucial to overcome the limitations of a single approach and thus to unravel the mechanisms that operate at molecular level in living cells. For example, the use of super-resolution techniques - like stimulated emission depletion (STED) - nowadays allows the visualization of cellular components in fixed samples with a nanometric resolution at high molecular densities. On the other hand, time-resolved techniques like single particle tracking (SPT) allow accessing the dynamic information on living cells at the single molecule level. In addition, the use of cell manipulation tools offers the possibility of mimicking in a controllable manner the mechanical environment experienced by cells under physiological conditions. While the use of these techniques has produced major advances in comprehending the cellular machinery, it has further required and stimulated the generation of new analytical tools for data analysis and interpretation. As such, in the last years we have witnessed a huge development of data science for microscopy, image analysis and biophysical experiments, which have pushed the field of cell biology towards a more quantitative understanding.

In this chapter, we describe the techniques and methods used in our experiments and data analysis. First, we introduce two advanced microscopy techniques, i.e., STED & SPT and describe their setup as well as the specific sample preparation conditions and the algorithms used to analyze the output data generated from each experimental condition. Moreover, we describe two manipulation approaches used in this thesis to mechanically stimulate the living cells: a parallel plate flow chamber (PPFC) system and a stretching device, as well as their respective calibration details. Finally, we describe the calibration and the first results obtained by combining SPT and mechanical stimulation, in order to measure the diffusion of membrane adhesion receptors on living cells while subjected to shear stress using transparent elastomer substrates. By means of this experimental configuration, we could show that the αLβ2 integrin reduces its mobility as a consequence of T-cell membrane stretching, thus suggesting that mechanical stress triggers a signaling pathway that induces conformational changes on αLβ2.

2.2 Quantitative single molecule optical tools used in this thesis

2.2.1 STED nanoscopy

STED nanoscopy was first proposed in 1994 (1) and experimentally demonstrated five years later (2). As briefly described in Chapter 1, STED uses two overlapping laser beams (**Fig. 2.1A**): a first one (excitation laser) which excites the sample and a second one (depletion or STED laser) which depletes the excitation within the region of the sample where both beams overlap. In order to reduce the effective point spread function (PSF) using this concept, the second beam is engineered to have a doughnut-shaped pattern. This can be achieved by placing a phase mask in the path of the depletion laser (**Fig. 2.1A**). Whereas the first beam induces fluorescence of the sample via spontaneous emission, the depletion laser induces the off switching of fluorophores by using the physical principle of stimulated emission. Spontaneous emission occurs when a fluorophore is excited to a higher energy state (S_1) and subsequently relaxed to the ground state (S_o) spontaneously, with the consequent emission of a photon (**Fig. 2.1B**). Due to vibrational relaxations, the photon emitted during the fluorescence process is always less energetic than the exciting photon ($\nu_2<\nu_1$), i.e., is red-shifted. On the other hand, in the stimulated emission, a second laser pumps the fluorophore while still being in the excited state, and forces the electrons to return back to the ground state without fluorescence. As a result, two identical photons are generated with exactly the same characteristics (i.e, wavelength, polarization and direction of propagation) of the incoming depletion photon (**Fig. 2.1B**). Hence, within the fluorescence detection bandwidth, stimulated emission effectively switches off the excited fluorophores.

Importantly, for the proper performance of STED, the choice of the fluorophore is a crucial step. A possible undesired scenario is that fluorophores in the excited state get further excited into higher singlet ($S_{n>1}$) or triplet ($T_{n>1}$) states instead of undergoing stimulated emission, thus leading to photobleaching (3, 4). Therefore, fluorophores bearing little absorption from the excited state to $S_{n>1}$ or $T_{n>1}$ states at the STED wavelength are better suited for STED nanoscopy (5). Another effect to take into account when choosing a dye is the potential spectral overlap between the absorption and emission spectrum of the fluorophore. A strong overlay of both spectra increases the probability of the STED beam to directly excite the fluorophore, thus leading to undesired background fluorescence and reduced image contrast (6). This effect is in practice solved by red-shifting the wavelength of the STED beam to the far-red edge of the fluorescence emission spectrum.

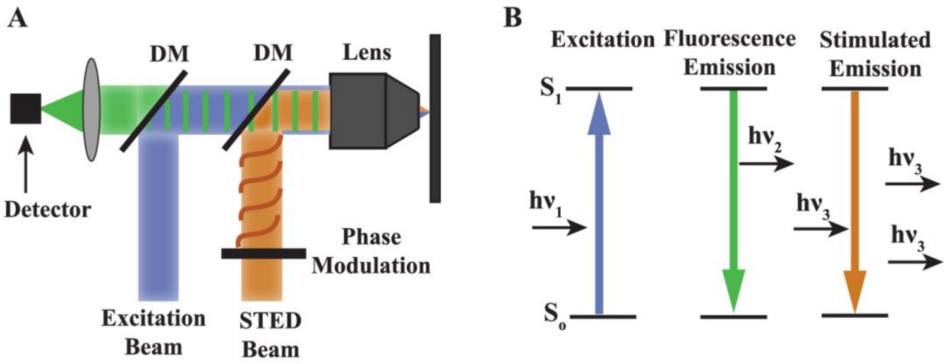

Figure 2.1 STED concept. (A) Schematics layout of a STED microscope. A phase modulation mask creates a doughnut-shaped depletion beam (orange) that overlaps with the excitation laser beam (blue). The dichroic mirrors (DM) enable the excitation beams to go onto the sample, while allowing the fluorescence emission (green) to be transmitted into the detector. **(B)** Energy diagrams for spontaneous and stimulated emission. An incident photon excites the fluorophore from the ground state S_0 to the excited state S_1 (left). Once excited, the fluorophore will decay spontaneously to the ground state by emitting a less energetic photon ($\nu_2<\nu_1$). Alternatively, the fluorophore previously excited can decay to the ground state via stimulated emission induced by an incoming red-shifted photon ($\nu_3<\nu_2<\nu_1$). As a result two identical photons are emitted with the same wavelength, phase and polarization of the incident one. Adapted from (7).

The resolution of STED nanoscopy ultimately depends on the intensity of the STED laser beam (*I*) and not on the optics used, through the formula (8):

$$\Delta r = \frac{\lambda}{2n\sin(\alpha)\sqrt{1+\frac{I}{I_s}}} \tag{2.1}$$

where n is the refractive index of the medium between the sample and the objective, α is the one-half angular aperture of the objective, λ is the wavelength of the excitation light, and I_s is the STED beam intensity value at which the fluorescence of the excited dye is depleted to 50% (8). Thus, to ensure that stimulated emission is dominant over spontaneous emission process it must be satisfied that $I > I_S$. Pulse lasers offer a good compromise between optimal depletion process and relatively low intensities of the STED beam (3). Alternatively, continuous wave (CW) STED also offers great advantages since it simplifies the implementation of setup to a large extent. Unlike pulsed lasers this continuous illumination requires higher STED beam intensities to favor stimulated emission over other competing transitions. However, this higher beam intensity used in CW-STED increases the probability of photobleaching of the fluorophore as compared to pulsed-STED. Nevertheless, by reducing the pixel integration time and increasing the scanning speed of the sample, the photobleaching on CW-STED can be reduced.

Although pulsed-STED achieves higher resolution than CW-STED, the last one is widely used due to its set-up simplicity and still good resolution (~100nm).

STED set-up description. The STED images obtained throughout this thesis have been acquired using a commercial Leica CW-STED setup (TCS-SP5). The setup is equipped with a fully motorized Leica DMI6000B microscope. A 100x 1.4 N.A. oil objective (HCX PL APO CS, Leica) was used to image the sample. For all the experiments reported in this thesis, cells were labeled using AlexaFluor 488nm (AF488) given its good performance in CW-STED set-ups (9). AF488 fluorophores were excited with the 488nm line of an ArKr laser with the intensity set at ~1µW. The intensity of the STED beam was set to its maximum value (corresponding to ~100-130 mW in the focal plane) to achieve the highest lateral resolution possible by the setup. Approximately after each hour of measurement, the alignment between the excitation and the STED beam were automatically corrected to ensure optimal performance of the setup. The fluorescence intensity coming from the sample was detected either by an avalanche photo diode module (APD) or with a photomultiplier tube (PMT). Line accumulation and image averaging were set depending on the particular labeling conditions of the sample. Nevertheless, when different experimental cells conditions were compared, all the parameters of the STED setup were kept identical. STED resolution was typically ≈120 nm, as measured by the full width at half maximum (FWHM) of a Gaussian function fitting fluorescence spots corresponding to sparse single markers.

Sample preparation for STED. The main goal of super-resolution imaging is to resolve structures at the nanometer scale. In order to exploit this feature, a high concentration of labeling probes has to be used so that all target components of the cell can be fluorescently labeled and imaged. When labeling cell receptors, the general procedure used throughout this thesis was the following: Human endothelial cells (ECs, Chapter 4) and Molt-4 T-cells (Chapter 5) were plated on coverslips functionalized either with fibronectin (20 µg/ml) or PLL (10 µg/ml) respectively. After cell adhesion, cells were fixed in 2% paraformaldehyde (PFA) for 15 min and subsequently blocked with a solution containing 3% BSA + 20 mM Glycine in PBS buffer for 15 min. Fc receptors were blocked in order to avoid non-specific binding of Antibodies (Abs) to the cells by blocking them with a 2% HS. In 2 separated steps, primary mouse anti-human Abs and goat anti-mouse AlexaFluor488 (AF488) labeled secondary Abs were added at a concentration of ≈5 µg/ml (≈30 nM) and incubated for 30 min at room temperature. Isotype controls were always performed in order to check that all the labeling were specific. After the sample preparation was completed, cells were kept in a 1% PFA solution in PBS buffer while imaging.

Analysis of STED nanoscopy images. Two different approaches have been used in this thesis to analyze STED images. Both methodologies allow estimating the stoichiometry of small molecular aggregates (nanoclusters) based on the comparison between the fluorescence intensity signals of an individual nanocluster with the intensity fluorescence signal of individual Abs spread on glass. The choice of each approach depended on the receptor density on the cell membrane. If the density of receptors on the cell membrane was low enough to allow their individual identification, Gaussian fitting of each spot was performed (a). On the contrary, if the receptor density was too high preventing the identification of individual spots, an algorithm based on the decomposition of intensity peaks with PSFs obtained from single markers was used (b).

a) Gaussian fitting of individual nanoclusters Unprocessed, super-resolution STED images were analyzed using custom written Matlab software. Individual spots were manually selected from the images and their intensity profiles were fitted to a 2D Gaussian function (10, 11):

$$I(x,y) = I_o e^{-\left(\frac{(x-xo)^2+(y-yo)^2}{2\sigma^2}\right)} \qquad (2.2)$$

where *xo* and *yo* are the peak location coordinates, *Io* is the peak intensity and σ the standard deviation in both dimensions. The lateral position and the size of the spots were determined by calculating the centroid position and the FWHM respectively. Moreover, the nanoclustering degree, i.e. number of molecules per cluster, of each individual spot was estimated based on the fact that the total intensity of individual nanoclusters is directly proportional to the number of AF488-labeled Ab, as long as a low number of molecules are contained in each nanocluster. Hence, the number of particles per cluster was determined by comparing the fluorescence intensity of each spot with the fluorescence intensity of individual AF488-labeled Abs spread on the glass coverslip. The total intensity of each nanocluster was calculated as the average of the intensity values of all those pixels located within the FWHM of the given spot. Moreover, the background intensity was subtracted from the total intensity of each individual spot. The average nanoclustering degree was finally calculated by dividing the mean fluorescence intensity of all individual nanoclusters by the mean fluorescence intensity of the spots on the glass.

b) PSF decomposition of nanoscopy images via Bayesian analysis. The characterization of high density nanoclusters was performed using an algorithm developed in our group (12) that allows the reconstruction of super-resolution images with high fidelity. The method only requires two input parameters: the width of the PSF and the intensity distribution of individual receptor markers. Both quantities can be evaluated from images of sparse immobilized fluorescent markers on glass using an approach as that described in a). The algorithm is based on the progressive full reconstruction of a synthetic image by detecting, reconstructing and correspondingly subtracting all the local peak intensity values within a sub-region of the raw unprocessed image. In a first step, the program finds the region within the image having the highest probability of containing features that can be associated to marker fluorescence emission more than to noise. Once the first image sub-region has been identified, the raw intensity map of that sub-region is attempted to be reconstructed as the sum of *n* PSFs, where each PSF is a two-dimensional Gaussian function as obtained from individual markers spread on glass. This reconstruction is performed by minimizing the Bayesian Information Criterion (BIC). Once the sub-region has been reconstructed, it is saved and excluded from the analysis in next step. Thus, the process is repeated until the full image has been reconstructed. To further minimize false peak detection, the algorithm performs a global BIC analysis on all the detected PSFs once the image has been entirely reconstructed. Together with the reconstructed image, the program returns the centroid position of all the spots, from which the nearest neighbor distribution (NND), i.e., the minimum distance between each spot and their nearest neighboring spots, can be determined. Moreover, by fitting the intensity profile of each individual spot to **Eq. 2.2**, its peak intensity *Io* can be determined. To estimate the degree of clustering, the average peak intensity calculated over all the spots on the cell membrane was divided by the mean peak intensity obtained from spots corresponding to single markers immobilized on the glass coverslip

2.2.2 Single Particle Tracking (SPT)

Although super-resolution techniques are able to overcome the diffraction limit, in many cases they are still not suitable to study dynamic processes in living cells, due to their low temporal resolution. SPT constitutes an alternative microscopy technique that offers both single molecule sensitivity and millisecond time resolution (13, 14). SPT relies on the specific attachment of a probe, usually fluorescent, to the proteins of interest, followed by the detection of its position as a function of time. By reconnecting the coordinate positions of each fluorescent spot with nanometer accuracy and as a function of time, fluorescent trajectories can be generated and the diffusion of individually labeled proteins can be characterized. However, as compared to super-resolution techniques a low amount of fluorescent markers is required (sub-labeling) in order to unambiguously reconnect the positions of individual molecules in successive frames.

When choosing a dye to perform SPT, two main features must be taken into account: brightness and photostability. The first property affects the localization accuracy of the dye which depends on the number of emitted photons N, $\sigma \sim \mathrm{FWHM}/\sqrt{N}$ (15). On the other hand, photostability allows the recording of long trajectories that otherwise would be impossible to achieve due to photobleaching. Quantum dots (QDs) (16) have been used as probes throughout this thesis for SPT experiments, due to their higher brightness and photostability with respect to organic dyes. The main drawback of QDs, however, is that they also experience blinking, i.e., a process in which emission intensity is not constant but alternates between bright and dark levels (17, 18). Hence, this process may affect the reconnection of the centroid positions through the sequential frames. Nevertheless, different algorithms have been developed to minimize the blinking effect of QDs on the reconnection process (19). The reconnection algorithm used in this thesis tolerates one missed frame without losing the tracking. Furthermore, the algorithm recognizes artifacts due to possible particle interchange, by detecting abrupt changes in the intensity and displacement of QDs over the time.

From the instrumental point of view, the most common experimental configuration used for SPT consists in the use of an inverted microscope with epi-fluorescence or total internal reflection fluorescence (TIRF) excitation. The TIRF configuration is based on the generation of an evanescent field at the glass–water interface produced by total internal reflection of the excitation laser. Because the evanescent field decays exponentially along the axial direction, the extent of illumination is limited to ~200nm away from the interface, thus avoiding excitation of unwanted fluorescent components within the cell interior (20). Alternatively, highly inclined or laminal optical (HILO) sheet illumination can be also implemented (21). In this technique the incident laser beam is highly inclined but without reaching total internal reflection. This technique enables to visualize different region of the cell interior although it has a limited depth range and works best in the central region of the object field.

Set-up description. SPT experiments were performed using a custom setup built around an inverted microscope (IX70, Olympus) working under oblique geometry or under total internal reflection (TIR) geometry (**Fig. 2.2**). Continuous excitation of QDs was provided by a 488nm laser (Sapphire 488-150CW CDRH). The diameter of the excitation beam was magnified using a telescope configuration and further focused in the back focal plane of a 1.49 NA oil immersion objective (Apon 60x TIRF, Olympus). A quarter wave plate provided circular polarized excitation light while a carousel of neutral density filters allowed varying its intensity. To switch between oblique and TIR configuration, a mirror was accurately shifted vertically with respect to the objective. A dichroic mirror (Semrock, FF500/646-Di01) was used to direct the laser light onto the sample, while allowing the transmission of the QDs fluorescence emission, which was directed onto a CMOS camera (Hamamatsu, ORCA-Flash 4.0) after further long-pass filtering (Semrock, BLP01-635R-25). The images were acquired at a frame rate of 60Hz and with a size of 256x256 pixels (Chapter 5) or 512x512 pixels (current Chapter). The pixel size in both cases was ~100nm. A custom-made incubator built around the microscope allowed the samples to be maintained at 37ºC with 5% CO_2 during the measurements.

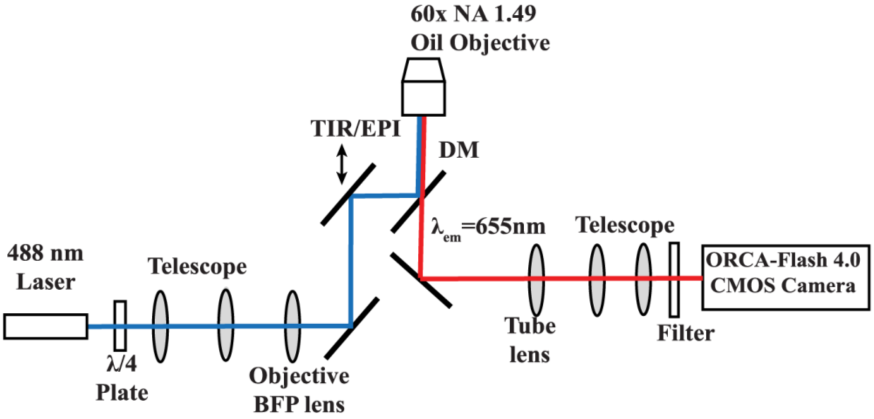

Figure 2.2 SPT setup description. A 488 nm wavelength Laser is used to excite the sample on an inverted single-molecule sensitive fluorescence microscope in TIRF or oblique illumination. A CMOS Camera was used to record the fluorescence emission after magnification and long-pass filtering. Adapted from (22).

Sample preparation for SPT. In contrast to superresolution imaging, low density labeling conditions are required for SPT. The general protocol used in this thesis for SPT experiments was the following: Streptavidine-coated QD655 were used as probe to follow the motion of cell membrane receptors. Suitable antibodies were selected according to the target protein and added to a solution of EZ-Link NHS-Biotin in a 1:1 molar ratio. Subsequently, the mixture was dialyzed over night at 4ºC in 1l of PBS using mini dialysis units of 2000 MWCO. Next day, QD655 were added to the equimolar solution of the biotinylated antibody and an excess of free biotin in order to obtain a 1:1 antibody-QD ratio. The mixture was then gently shaken for two hours at 4ºC and the concentration was finally adjusted to obtain sub-labeling conditions (~0.1 μg/ml). T-cells were then blocked by incubation for 5 min with 3% BSA, 2% HS and 20 mM glycine in PBS. Finally, antibody-QD655 conjugate was added to the cells for 3 min at room temperature, and then cells were carefully washed 5-10 times with RPMI 1640 medium.

SPT analysis. Individual QDs were tracked using a colloidal reconnection algorithm (23) adapted and translated to Matlab (24). When imaging the apical side of cells (Chapter 5), a ROI was drawn manually to select only specific areas of the cell where the trajectories remained in the same focal plane during the measurement time. To monitor the performance of the tracking algorithm, each reconstructed trajectory was visually inspected onto the overlaid raw video.
For each trajectory, the mean square displacement (MSD) was determined according to the formula (25):

$$MSD(n\Delta t) = \frac{1}{(N-1-n)}\sum_{j=1}^{N-1-n}[x(j\Delta t+n\Delta t)-x(j\Delta t)]^2+[y(j\Delta t+n\Delta t)-y(j\Delta t)]^2 \qquad (2.3)$$

where Δt is the frame period, N is the total number of frames of the trajectory, n is a positive integer that represents the time increment and x, y are the coordinates of the QD position at the starting frame $j\Delta t$ and after a time lag $t = n\Delta t$. The diffusion coefficient at short time lags (D_{1-4}) were obtained from the linear fit of the first 4 points of the MSD curve using the equation:

$$MSD(t) = 4D_{1-4}t + \Delta_o^2 \qquad (2.4)$$

where Δ_o^2 is the MSD offset at zero time lag which is proportional to the localization accuracy. Δ_o^2 is directly related to the position accuracy by:

$$\langle(\Delta x)^2\rangle = \frac{\Delta_o^2}{2d} \qquad (2.5)$$

where d corresponds to the number of dimensions in which the diffusion takes place (d=2 in our case). The choice of only 4 points for the linear fit was made to avoid interdependence between square displacement and scatter in the MSD plot (14). Finally, the full distribution of D_{1-4} was plotted as a semi-log histogram containing information from multiple trajectories on different cells. Measurements of the apparent diffusion coefficient of QDs on fixed cells were used to estimate the threshold value to discriminate immobile from mobile trajectories. The threshold was determined as the 95th percentile of the diffusion coefficient distribution, which resulted to be D=0.0025 μm^2/s (Chapter 5) or D=0.0034 μm^2/s (current chapter). The fit of the first 4 points of the MSD averaged over all the mobile trajectories was also used to calculate the mean diffusion coefficient.

To further enquire on the diffusion behavior exhibited by the mobile particles at longer times, we applied cumulative probability distribution (CPD) analysis (26). For each time lag, the CPD of square displacements was calculated and fitted with a two component model:

$$P(r^2,t) = 1 - \left[f e^{-\frac{r^2}{r_1^2}} + (1-f) e^{-\frac{r^2}{r_2^2}} \right] \tag{2.6}$$

Where P is the probability that a particle starting at the origin will be found within a circle of radius r at time t; f and $1-f$ are the fraction of the first and second components, henceforth referred to as slow and fast components respectively, and $r_i^2 (i = 1{,}2)$ are the square displacements of both components for the given time lag. Square displacement values for both components were retrieved by fitting the CPD at increasing time lags. MSD curves were generated for both components and the slow and fast diffusion coefficients were calculated by fitting the first 4 points of the corresponding MSD curve using **Eq. 2.4**. Anomalous exponents (α) of the slow and the fast component were obtained by fitting the MSD curves with an anomalous diffusion function:

$$r^2(t) = \Gamma t^{\alpha} + \delta_o^2 \tag{2.7}$$

where r^2 is the MSD, Γ is the transport coefficient and δ_o^2 is the square displacement at t=0. The value of α indicates the type of diffusive motion (14), with α=1 for Brownian diffusion and α<1 for anomalous diffusion.

2.3 Mechanical manipulation tools used in this thesis

It is broadly recognized that cells in our body are subjected to different mechanical stimuli like pushing, pulling and squeezing that play important roles in the cell function. One example is the severe deformations suffered by leukocytes during their transit across the endothelium in addition to the stress they experience during earlier stages of the extravasation process due to the shear flow. As extensively described in Chapter 1 there are several techniques available to mechanically stimulate cells. Although each of them has their strengths and weaknesses, they all are targeted to mimic in a controllable manner the mechanical stimuli experienced by cells under physiological conditions. Herein we describe in detail two techniques that account for both types of forces: stretching forces and laminar shear flow.

2.3.1 Isotropic Stretching

Stretching device description. To mimic the mechanical environment experienced by the cells, a custom stretching device based on the one described in (27) was used (**Fig. 2.3A**). The device is composed by a vacuum chamber sealed on one side by an elastic Fibronectin (FN)-coated PDMS substrate to which the cells adhere to. The elastic PDMS was stretched over a lubricated O-ring located in the central region of the vacuum chamber, by applying negative pressure underneath its outer annular region. Thereby, the resulting force transmitted to the central area of the cell culture was isotropic. The magnitude and profile of the stretching force were controlled with a resistor–capacitor pneumatic valve (VSD- EV vacuum control module) inserted between the sample and a vacuum source. The input voltage of the valve, which is proportional to its output vacuum pressure, was controlled by a custom written Labview code.

PDMS substrate preparation and calibration. Elastic membranes were prepared using PDMS (Polydimethylsiloxane) mixed with a crosslinker at 10:1 ratio. To eliminate the bubbles generated during the mixing process, the elastomer was degassed under vacuum for 1h. Subsequently, 5mg of the mixture were gently added onto a polystyrene dish of 13cm of diameter and spin-coated at different spinning velocities. In all the cases, the spin-coating process was performed as follow: first, samples were ramped up to the desired velocity at 50rpm/s of acceleration, and once the final velocity was reached, it was held for others 45s. Afterwards, the mixture was cured for 12h at 65ºC. Finally, the elastic membranes were carefully detached from the dishes using a spatula and mounted in between two mating plastic rings of 6cm diameter. The remaining membrane was cut with a scalpel. Different preparations led to different substrate thickness. Spinning velocities between 500rpm and 1000rpm resulted in a thickness ($\approx 100\ \mu m$) suitable for optical detection as verified using bright-field microscopy.

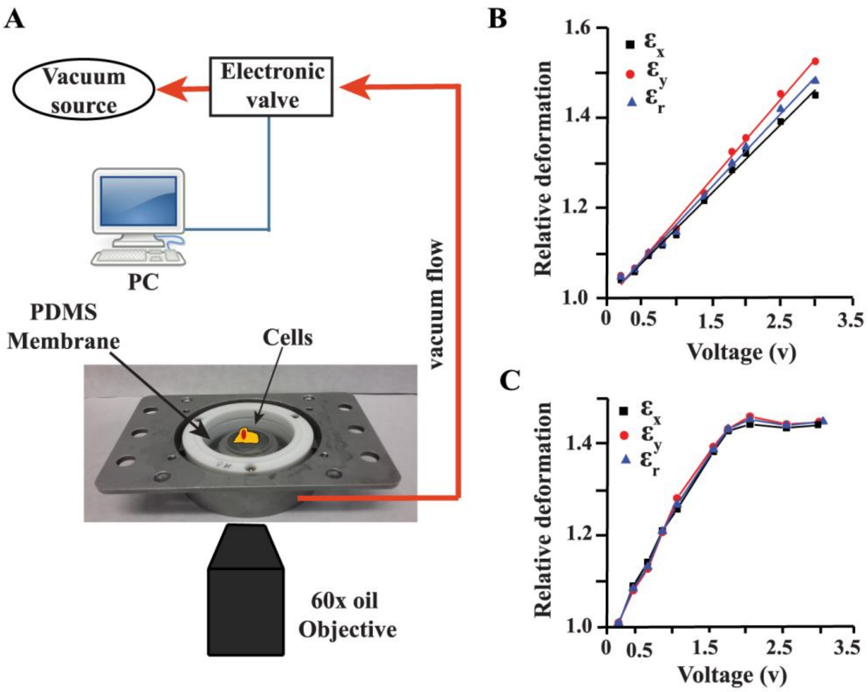

Figure 2.3 (A) Schematic of the stretching system. Electrical control of the vacuum pressure within the chamber allows application of isotropic force on the PDMS substrate, which is in turn transmitted to the cells. Red arrows indicate the direction of the vacuum flow and the deformation of the elastic PDMS. PDMS membranes spin coated either at 500rpm **(B)** or 1000rpm **(C)** were calibrated just before performing the experiments. Besides the total relative deformation (ε_r), the relative deformation along two perpendicular directions (ε_x, ε_y) was determined to check the isotropy of the deformation. The voltage applied, proportional to the vacuum pressure was electronically controlled.

Calibration of the substrate elastic response was performed by collecting bright-field images of particles immobilized on the substrate while varying vacuum pressure. To this end, 1ml of fluorescent beads (~10^8 ml^{-1}) of 100nm diameter was added to the central region of the elastic membrane for 1h at 37ºC. The solution was kept confined in the central region of the PDMS membrane by using a rubber ring of 2.1cm of inner diameter. After incubation, the elastic membranes were washed with PBS and mounted on the microscope stage. Isotropic extension of the membranes was quantified by calculating the relative change in the interparticle distance *vs.* the applied voltage. For each preset voltage, the 2D coordinates of at least N=10 particles were selected and the mean relative distance between them was calculated as:

$$\bar{\varepsilon}_r = \frac{2}{N(N-1)}\sum_{i=1}^{N-1}\sum_{j=i+1}^{N}\frac{\|r'_{ij}\|}{\|r_{ij}\|} \tag{2.8}$$

Where $\|r_{ij}\|$ and $\|r'_{ij}\|$ are the 2D Euclidean distances between the particles *i* and *j* before and upon stretching the PDMS membrane respectively. Similarly, the relative membrane deformation along the *x* and *y* axes ($\bar{\varepsilon}_x,\ \bar{\varepsilon}_y$) were calculated by substituting $\|r_{ij}\|$ and $\|r'_{ij}\|$ for the corresponding 1D Euclidean distances in Eq. 2.8. Differences between $\bar{\varepsilon}_x$ and $\bar{\varepsilon}_y$ allowed to verify the degree of uniformity of the deformations produced on the flexible substrate. Thus, only calibration regions where the differences in membrane deformation along the two axes were less than 3%, were used for the experiments. Calibration curves showed that membranes spin-coated at 500rpm exhibited linearity on the whole pressure range while membranes spin-coated at 1000rpm reached saturation (**Fig. 2.3B, C**). Nevertheless, the elastic modulus (proportional to curves slope in the linear regime) was similar in the both cases. Since at large strain values the cells were disrupted, the maximum stretching deformation applied was 30% ($\bar{\varepsilon}_r = 1.3$), still below the plateau region ($\bar{\varepsilon}_r = 1.45$, **Fig. 2.3C**). Therefore, both membranes fabricated either at 500rpm or 1000rpm were suitable for experiments.

2.3.2 Shear Flow device

Micro-chamber description and calibration. Shear flow experiments were performed with a parallel-plate closed flow chamber (PPFC) (FCS2, Bioptechs Inc., **Fig. 2.4**). Endothelial cells - growth onto 40 mm coverslips - were placed on the micro-aqueduct slide separated by 100 µm-thick gasket with a rectangular surface (1.4 x 2.2 cm). The fully assembled flow chamber was mounted on the stage of the inverted microscope described above (section 2.2.2). The flow chamber was connected on one end to an automated syringe pump (FCS2 Micro-Perfusion Pump) and on the other end to a medium waste reservoir. 5% CO_2-enriched RPMI-1640 cell culture medium at 37ºC was perfused at constant shear flow through the chamber. Shear stress of flowing medium, *τ*, was calculated using the equation (28):

$$\tau = \frac{6Q\mu}{wh^2} \tag{2.9}$$

where *Q* is the flow rate, µ is the viscosity of the fluid, *w* is the width and *h* is the height of the gasket. The flow rate and in turn the shear stress can be set by tuning the speed of the pump. In order to calibrate the system, RPMI medium was perfused through the chamber at an arbitrary pump speed for 10 min and the collected volume was measured. The flow rate was determined by dividing the volume measured by the time (10min). The calculated flow rate was then used to adjust pump speed and to obtain the desired shear stress (either 1 dyn/cm^2 or 8 dyn/cm^2) using **Eq. 2.9**. Since the flow rate depends on the tubing diameters and these tend to stretch with the use, the calibration was always performed just before carrying on the experiments.

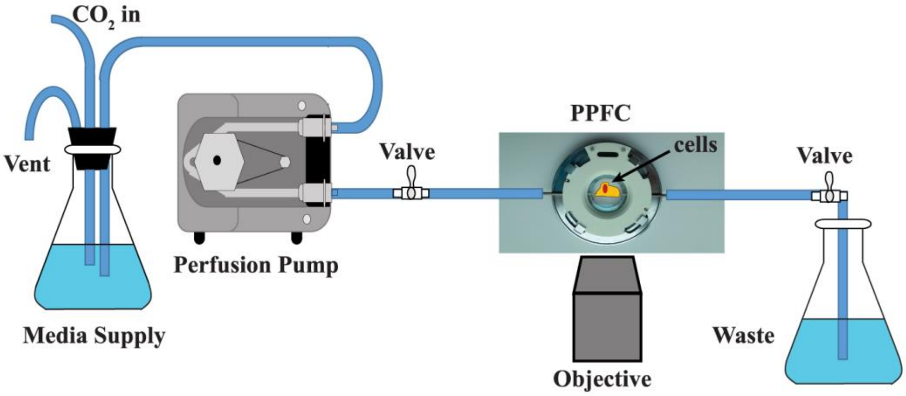

Figure 2.4 Perfusion diagram for the PPFC device. A container with the cell medium and CO$_2$ is flushed into the PPFC by means of a perfusion pump that is electronically controlled through a computer. Mechanical valves placed at specific positions along the flow line allow interrupting the flow manually, thus avoiding possible bubbles to go inside the chamber when it is assembled and disassembled from the microscope stage. A second container is placed at the end of the flow line to collect the wastes.

2.4 SPT of individual receptors under the presence of mechanical stimulation

The stretching device has been designed in order to be easily mounted onto the stage of the inverted microscope used for SPT (section 2.2.2). To minimize mechanical and thermal drift, the device was firmly fixed to the microscope stage by means of 4 small screws. Moreover, due to the elastic tension exerted by the PDMS over the objective, once the sample was focused, the objective was locked to assure a constant focus during the measurements. The choice of the fluorescence probe was especially crucial in these types of experiments since PDMS optical properties were different from those of the glass. Though the refraction index of fabricated PDMS was close to the one from glass, the first one induces light scattering due to impurity and background fluorescence, thus decreasing the signal to noise ratio. Therefore, organic dyes were found not suitable for these experiments due to their low brightness that together with the PDMS-induced scattering resulted in a poor signal to noise ratio. In contrast, the emission of QD655 was high enough to ensure a suitable signal to noise ratio for localization and particle tracking in spite of the scattering and were therefore used as probes.

The full experimental configuration was used to measure the diffusion of αLβ2 (LFA-1) integrins expressed on Jurkat T-cells under the influence of mechanical stimulation. Integrins are transmembrane receptors involved in adhesion and migration processes. In particular, the αLβ2 integrin constitutes one of the primary adhesion receptors in T-cells. As discussed in Chapter 1, adhesion depends on two main properties of integrins: affinity (29, 30) and avidity (31). The first one is determined by the molecular conformation of the receptor whereas the second one refers to their capacity to form nanoclusters. Moreover it has been demonstrated that different conformational states exhibited different lateral diffusion of αLβ2 (24, 32). In addition, recent works have suggested that mechanical stress might influence receptor behavior at the molecular level and thus induce changes in affinity of integrins (33, 34). In the physiological context, αLβ2 mediates the migration of T-cells through the endothelium, which occurs under shear stresses induced by the blood flow. Hence, understanding the effect of forces on αLβ2 activation is a critical step to unravel how this integrin regulates adhesion and migration of leukocytes. Therefore, the aim of these experiments have been two-fold: a) provide a proof of concept of the combined use of SPT and mechanical stimulation; b) investigate the influence of mechanical forces on the lateral mobility of αLβ2.

2.4.1 SPT of αLβ2 on stretching substrates

Freshly prepared PDMS substrates (spin coated at 500rpm) were calibrated the same day they were used for experiments with cells. After calibration, PDMS membranes were thoroughly washed with ethanol, blow dried with nitrogen gas and subjected to UV/ozone treatment for 20min. The central area of the substrate was then coated with 500µl of FN (20µm/ml) by incubation for 30min. Jurkat cells were diluted to $8x10^5$ per ml in RPMI-1640 medium and spread onto the FN coated area for 30 min. αLβ2 was labeled using the TS2/4 Ab conjugated to QD655 as described in section 2.2.2. Note that TS2/4 is a conformation-independent Ab and therefore reports on the entire αLβ2 population regardless of its activation state. Finally, samples were placed under the SPT microscope and imaged by collecting several movies containing individual trajectories for 10min. Afterwards, a 15% stretching force was applied to the elastic membrane and kept for another 20min during which additional movies were recorded.

2.4.2 Results

Performance of the experimental configuration. In order to characterize the combined SPT-stretching device configuration, Jurkats cells were spread on FN coated PDMS and subjected to a 15% stretching force. Images of the cells were taken before and after applying the stress (**Fig. 2.5 A, B**).

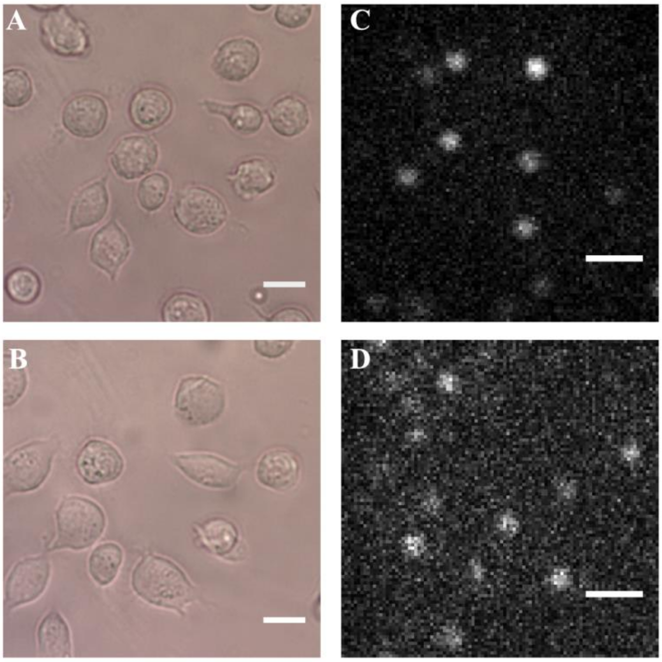

Figure 2.5 Bright-Field images of Jurkat cells onto a FN coated PDMS substrate after 30 min of incubation, before **(A)** and after **(B)** applying a 15% of stretching deformation. Representative images of fluorescent QDs either on glass **(C)** or on PDMS substrate **(D)**, using TIRF illumination. Scale bars represent either 20 µm (A, B) or 1 µm (C, D). Images were acquired at a frame rate of 60 Hz.

As expected, in accordance with previous studies, a percentage of cells (~60%) showed a remarkable increase (larger than the applied stretch) in cell contact area a few minutes after stretching (35). To characterize the experimental setup on SPT experiments, the performance of QD655 as a probe was tested. For this purpose, QD655 were passively absorbed onto PDMS membranes and imaged in TIRF configuration. Due to scattering of the light through the PDMS, the signal to background ratio of the fluorescent images was lower as compared to that on glass under the same experimental settings (7 on PDMS vs 9 on glass) (**Fig. 2.5 C, D**). However, the contrast of the images remained high enough to make QD655 distinguishable from the background and allow their tracking. To quantify how much the PDMS could affect the performance of SPT experiments, the localization accuracy of QDs was calculated using **Eq. 2.5**. QDs were localized about two-fold better on glass (~20nm) than on PDMS (~40nm). Stretching of the PDMS did not further affected localization accuracy of QD655. Hence, using QD655 as a probe allowed performing SPT experiments on mechanically stimulated cells.

αLβ2 mobility under mechanical stimulation. Analysis of single particle trajectories was used to investigate the dynamics of αLβ2 under the influence of stretching forces. Samples were prepared as described above (section 2.4.1). To capture the motion of individual QDs we used a SPT set-up under TIRF illumination. Movies of 15 min of duration were recorded before and after applying a 15% of stretching. In both cases trajectories of QDs were analyzed and the diffusion coefficient at short time lags (D_{1-4}) were calculated as described above (section 2.2.2). Likewise, to discriminate immobile subpopulation from the mobile one, we used QDs immobilized on PDMS as reference (see details in section 2.2.2). In presence of 15% stretching, we observed an increase in the immobile fraction, from 31% in resting conditions to 63% after stretching (**Fig. 2.6A**).

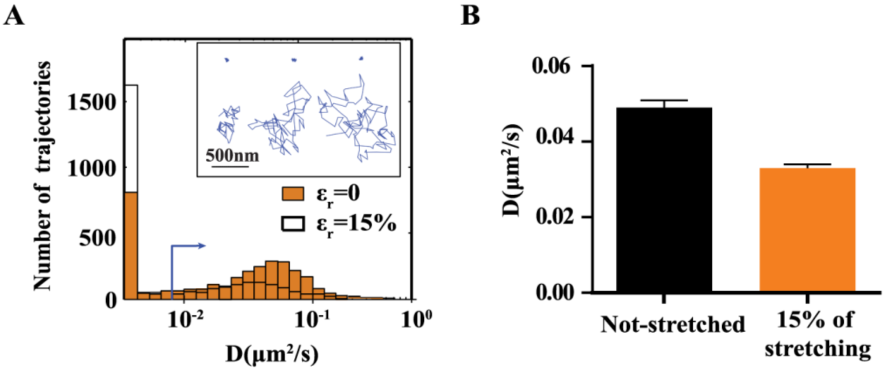

Figure 2.6 (A) Distribution of diffusion coefficients obtained for single αLβ2 trajectories (N>500) collected from 3 independent experiments containing at least 10 cells each. Diffusion coefficients in not stretching conditions are represented by filled yellow bars whereas empty bars represent diffusion in presence of 15% of stretching. Only trajectories lasting longer than 13 frames were selected for the analysis. The blue arrow indicates the threshold value used to classify mobile vs. immobile trajectories. (Inset) Representative αLβ2trajectories obtained in the presence of force. **(B)** Diffusion coefficient obtained by the fit of the ensemble-averaged MSD for the mobile trajectories in absence (black) and in presence of 15% of stretching force (yellow).

Since the instantaneous diffusion coefficient D does not allow to investigate dynamical behavior at long times, we applied CPD analysis (section 2.2.2) to enquire on the type of diffusion exhibited by the mobile fraction of αLβ2 at larger time-scale. As shown in **Fig. 2.7A**, application of force changed the dynamics of the faster component, with a reduction of both the diffusion coefficient (from $D=(0.060\pm0.001)\mu m^2/s$ to $D=(0.036\pm0.001)\mu m^2/s$) and the value of the anomalous exponent (from $\alpha=0.85\pm0.01$ to $\alpha=0.74\pm0.01$). On the other hand, the slow diffusing component D and α did not show significant force-induced changes. However, force altered the balance between immobile, slow and fast mobile populations (**Fig. 2.7B**).

These preliminary data show that αLβ2 mobility is strongly influenced by the presence of forces acting on the cellular membrane, suggesting that mechanical stress play an important role on αLβ2 dynamics. One plausible scenario to explain our results is that forces exerted on integrins by binding to its ligand FN, will activate β1 integrins, which will locally re-model the actin cytoskeleton propagating this effect to αLβ2 and causing its activation via inside-out signaling. Nevertheless, many more experiments would need to be performed to test this hypothesis, as well as appropriate controls to exclude potential artifacts associated to hindering mobility effects of the PDMS substrate on the basal cell membrane.

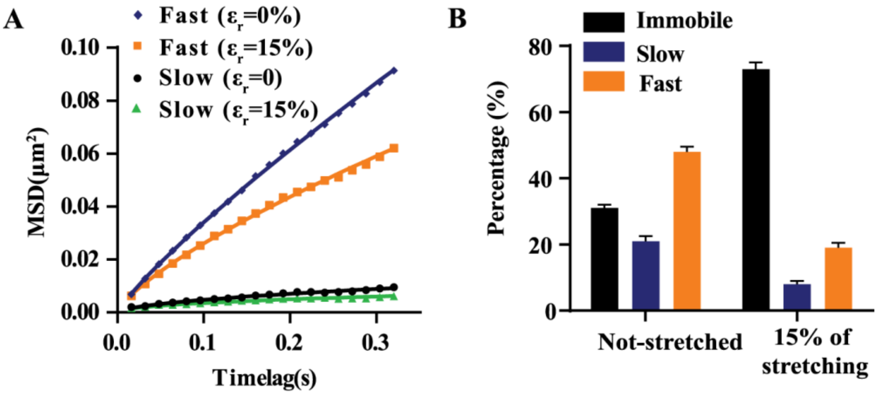

Figure 2.7 (A) MSD curves of the slow and fast components derived from the cumulative probability distribution analysis. The diffusion coefficient of both components decreases upon force stimulation. **(B)** Comparison between the different mobility subpopulations in absence and in presence of force.

2.5 Discussion

In this chapter, we have discussed the advantages and limitations of STED nanoscopy. This technique has been able to overcome the diffraction limit of light by exploiting the physical properties of the fluorophores used as probes. In spite of its high lateral spatial resolution, this techniques lack the temporal resolution for detecting dynamic events that take place at molecular level on the cell membrane. SPT overcomes this limitation as it is able to reach millisecond time resolution at the expense of low labeling density, thus providing information only on a limited number of molecules simultaneously. Since each technique by its own cannot assess the spatiotemporal organization of the different cell components at the nanoscale, in this thesis we have combined the two different approaches.

We have also discussed the working principles of two different devices used to mechanically stimulate the cells: a PPFC device that was used to mimic the shear stress experienced by ECs and T-cells within the blood vessels (Chapter 3); and a custom stretching device that allows applying isotropic forces on cells. Both devices were used - in combination with different microscopy optical techniques - to visualize the effect produced by mechanical forces at the molecular level on living cells. Moreover, we have designed the stretching device to be fully compatible with our SPT setup. We also have found the optimal fabrication conditions for PDMS substrates that make them suitable for single molecule fluorescence microscopy. Furthermore we showed that QDs are more suitable than organic dyes in order to obtain higher signal to background ratios, when using PDMS substrates. The use of the stretching device on the SPT setup was further validated by performing SPT of αLβ2 integrin on T-cells.

Our data showed that αLβ2 mobility is influenced by the presence of forces acting on the cellular membrane, suggesting that mechanical stress play an important role on αLβ2 dynamics. Since in our experiments cells are seeded on a fibronectin-coated substrate (binding specifically to β1 integrin but not to β2) the effect of force on αLβ2 must be of an indirect nature. Based on previous studies (36), cytoskeleton-mediated cross-talk between β1 integrins and β2 might induce αLβ2 activation and immobilization. In absence of forces, αLβ2 is in its low affinity conformation, weakly and dynamically interacting with the cytoskeleton. Once the force is applied, fibronectin-β1 bonds act as mechano-sensors, transmitting the mechanical stimulus to β2 integrin via the actin network, inducing a conformational change and firmly anchoring it to the cytoskeleton. Thus, we hypothesized that mechanical stress triggers a signaling pathway that induce conformational changes on αLβ2. However, another possible explanation for the reduction in mobility of αLβ2 is that due to decreased space between the basal cell membrane and the PDMS substrate upon stretching, QDs could get trapped. Thus, the apparent reduction in the αLβ2 mobility might be an artifact due to the immobilization of QD in the cell-substrate interspace. Unfortunately, the experiments performed so far are not enough to discard this possibility. Thus, future work would need to be done in order to verify our biological hypothesis.

2.6 References

1. Hell S. W. and Wichmann J., Breaking the diffraction resolution limit by stimulated emission: stimulated-emission-depletion fluorescence microscopy. *Opt. Lett.*, (1994) **19**, 780-782.

2. Klar T.A. and Hell S. W., Subdiffraction resolution in far-field fluorescence microscopy. *Opt. Lett.*, (1999) **24**, 954-956.
3. Donnert G., Keller J., Medda R., Andrei M. A., Rizzoli S. O., Lührmann R., Jahn R., Eggeling C., and Hell S. W., Macromolecular-scale resolution in biological fluorescence microscopy. *Proc. Natl. Acad. Sci. USA*, (2006) **103**, 11440-11445.
4. Song L., Varma C. A., Verhoeven J. W., Tanke H. J., Influence of the triplet excited state on the photobleaching kinetics of fluorescein in microscopy. *Biophys. J.*, (1996) **70**, 2959-2968.
5. Hotta, J-I., Fron E., Dedecker P., Janssen K. P. F., Li C., Müllen K., Harke B., Bückers J., Hell S. W., and Hofkens J., Spectroscopic rationale for efficient stimulated-emission depletion microscopy fluorophores. *J. Am. Chem. Soc*., (2010) **132**, 5021-5023.
6. Vicidomini G., Moneron G., Eggeling C., Rittweger E., and Hell S. W., STED with wavelengths closer to the emission maximum. *Opt. Express*, (2012) **20**, 5225-5236.
7. Farahani J. N., Schibler M. J., and Bentolila L. A., Stimulated Emission Depletion (STED) Microscopy: from Theory to Practice. *Microscopy: Science, Technology, Applications and Education,* (2010), 1539-1547. Retrieved from http://www.formatex.org
8. Hell S. W., Far-field optical nanoscopy. *Science*, (2007) **316**, 1153-1158.
9. Moneron G., Medda R., Hein B., Giske A., Westphal V., and Hell S. W., Fast STED microscopy with continuous wave fiber lasers. *Opt. Express*, (2010) **18**, 1302-1309.
10. van Zanten T. S., Cambi A., Koopman M., Joosten B., Figdor C. G., Garcia-Parajo M. F., Hotspots of GPI-anchored proteins and integrin nanoclusters function as nucleation sites for cell adhesion. *Proc. Natl. Acad. Sci. USA*, (2009) **106**, 18557-18562.
11. van Zanten T.S., Gomez J., Manzo C., Cambi A., Buceta J., Reigada R., and Garcia-Parajo M.F., Direct mapping of nanoscale compositional connectivity on intact cell membranes. *Proc. Natl. Acad. Sci. USA*, (2010) **107**, 15437-15442.
12. Manzo C., van Zanten T. S., Saha S., Torreno-Pina J. A., Mayor S., and Garcia-Parajo M. F., PSF decomposition of nanoscopy images via Bayesian analysis unravels distinct molecular organization of the cell membrane. *Sci Rep.*, (2014) **4**, 4354.
13. Kusumi A., Sako Y., and Yamamoto M., Confined lateral diffusion of membrane receptors as studied by single particle tracking (nanovid microscopy). Effects of calcium-induced differentiation in cultured epithelial cells. *Biophys. J.*, (1993) **65**, 2021-2040.
14. Saxton M. J., Single-Particle Tracking: The Distribution of Diffusion Coefficients. *Biophys. J.*, (1997) **72**, 1744-1753.

15. Schmidt T., Schütz G. J., Baumgartner W., Gruber H. J., and Schindler H., Imaging of single molecule diffusion. *Proc. Natl. Acad. Sci. USA*, (1996) **93**, 2926-2929.

16. Walling M. A., Novak J.A., and Shepard J.R.E., Quantum Dots for live cell and in vivo imaging. *Int. J. Mol. Sci.*, (2009) **10**, 441-491.

17. Nirmal M., Dabbousi B. O., Bawendi M. G., Macklin J. J., Trautman J. K., Harris T. D., and Brus L. E. Fluorescence intermittency in single cadmium selenide nanocrystals. *Nature*, (1996) **383**, 802-804.

18. M. Kuno, Fromm D. P., Hamann H. F., Gallagher A., and Nesbitt D. J., Nonexponential “blinking” kinetics of single CdSe quantum dots: A universal power law behavior. *J. Chem. Phys.*, (2000) **112**, 3117.

19. Sergé A., Bertaux N., Rigneault H., and Marguet D., Dynamic multiple-target tracing to probe spatiotemporal cartography of cell membranes. *Nat. Meth.*, (2008) **5**, 687-694.

20. Axelrod D., Total internal reflection fluorescence microscopy in cell biology. *Traffic*, (2001) **2**, 764–74.

21. Tokunaga M., Imamoto N., and Sakata-Sogawa K., Highly inclined thin illumination enables clear single-molecule imaging in cells. *Nat. Meth.*, (2008) **5**, 159-161.

22. Torreno-Pina J. A., Membrane protein nanoclustering as a functional unit of immune cells -from nanoscopy to single molecule dynamics-, *Doctoral dissertation* (2015)

23. Crocker J.C. and Grier D. G., Methods of digital video microscopy for colloidal studies. *J. Colloid Interface Sci.*, (1996) **179**, 298-310.

24. Bakker G. J., Eich C., Torreno-Pina J. A., Diez-Ahedo R. , Perez-Samper G., van Zanten T. S., Figdor C. G., Cambi A., and Garcia-Parajo M. F., Lateral mobility of individual integrin nanoclusters orchestrates the onset for leukocyte adhesion. *Proc. Natl. Acad. Sci. USA*, (2012) **109**, 4869–4874.

25. Kusumi A., Sako Y., and Yamamoto M., Confined lateral diffusion of membrane receptors as studied by single particle tracking (Nanovid Microscopy). Effects of Calcium-induced differentiation in dultured epithelial cells. *Biophys. J.*, (1993) **65**, 2021-2040.

26. Schütz G. J., Schindler H., and Schmidt T. , Single-molecule microscopy on model membranes reveals anomalous diffusion. *Biophys. J.*, (1997) **73**, 1073-1080.

27. Trepat X., Deng L., An S. S., Navajas D., Tschumperlin D. J., Gerthoffer W. T., Butler J. P., and Fredberg J. J., Universal physical responses to stretch in the living cell. *Nature* (2007) **447**, 592-596.

28. Lane W. O., Jantzen A. E., Carlon T. A., Jamiolkowski R. M., Grenet J. E., Ley M. M., Haseltine J. M., Galinat L. J., Lin F. H., Allen J. D., Truskey G. A., and Achneck

H. E., Parallel-plate flow chamber and continuous flow circuit to evaluate endothelial progenitor cells under laminar flow shear stress. *J. Vis. Exp.*, (2012) **59**, e3349.

29. Xie C., Shimaoka M., Xiao T., Schwa P., Klickstein L.B., and Springer T.A., The integrin -subunit leg extends at a Ca2+-dependent epitope in the thighgenu interface upon activation. *Proc. Natl. Acad. Sci. USA*, (2004) **101**, 15422–15427.
30. Luo B. H., Carman C. V., and Springer T. A., Structural basis of integrin regulation and signaling. *Annu. Rev. Immunol.*, (2007) **25**, 619-647.
31. Cambi A., Joosten B., Koopman M., Beeren I., Torensma R., Fransen, Frank J. A., van Leeuwen N., and Figdor C. G., Organization of the integrin LFA-1 in nanoclusters regulates its activity. *Mol. Biol. Cell*, (2006) **17**, 4270–4281.
32. Constantin G., Majeed M., Giagulli C., Piccio L., Kim J. Y., Butcher E. C., and Laudanna C. , Chemokines trigger immediate β2 integrin affinity and mobility changes: Differential regulation and roles in lymphocyte arrest under flow. *Immunity*, (2000) **13**, 759–769.
33. Roca-Cusachs P., Iskratsch T., and Sheetz M. P. Finding the weakest link – exploring integrin-mediated mechanical molecular pathways. *J. Cell Sci.*, (2012) **125**, 3025–3038.
34. Schürpf T. and Springer T. A., Regulation of integrin affinity on cell surfaces. *EMBO J.*, (2011) **30**, 4712–4727.
35. Cairo C. W., Mirchev R., and Golan D. E., Cytoskeletal regulation couples LFA-1 conformational changes to receptor lateral mobility and clustering., *Immunity* (2006) **25**, 297–308.
36. Chan, J. R., Hyduk S. J., and Cybulsky M. I., α4β1 integrin/VCAM-1 interaction activates αLβ2 integrin-mediated adhesion to ICAM-1 in human T cells. *J. Immunol*, (2000) **164**, 746-753.

Chapter 3

PLANT: A method for detecting changes of slope in noisy Trajectories

Time traces obtained from biophysics experiments - such as the migration of leukocyte across endothelial cells - contain information of the underlying processes that occur at molecular level. Accurate quantification of these data can help to understand the details of the complex dynamic of biological systems. In this Chapter we describe PLANT (Piecewise Linear Approximation of Noisy Trajectories), a segmentation algorithm that allows the reconstruction of time trace data as consecutive straight lines, from which changes of slopes and their respective durations can be extracted. We first present the theoretical description and the general methodology of the algorithm, including a method to automatically estimate the noise from the data. Then, we perform extensive simulations to characterize the strengths and the limitations of the method. Moreover, we provide both theoretical and empirical rationale for the performance of the algorithm in the different conditions tested. Last, we apply the algorithm to experimental data obtained from tracking the centroid position of lymphocytes migrating under the effect of a laminar flow.

This work is currently under preparation to be submitted in *Biophys. J.:* A. Sosa-Costa, I. Piechocka, L. Gardini, F. Pavone, M. Capitanio, M. F. Garcia-Parajo, C. Manzo. "PLANT, a method for detecting changes of slope in noisy Trajectories"

3.1 Introduction

The output of several biophysics experiments, such as DNA elongation via magnetic and optical tweezers (1–3), myosin motor motility (4), and cell tracking under shear flow (5, 6) consists in time trace curves. Many of these curves show alternate regions of pauses and linear increments usually associated with different events taking place at molecular level (5, 6). The recognition of such regions and their associated physical parameters such as, segment duration and rate of elongation are essential to better understand the underlying dynamics of the ongoing processes. However, noise due to thermal fluctuations affects these data and limits their accurate quantification. Thus, the automatic detection of the different features of the time trace curves remains a challenging computational problem.

Several approaches have been developed for the automatic segmentation of time traces (7–10). One of the most common approaches is the approximation of the original data in different straight lines, usually referred as to Piecewise Linear Approximation (PLANT). Given a time series, this approach consists in constructing a piecewise linear function that produces the best representation either using a limited number of segments, or not exceeding a user-specified threshold for the error (11). Generally speaking, the segmentation algorithms based on the PLANT can be grouped in three different categories: sliding window, top-down, and bottom-up algorithms (11). In the sliding windows algorithms, a segment is grown until the error after adding a new point to the segment exceeds some specified threshold. Although this type of approach is ideal to analyze the data while being generated (i.e. online segmentation), it tends to overestimate the number of segments (12). On the other hand, the top-down type of algorithms work by recursively splitting the entire signal until certain error threshold is reached. Last, bottom-up algorithms start by arbitrarily dividing the signal in multiple segments and recursively merging the two more similar adjacent segments. Likewise, the process is stopped when some criterion fixed by the user is met. Although in general top-down and bottom-up algorithms have shown to perform better than the sliding window algorithm (11), there are several variations of these three methods, each of them usually adapted to perform better on specific type of data (13–16).

Here, we describe a bottom-up type of algorithm that can robustly reconstruct noisy time-traces. Unlike conventional bottom-up algorithms, in a first step we find the points where there is a potential variation of the slopes (change points) and then we recursively merge the adjacent segments. We follow a likelihood-based approach and therefore we do not impose any condition on the number of segments or on the residual error. We tested our algorithm on a variety of conditions, including different noises, slopes, and segment lengths and provide reasonable explanations on the observed results. In addition, we validated our algorithm on time traces experimentally obtained from tracking the centroid of lymphocytes while moving on endothelial cells (EC) under the presence of a constant shear flow.

3.2 Algorithm description

We consider an input data consisting in a trajectory in which an observable y is sampled at N discrete time points t_i. The working hypothesis is that the trajectory (t_i; $y(t_i)$) is composed by a sequence of K adjacent linear segments, bounded by $K + 1$ change points cp_k occurring for values of the index $i = cp_k$ and corrupted with Gaussian noise having constant variance σ^2 (**Fig. 3.1A**). Given a minimum segment length N_{MIN}, an estimation of the noise σ^2, and a confidence level α, the objective of the algorithm is to efficiently and precisely determine the change points (**Fig. 3.1B**), and thus be able to measure the segments duration and slope (**Fig. 3.1C**).

The flow diagram of the algorithm is depicted in **Fig. 3.1D**. It is composed by two main sequential blocks, the first of which (WINLINFIT) recursively selects a set of candidate change points associated to a potential variation in the slope by means of least square fitting and likelihood evaluation, whereas the second (MERGING) refines the number of change points by hierarchically executing an hypothesis test on adjacent segments.

3.2.1 WINLINFIT

The WINLINFIT module operates on the input trajectory to provide an initial guess for the change points cp_k.

Under the hypothesis that the trajectory is a concatenation of linear segments in the presence of Gaussian noise, performing a least square fitting over each of these segments with a linear model $f(t) = a + bt$ allows to calculate the estimators $\hat{a}_k$and $\hat{b}_k$ (17). Therefore, by applying the principle of maximum likelihood, we obtain that

$$s_k^2 = \frac{\sum_{i=cp_k}^{cp_{k+1}}(a_k t_i + b_k - y_i)}{cp_{k+1} - cp_k + 1} \tag{3.1}$$

The quantity s_k^2 can also be interpreted as the variance of a sample of length $N_k = cp_{k+1} - cp_k + 1$ and its expectation value provides the (biased) estimator of the population variance σ^2. It has been demonstrated that s_k^2 has a Pearson type III probability distribution (18):

$$p(s_k^2, N_k | \, \sigma^2) = \frac{\left(\frac{N_k}{2\sigma^2}\right)^{\frac{N_k-1}{2}} (s_k^2)^{\frac{N_k-3}{2}} e^{-\frac{N_k s_k^2}{2\,\sigma^2}}}{\Gamma\left(\frac{N_k-1}{2}\right)} \tag{3.2}$$

where Γ represents de Gamma function.

Although for the trajectories under examination neither the number $K + 1$ nor the locations of the cp_k are known, in many cases it is possible to obtain an estimation of σ^2, either from control experiments or from the trajectory itself. An example of such kind of procedure is provided in Section 3.2.3. We can thus split the trajectory in all the possible combinations of segments:

$$\sum_{N_k=N_{MIN}}^{N} (N_k - N_{MIN} + 1) = \frac{1}{2}(N_{MIN} - N - 2)(N_{MIN} - N - 1) \tag{3.3}$$

bound by the times t_i and t_j and having length $N_{ij} = j - i + 1 \geq N_{MIN}$ with $N_{MIN} \geq 3$ as imposed by the condition of having a number of points larger than the degrees of freedom for a linear fit. We thus perform a linear fit on each segment and build a matrix:

$$s_{ij}^2 = \frac{\sum_{l=i}^{j}\left(\hat{a}_{ij} t_l + \hat{b}_{ij} - y_l\right)^2}{j - i + 1} \tag{3.4}$$

and evaluate the corresponding likelihood $p_{ij} = p\left(s_{ij}^2, N_{ij} \middle| \, \sigma^2\right)$ by means of **Eq. 3.2**. The segments fully contained in a linear fragment of the trajectory will provide higher value of the probability, whereas those spanning over two or more linear regions will display larger deviations from the expected variance and thus lower p_{ij}'s. We then apply a recursive routine, by means of which the segment with the maximum p_{ij} value is selected and the coordinates of its endpoints (t_i and t_j) are saved as potential slope change points. All the elements of the matrix p_{ij} corresponding to segments having one end point falling within the interval (t_i; t_j) are removed and excluded from the subsequent analysis in the step. The process is repeated until the whole trajectory is segmented in a series of contiguous fragments with change points *cp*.

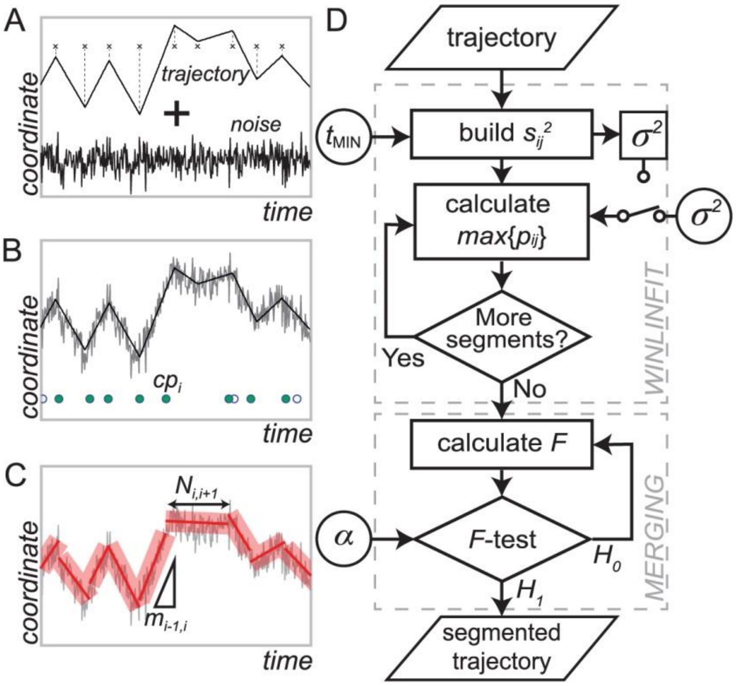

Figure 3.1 The principles of the PLANT algorithm. **(A)** Flow chart of the algorithm, composed by two main blocks: i) the WINDLIFIT, acting on the raw input trajectory to detect points compatible with a change of slope; and ii) the MERGING, assessing the statistical significance of the change points between adjacent segments in order to provide the reconstructed curve. **(B)** Representative simulated input trajectory as a series of joint linear segments corrupted with Gaussian noise. **(C)** The WINDLIFIT block detects points compatible with a change of slope (full and empty symbols), which are further refined by the MERGING block based on their statistical significance (full symbols). **(D)** Reconstructed trajectory from which it is possible to calculate the slopes and durations of each segment as well as their errors.

3.2.2 MERGING

Once the *cp*’s are obtained from the WINLINFIT step, the MERGING block statistically refines their occurrence by hierarchically applying a Fisher test with confidence level α.

The MERGING block consists in testing whether some of the change points correspond to a false positive detection and the adjacent segments can thus be merged. For this, for each pair of adjacent segment (i, j) and (j, k), we test the null hypothesis H_0 that the segments belong to the same linear region (i, k) and there is no change point j between them, versus the alternative hypothesis H_1, i.e. that the segments do correspond to different linear behaviors. In the first case (H_0), we perform a linear fit over the whole region (i, k), whereas in the second case (H_1) two different linear fit are executed. Then, the Fisher statistic is computed as (19):

$$F = \frac{RSS_{H_0} - RSS_{H_1}}{RSS_{H_1}} \left(\frac{N_{ik} - p_{H_1}}{p_{H_1} - p_{H_0}}\right) = \cdots \tag{3.5}$$
$$= \left(\frac{(k-i+1)s_{ij}^2}{(j-i+1)s_{ij}^2 + (k-j+1)s_{ij}^2}\right)\left(\frac{k-i-3}{2}\right)$$

where $RSS_{H_i}$and p_{H_i} are the squared sum of residuals and the number of degrees of freedom associated to the two hypothesis *i* = 0; 1, respectively. We then execute a hypothesis test on the pair of segments showing the minimum *F* value (higher probability to be merged). The value of *F* is compared with the critical value of the Fisher-Snedecor distribution $\mathcal{F}_\alpha$ with level of confidence α. In the case the hypothesis H_0 is accepted, the segments are merged and the Fisher statistic recalculated for the updated list of cp's. The procedure is repeated as long as the segments pair with the minimum *F* verifies the null hypothesis condition $\min\{F\} \leq \mathcal{F}_\alpha$

3.2.3 Automatic estimation of σ^2

When analyzing the time traces, our algorithm needs an estimation of the noise variance σ^2. In many cases, this value can be obtained from calibration measurements, e.g. by tracking immobile objects. However, we devised a method that allows for its online estimation directly on the trace under analysis. The working hypothesis consists in assuming that the time trace is the concatenation of segments of different slopes and duration. On such a trace, as shown in **Eq. 3.4**, we calculate the matrix s_{ij}^2 for all the possible segments with length larger than N_{MIN}. The number of possible segments is given by **Eq. 3.3**. The s_{ij}^2 calculated over regions fully contained in one of the segments of constant slope composing the trace represent a measurement of the variance σ^2, and their expectation value can be used to obtain an estimation of σ^2:

$$\sigma^2 = \frac{N}{N-1}\langle s^2 \rangle \tag{3.6}$$

However, not all the s_{ij}^2 correspond to a measurement of the variance. Since we take all the possible segments, many will overlap with at least one border between two regions of different slope. However, for short segments (i.e., shorter than the average duration of the region of constant slopes), the number of times they lie at the border is negligibly small compared to the times they are fully contained within a constant slope region. By means of numerical simulations, we could show that in most experimental conditions the median of s_{ij}^2 for segments with length ≤ 20 follows, save for a constant, **Eq. 3.6**. Therefore, we included in the algorithm the option of automatically estimating the noise variance by weighted non-linear fitting of the median of the sample variance. The maximum segment length to be considered for the fit can be defined by the user to adapt to situations with a different average length for the regions of different slope.

3.3 Results and Discussion

In this section, we discuss the performance of the PLANT algorithm through some theoretical considerations as well as through the analysis of several sets of simulated data. Finally, we show the ability of PLANT to analyze a dataset obtained from single-cell tracking measurements, which is thoroughly explained and discussed in Chapter 4 (20).

3.3.1 General considerations

The aim of the algorithm is to efficiently and precisely detect the occurrence of a change point corresponding to a variation of slope between two linear segments in the presence of noise. The quantitation of the algorithm performance is obtained through the evaluation of several merit figures, such as the power of detection and the errors on the *cp* location and segment slopes. The trace noise, the slopes and the lengths of the adjacent segments affect the detection of the *cp*. In order to assess how these parameters influence the detection, let's consider a change point *cp* separating two segments $i = 1; 2$ of slopes m_i and lengths N_i (**Fig. 3.2A**). The trajectory coordinate is affected by Gaussian noise with standard deviation σ, therefore at each time point *t* its value shows deviations from the expected value $m_i t$. As a consequence, in a region around the change point position, we will find coordinate values compatibles with both slopes. To obtain a significative change (above a given confidence level) in the *y* coordinate that reveals the occurrence of the *cp*, one must be at a given distance from the *cp*, implying a minimum segment length that depends on the segment slope (**Fig. 3.2A**). Therefore, the power of detection must be a function of the segments slopes m_i, duration N_i and noise σ. Following this semi-quantitative argument, we can obtain a simple geometrical estimation of how the *cp* localization precision,

$$\Delta_{cp} \approx \frac{2\sigma}{|m_2 - m_1|} \tag{3.7}$$

and the corresponding error on the slope,

$$\Delta m_i \approx \frac{4\sigma\Delta_{cp}}{N_i^2 - \Delta_{cp}^2} \tag{3.8}$$

depends on the traces parameters.

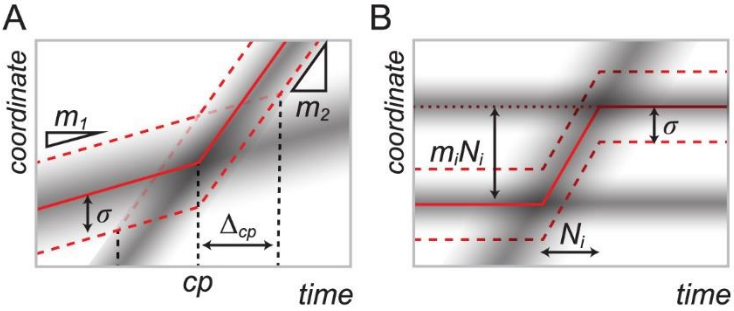

Figure 3.2 Simulations schemes used to calculate algorithm performance. **(A)** The power of detection of a *cp* was calculated by applying the algorithm on simulated traces formed by two segments with slopes m_1, m_2, lengths N_1, N_2 and noise σ; errors on the *cp* location and slopes were obtained from the same data. **(B)** The power of detection of a segment of length N_i was obtained by simulating segments of varying lengths and slopes embedded within two long regions with null slope and noise σ.

Although the scheme depicted in **Fig. 3.2A** is useful to estimate power of detection and localization precision for an "isolated" *cp*, it represents a simplification of the actual situation, in which each segment of the trace (except the first and the last) is embedded within two others. Similarly to what we have previously discussed for the *cp*, in order to be detected, a segment must verify some relation that depends on its length and slopes. As shown in **Fig. 3.2B** for the case of outer segments with same slope equal to zero, this condition is given by $m_i*N_i > 2\sigma$, which for a fixed slope, sets a minimum detectable-segment duration. However, it must be noticed that for large slopes this condition is verified even in the case of very short segments (e.g. $N_i \lesssim N_{min}$), for which the algorithm cannot detect two separated *cp*s but only one. However, since we do not force the reconstructed trace to be continuous at the *cp*, the trajectory will be reconstructed as having an instantaneous jump. In this way, in spite of missing the detection of the inner segment because of the limited time resolution, we could still preserve a high-fidelity reconstruction and the precision in the determination of the neighboring slopes.

3.3.2 Performance of the algorithm

In order to first investigate the performance of our algorithm in identifying a change point, we used numerical simulations. For this, we appealed to a simulation scheme (**Fig. 3.2 A**) made of trajectories composed by two different linear segments with lengths N_1 and N_2, slopes m_1 and m_2 and noise σ. For each set of parameters, in total 500 traces were simulated and analyzed with the PLANT algorithm with α=0.95, as it offers a good tradeoff in the number of false positives *cp* detected. The noise standard deviation was automatically estimated by means of the routine described in Section 3.2.3. In order to quantify the algorithm performance, we evaluated several figures of merit. An important parameter is the power of detection, i.e. the probability of detecting a change in slope when it is known there is a change within the trajectory. The results for the power of detection are summarized in **Fig. 3.3A-C**, where it is seen to depend in a sigmoidal fashion on the noise σ. Expectedly, **Fig. 3.3A** shows that the power of detection markedly depends on segment length. Moreover, traces formed by segments of the same length with different slope values but same slope difference $|m_2 - m_1|$ showed analogous behavior. In addition, larger difference $|m_2 - m_1|$ (**Fig. 3.3B**) produced a higher power of detection. We also investigated traces composed by segments of different length, finding that the power of detection is actually a function of the segment length through the quantity $N^* = 2N_1N_2/(N_1 + N_2)$ (**Fig. 3.3B**).We therefore attempted to express this dependences in a more compact form and we found that the power of detection for all of our simulated conditions collapsed on the same curve (**Fig. 3.3C**) by expressing them in terms of the adimensional variable

$$\xi = \frac{2\sqrt{2\mathcal{N}}\sigma}{|m_2 - m_1|N^*\sqrt{N^*}} \tag{3.9}$$

where $\mathcal{N}$ is a constant with the dimensions of a segment length. Empirically, we also found the power of detection can thus be expressed as:

$$P_{cp}(\xi) = \frac{\mathrm{erf}(1/\xi)^4 + P_\infty}{1 + P_\infty} \tag{3.10}$$

where erf represents the error function and with P_∞ =0.04 and $\mathcal{N}^{1/2} \cong 6$ for all the simulated conditions.

Next, we calculated the precision in the localization of the *cp*, defined as the standard deviation of the distribution of the detected minus the “true” *cp* position. Although the simple calculation performed in the previous section predicts a dependence on noise and slopes only (**Eq. 3.7**), our simulations show a further effect of the segment length and a different scaling as a function of σ depending on the difference in segment length $\Delta N = |N_2 - N_1|$ (**Fig. 3.3D**). We found that for small noise values the observed behavior is well described by the expression:

$$\Delta_{cp} \approx \frac{2\sqrt{2}N\sigma^{\frac{N}{N-\Delta N}}}{3N^*|m_2 - m_1|} \tag{3.11}$$

where $N = N_1+N_2$ is the total trace length. For larger noise, the localization precision seems to asymptotically converge toward a value of ~0.4N, independently on the parameters values.

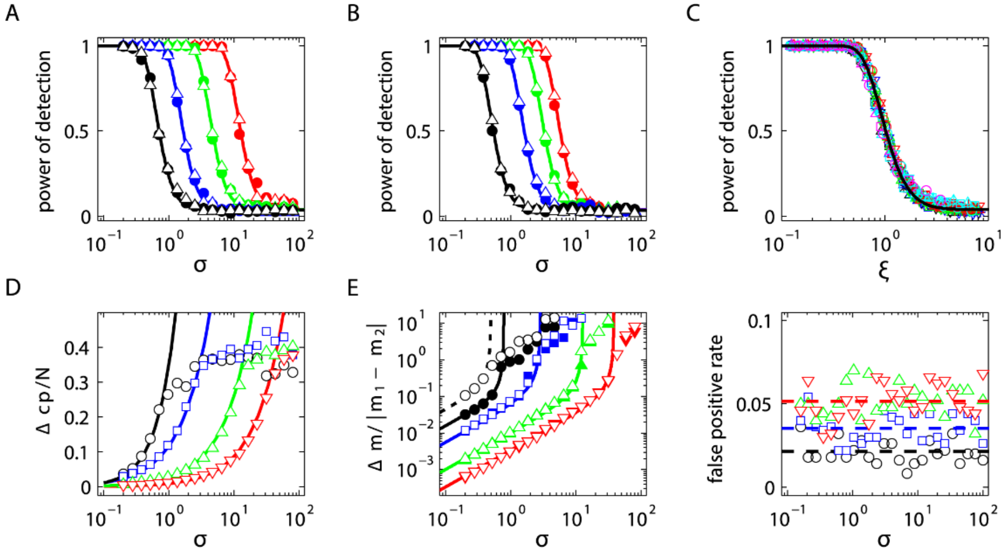

Figure 3.3. Algorithm performance for *cp* detection calculated on the simulation scheme depicted in Fig. 3.2A. (A) Power of detection as a function of the noise σ for segment lengths $N_1 = N_2 = 10; 20; 40; 80$ (represented in black, blue, green and red, respectively) and slopes $m_1 = 0.2; 0.5$, $m_2 = 0.5; 0.8$ (● and △, respectively) with same slope increment $|m_2 - m_1| = 0.3$. **(B)** Power of detection as a function of the noise σ for segment slopes $m_1 = 0.2$ and $m_2 = 0.3; 0.5; 0.8; 1.3$ (represented in black, blue, green and red, respectively) and lengths $N_1 = 13$; $N_2 = 30$ (●) and $N_1 = N_2 = 20$ (△) with a fixed $N^* = 20$. **(C)** Power of detection for several segments lengths and slopes collapse onto each other once rescaled to the variable ξ (**Eq. 3.9**). Lines in (A-C) correspond to fits to the function given in **Eq. 3.10**. **(D)** Change point localization precision normalized to the trace length for same segments slope ($m_1 = 0.2$; $m_2 = 0.3$) and lengths $N_1 = 20$, $N_2 = 40$ (○) or $N_1 = N_2 = 80$ (□); same segments length ($N_1 = N_2 = 80$) and slopes $m_1 = 0.2$, $m_2 = 0.5$ (△) or $m_1 = 0.2$, $m_2 = 1.1$ (▽). **(E)** Error in the determination of the segment slopes normalized to the modulus of slopes difference. Symbols have the same meaning as in panel D. Empty or filled symbols refer to the two different segments of the simulated trace. **(F)** False positive identification rate obtained for $m=0.1$ and length $N=40$ (○); $m=0.1$ and $N=80$ (□); $m=0.1$ and $N=150$ (△); or $m=1.1$ and $N=150$ (▽). Each point in the plot was obtained from 500 simulated traces.

We also evaluated the error on the detected slopes, as displayed in **Fig. 3.3E**. According to the calculation reported in **Eq. 3.8**, Δm_i is found to be independent on the segment slopes and to scale linearly with the noise. However, it shows a more complex dependence on the difference in segment lengths that, for small noise can be expressed as:

$$\Delta m_i \approx \frac{4\sigma\sqrt{N_i}}{N_i^2 - \Delta_{cp}^2 \left(\frac{N}{N+\Delta N}\right)^4} \tag{3.12}$$

Last, in **Fig. 3.3F** we report on the false positive rate (FPR), i.e. the probability of detecting a change point where it actually there is no change point. To measure this quantity we simulated traces of only one segment with length N, slope m and noise σ. The data show that the algorithm is robust toward the detection of false positive and show high specificity, with FPR<1% for all the simulated cases. Expectedly, the FPR depends weakly on the length of the segment but it does not vary with m nor with σ. The latter is due to the fact that statistical tests performed by the algorithm explicitly take into account the presence and value of the noise.

As we have already anticipated in the previous section, the actual scenario to which the algorithm is meant to be applied is more complex than the simulation scheme depicted in **Fig. 3.2A**. This is because each segment of the trace is embedded within two others with different slopes and durations. Moreover, both a missed change point and a false positive detection will affect the determination of the parameters of the neighboring segments in a complex way that ultimately depends on the distribution of slopes and durations of the trace. Therefore, the specific performance of the algorithm must be evaluated in every specific case by means of simulations. However, in order to provide a flavor of the ability of the algorithm to correctly identify a segment in a more realistic scenario, we use another simulation scheme (**Fig. 3.2B**), where a test segment of varying slope and duration is embedded within two very long ones having null slope for different noise levels. The choice of the null slope does not limit the generality of these calculations since, as we have shown in **Eqs. 3.9** and **3.10**, the power of detection only depends on the slope difference $|m_2 - m_1|$. The results of the algorithm applied over 500 simulations for each condition are reported in **Fig. 3.4**. Expectedly, the power of detection for a full segment has a nearly sigmoid behavior similar to that reported for a single *cp* in **Eq. 3.10**. Deviations from this behavior can be observed for small slope values and segments of length N~10, where the power of detection displays a little shoulder. This feature is likely due to the combination of the detection of a “real” *cp* plus a false positive detection, resulting in spurious segment identification. In fact, this behavior is observed in the regime $N < 2\sigma/m$ (empty symbols in **Fig. 3.4A**), where - as discussed previously - the values of noise, length and slope make the trace compatible with no segment change. As the simulated segment length and/or the slope are increased (or the noise reduced), the *cp* detection power increases and this also produces a decrease in the false positive rate. Consequently, the power of detection for the full segment starts growing with the expected scaling. In order to show how the algorithm performs at different noise levels, we also report the dependence of $N_{50\%}$, i.e. the segment length at which the power of detection reaches 50%. According to **Eq. 3.9**, we find that indeed $N_{50\%}$ shows the expected power law behavior ~$(\sigma/m)^{2/3}$ (**Fig. 3.4B**).

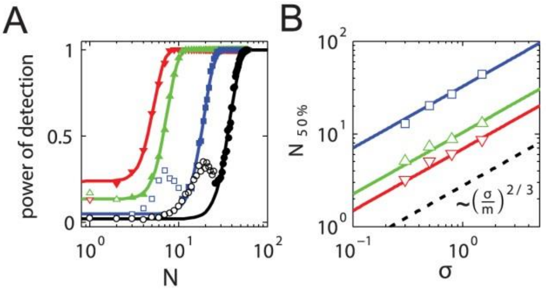

Figure 3.4: Algorithm performance for the detection of a segment according to the simulation scheme of Fig. 3.2B. (A) Power of detection as a function of the segment length *N* for σ=0.5, and slopes *m* =0.04 (●), 0.1 (□), 0.5 (△) and 1 (▽). The lines are the results of best fit according to **Eq. 3.10**. Empty symbols refer to the condition $N < 2\sigma/m$. **(B)** Segment length $N_{50\%}$ providing a 50% power of detection as a function of the trace noise σ for slopes m =0.1 (□), 0.5 (△) and 1 (▽). Lines correspond to a power law fit ~ $(\sigma/m)^{2/3}$=3. The dashed line is a guide to the eye.

3.3.3 Application of the algorithm to the analysis of trajectories from cell tracking experiments

The complex behavior and the function of living cells is the result of a myriad of biochemical reactions occurring at the molecular level (21), influenced by the molecular diffusion and by the spatial organization of the cellular components. An example of this involved interplay is represented by the migration of leukocytes across endothelial cells (ECs) during the immune response (22), as described in Chapter 1. The interaction between these two types of cells is mainly mediated by the transient binding of integrins placed on the leukocyte membrane to their counter-receptors on the ECs surface (23, 24). Moreover, it is known that under certain conditions integrins can spatially re-organize in clustered structures (25, 26). Such a clustering produces an increased local concentration that effectively changes the kinetics of interaction to their ligands (avidity). The kinetics of these interactions, in turns modulates leukocytes migration on ECs (27). Thus, the changes in the motion of leukocytes on ECs during the immune response are ultimately determined by the mechanism of interactions at molecular level (see also Chapter 4). In addition, it must be considered that these phenomena take place in environments such as lymph nodes and blood vessels, where mechanical cues such as shear forces play a major role. In order to study this mechanism in relation with the role of integrins

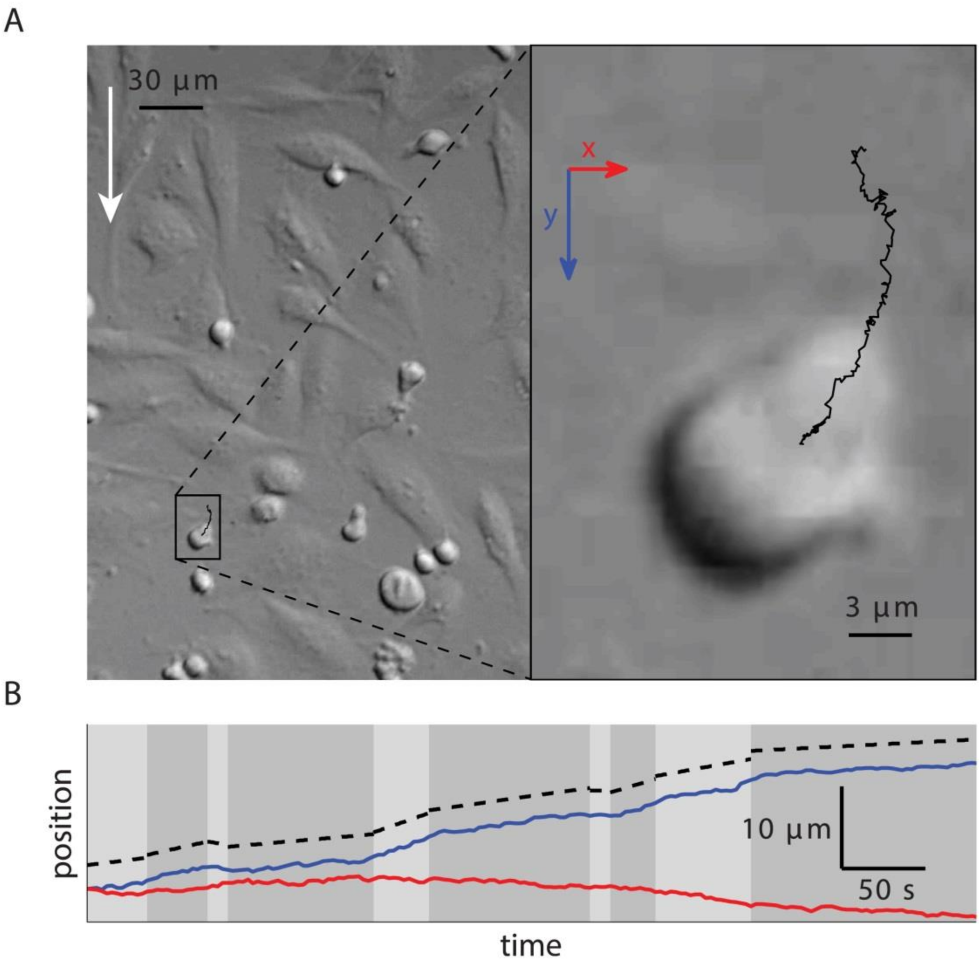

Figure 3.5 Cell tracking experiments and time trace analysis. (A) Movie frame of a typical experiments consisting in monitoring the motion of T-cells on ECs in the presence of shear flow (*left*) and zoom in of the region within the box (*right*) with overlaid trajectory. The flow is applied along to the positive *y* direction. The white arrow indicates the direction of the flow. **(B)** Time traces of the ***x*** and ***y*** coordinates of the position of the cell represented in panel A. Shaded gray regions correspond to regions where the algorithm detected changes of slope. The dashed line represents the piecewise reconstructed trace of the *y* trajectory that has been shifted upwards for clarity.

in the immune function and the effect of mechanical forces, we performed cell tracking experiments under the presence of a laminar flow. The motivation and detailed results obtained from these experiments area fully described in Chapter 4. In here we essentially focus on the validation of the PLANT algorithm to quantitatively analyze T-cell trajectories. In brief, we first grew cytokine-stimulated ECs in a parallel-plate flow chamber (PPFC) and subjected the cells to four hours of continuous shear-flow stimulation. T-cells were then injected into the chamber and allowed to adhere for 3 min, after which we applied a flow of 1 dyn/cm^2 and used DIC video microscopy to record movies for ~20min at 0.33Hz. A snapshot of a recorded movie is shown in **Fig. 3.5A.** We used a custom written routine (see Methods) to track the centroid position of leukocytes. Typical time traces of the cell centroid coordinates in the direction perpendicular (x) and parallel (y) to the flow are shown in **Fig. 3.5B**.

Leukocytes display heterogeneous motions, which at the experimental time resolution appear as composed by a concatenation of segments each with an approximately constant velocity but with large velocity variations between different segments, including reversing the velocity by moving against the flow direction ($v_y < 0$). Therefore, we applied our algorithm to a set of experimentally collected time traces to automatically characterize the different features in the cells motion. The result of the algorithm applied on the y coordinate of the cell centroid position is shown in **Fig. 3.5B**, where the shaded gray regions correspond to the detected changes of slope and the dashed line represents the piecewise reconstructed trace, which has been shifted up for clarity. The same analysis was applied to 50 experimental traces with duration of 400-600 s, and the distribution of slopes (velocities) and segment lengths (times) obtained were represented as histograms (**Fig. 3.6)**. In order to verify whether the motion along or against the flow had different characteristics, the data corresponding to the duration of the segments (**Fig. 3.6A**) were split based on the sign of the velocity component along the flow direction v_y, which is reported in **Fig. 3.6B**. Both distributions show an asymmetric shape,

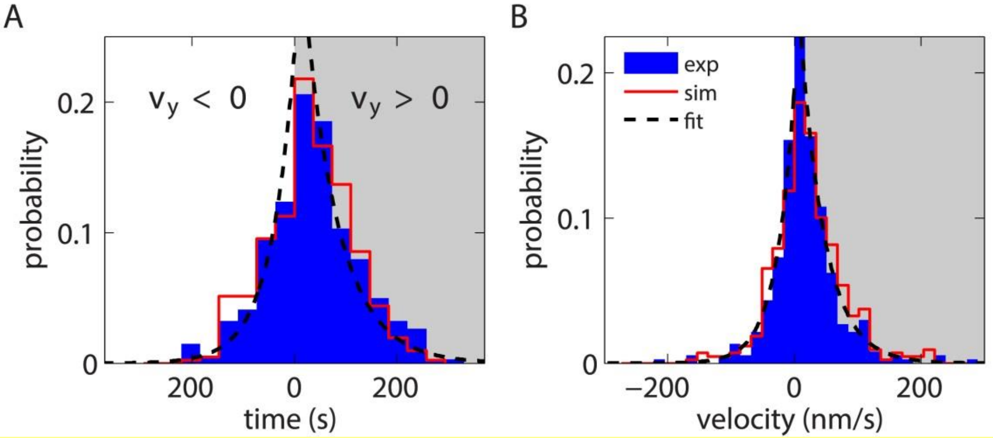

Figure 3.6 Analysis of cell tracking experiments with the PLANT algorithm. (A) Histogram of the time duration of the detected segments, divided according to the direction of the y-component of the velocity along (gray shaded area) or against (white area) the shear flow. **(B)** Histogram of the y-component of the velocity of the detected segments. In both panels, the blue bars correspond to experimental data, the dashed black lines are exponential fits to the experimental data and the red lines are the resulting distributions of velocities and times after applying the algorithm to simulated data.

reflecting the fact that the leukocytes move along the flow with higher probability. In spite of this preference, the molecular interactions established by cells allow to sustain the motion with non-negligible speed against the shear. We attempted to obtain a more quantitative insight from these data in order to link the observed features to molecular mechanisms such as integrin-ligand interactions, actin polymerization and the action of molecular motors such as myosin (27, 28). The histograms in **Fig. 3.6**, corresponding to the experimental data (blue bars) are characterized by exponential tails at long times and velocities, as shown by the dashed lines. Although one would be tempted to extract the characteristic times and velocities by fitting the experimental distributions to single exponential functions, this straightforward approach will result in an overestimation of these parameters with respect to the real values. This is because due to the time resolution of the experiments, the PLANT algorithm might miss short events that would in turn result in the detection of artificial long events. As briefly discussed in previous section, the knowledge of the performance of the algorithm is crucial to avoid these artifacts caused by a limited power of detection of short segments. However, this information cannot be easily obtained when dealing with "real" data, since it strongly depends on the (a priori unknown) distribution of segment duration and slopes, as well as on the relative positioning of segments. Therefore, to obtain a robust estimation of the kinetic parameters and retrieve their real values, we performed numerical simulations. We generated 50 synthetic traces with duration of 450 s composed by contiguous segments, whose duration and slope were randomly generated. The traces were corrupted with the noise value $\sigma = 0.2$, as estimated for the experimental data. We assumed exponential distributions for segment duration and slope similar to the experimental data, but where the characteristic values of these distributions and the relative probability of switching direction were varied. Since our algorithm will equally affect the simulated trajectories and the experimental ones, we varied the parameters of our simulated trajectories so that after applying our algorithm to them we could retrieve the same distribution values as the ones obtained after applying the algorithm to the experimental data. The distribution of times and velocities obtained by applying the algorithm to the simulated trajectories were then subjected to the same procedure than the experimental data, i.e., they were separated according to sign of the velocity and then fitted to exponential functions. The results of these fits were compared to the results of the fits performed on the experimental data after being segmented. By means of this procedure, we could find a set of parameters that could nicely reproduce our experimental results (red lines in **Fig. 3.6**). This allowed us to estimate the real parameters of the distributions, overcoming the limitations of instrumental resolution and algorithm limited performance. The results showed that the velocity of leukocytes is affected by shear flow. They move along the flow direction with an average speed of 39 ± 6 nm/s, which decreases to 29 ± 5 nm/s when opposing the flow. The typical duration of a segment travelled at nearly constant speed is of 35 ± 6s independently of the direction, producing an average path of ~1.4µm in the positive and ~1µm in the negative direction. In addition, the cells spend 2/3 of the time travelling along the flow.

3.4 Summary

In this Chapter we introduced PLANT, a bottom-up type of algorithm for detecting changes of slopes in time trace curves affected by a Gaussian noise. Unlike others algorithms based on PLA, PLANT does no impose any conditions on the number of segments or the error in the data. In fact, here we propose a method for estimating the unknown noise from the data (as long is Gaussian). In addition, in order to test the performance of the algorithm we performed numerous simulations. The results show that our algorithm could robustly reconstruct noisy trajectories and, as expected, the power of detection of *cp* decreased as the length of the segment decreases or the noise increased. Moreover, we found a functional dependence between the power of detection of a single *cp* and the segments length, slope and noise. Finally, we applied the algorithm on a set of experimental data obtained by tracking the position of T-cells on ECs. These results provide a first test of the ability of our algorithm to extract valuable information from noisy trajectories. The values of cell velocity and segment duration that can be obtained by means of our algorithm thus constitute relevant microscopic parameters, which can be used to validate molecular models of cell migration and thus better understand the role played by molecular interactions. In Chapter 4 we will further discuss how the characteristics of the T-cell motion correlate with the biological mechanisms that operate at molecular level.

3.5 Material and Methods

Shear flow experiments and imaging. Experiments were performed using a PPFC (see Chapter 2). Briefly, ECs were first stimulated with TNF-α (10 ng/ml) for 20 h, assembled into the PPFC and mounted in an inverted microscopy (Olympus IX71). Jurkats T-cells (~$1.5x10^6$ cells) were then injected into the chamber at 0.3 dyn/cm^2 using RPMI-1640 perfusion medium. Once inside the chamber, the flow was stopped for 3 min to allow the T-cells to adhere on ECs. Finally, the flow was resumed at 1 dyn/cm^2 and kept constant for 20 min. Movies of T-cells movement were recorded using DIC microscopy at 3 frame/s. A box built around the microscopy allowed maintaining the PPFC system at 37ºC during the time of measurements. More experimental details are given in Chapter 4.

Cell tracking algorithm. We developed an algorithm to automatically track the 2D motion of lymphocytes on ECs imaged by means of Differential Interference Contrast (DIC) microscopy. The algorithm, implemented in MATLAB, is based on the maximization of the image cross-correlation (29) function together with morphological transformation and thresholding to automatically track the cell centroids. The image cross correlation function allows quantifying how well a given template matches with the different regions of a larger image. Hence, the maximum of the cross correlation indicates the region of an image that best matches with the template. The algorithm works as follows: first, a region of interest (ROI) is manually selected from the initial frame. The ROI typically consists in a small rectangular region including the cell to be tracked (**Fig. 3.7A**). The selected ROI is used as a template image to find the same cell within the next frame by means of the maximization of the cross correlation. This procedure is iterated through all the movie frames. The template image is updated at every frame to take into account changes of cellular shape during the duration of the movie. This was a valid approach since T-cell shape only changed significantly at time scales longer than the sampling rate used (3 s). On the other hand, to avoid possible mismatching events due to the presence of cells with similar shape within the same frame, only sub-regions of the images close to the cell position in the previous frame were selected to maximize the cross correlation function. The size of these sub-regions was defined by the user by introducing into the program a maximum distance covered by the cell between two consecutive frames. In this way, the algorithm is able to successfully follow the same cell throughout the whole movie. However, in order to obtain a more precise determination of the cell centroid coordinates, we perform further image processing. From **Fig. 3.7A** it can be seen that the DIC video microscopy produces characteristic cell patterns, consisting in juxtaposed dark and bright area with 45° orientation respect to the image axes (29). Simple thresholding allows isolating the dark and bright features. In addition, the gradient of the image is larger at the edge between dark and bright regions. Pixels showing large gradients were used to obtain a digitized image that was summed to those obtained from the thresholding of dark and bright features. Such a map is then filled through image dilation and provides a reconstruction of the area covered by the cell. The cell centroid is then calculated as the center of mass of the map.

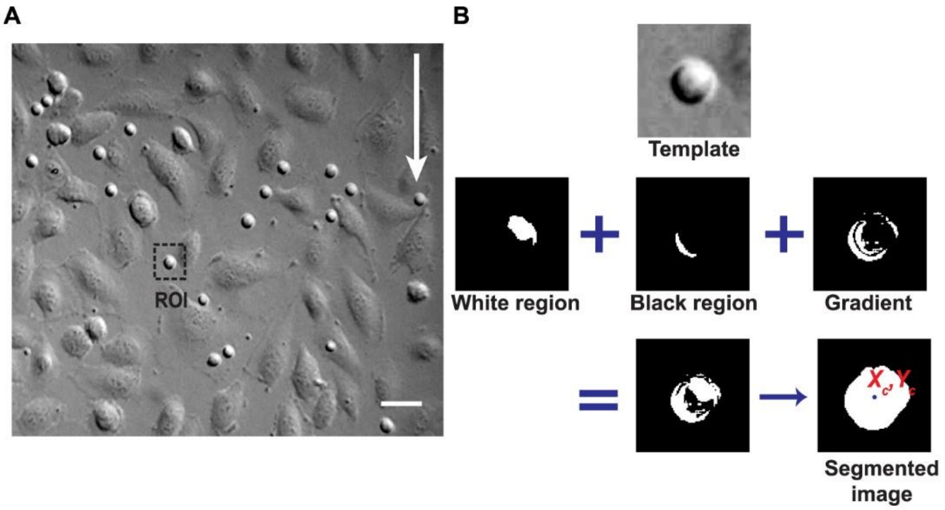

Figure 3.7 General procedure of cell tracking algorithm. (A) Representative DIC image of lymphocytes (nearly rounded cells) moving on ECs (larger and spread cell) under the influence of shear flow. The white arrow indicates the direction of the shear flow. Scale bar represents 30 µm. At each frame, a ROI (30×30 µm^2) around the cell to be tracked is automatically selected and used as a template for the next frame. **(B)** Template corresponding to the ROI depicted in (A) (upper panel). Black and white images resulting from applying different thresholds to the original template in order to enhance the bright (middle panel left), dark region (middle panel center) and large gradient regions (middle panel right). Digitized map resulting from adding up the images obtained from the 3 different thresholdings (lower panel left). Final segmented image obtained by filling the empty spaces of the previous step image (lower panel right). The final segmented image is used to precisely determine the coordinates of the cell centroid.

3.6 References

1. Haber C., and Wirtz D., Magnetic tweezers for DNA micromanipulation. *Rev. Sci. Instrum.*, (2000) **71**, 4561–4570.
2. Yan J., Skoko D., and Marko J. F., Near-field-magnetic-tweezer manipulation of single DNA molecules. *Phys. Rev. E*, (2004) **70**, 011905.
3. Capitanio M., Canepari M., Maffei M., Beneventi D., Monico C., Vanzi F., Bottinelli R., and Pavone F. S., Ultrafast force-clamp spectroscopy of single molecules reveals load dependence of myosin working stroke. *Nat. Methods*, (2012) **9**, 1013–1019.
4. Yildiz A., Forkey J. N., McKinney S. A., Ha T., Goldman Y. E., and Selvin P. R., Myosin V Walks Hand-Over-Hand: Single Fluorophore Imaging with 1.5-nm Localization. *Science*, (2003) **300**, 2061.

5. D´ecav´e E., Rieu D., Dalous J., Fache S., Br´echet Y., Fourcade B., Satre M., and Bruckert F., Shear flow-induced motility of Dictyostelium discoideum cells on solid substrate. *J. Cell Sci.*, (2003) **116**, 4331.
6. Thomas W., Forero M., Yakovenko O., Nilsson L., Vicini P., Sokurenko E., and Vogel V., Catch-Bond Model Derived from Allostery Explains Force-Activated Bacterial Adhesion. *Biophys. J.*, (2006) **90**, 753–764.
7. Keogh E., Chakrabarti K., Pazzani M., and Mehrotra S., Dimensionality Reduction for Fast Similarity Search in Large Time Series Databases. *Knowl. Inf. Syst.*, (2001) **3**, 263-286.
8. Hamann B. and Chen J.-L., Data point selection for piecewise linear curve approximation. *Comput. Aided Geom. Des*., (1994) **11**, 289–301.
9. Popivanov I. and Miller R. J., Similarity search over time-series data using wavelets. *Proc. 18th International Conference on Data Engineering,* (2002), 212–221
10. Perng C. S., Wang H., Zhang S. R., and Parker D. S., Landmarks: a new model for similarity-based pattern querying in time series databases. *Proc. 16th International Conference on Data Engineering,* (2000), 33–42.
11. Keogh E. J., Chu S., Hart D., and Pazzani M. J., An Online Algorithm for Segmenting Time Series, *Proc. of the 2001 IEEE International Conference on Data Mining,* (2001), 289–296.
12. Shatkay H. and Zdonik S. B., Approximate Queries and Representations for Large Data Sequences, *Proc. of the Twelfth International Conference on Data Engineering*, (1996), 536–545.
13. Chu C.-S. J., Time series segmentation: A sliding window approach. *Inf. Sci***.**, (1995) **85**, 147–173.
14. Hunter J. and McIntosh N., Knowledge-Based Event Detection in Complex Time Series Data, *Artificial Intelligence in Medicine: Joint European Conference on Artificial Intelligence in Medicine and Medical Decision Making*, (1999), 271–280.
15. Vasko K. T. and Toivonen H. T. T., Estimating the number of segments in time series data using permutation tests. *Proc. Data Mining*, (2002), 466–473.
16. Terzi E. and Tsaparas P., Efficient Algorithms for Sequence Segmentation. *Proc. of the Sixth SIAM International Conference on Data Mining*, (2006), 314–325.
17. Kenney J F., and Keeping, E. S. Mathematics of Statistics. *2nd Ed. New York: Van Nostrand*. (1951).
18. Singh V. P., Entropy-Based Parameter Estimation in Hydrology, Chapter 4: Pearson Type III Distribution. *Springer Netherlands.* (1998), 231-251.

19. Snedecor G. W., and Cochran W G., Statistical Methods. *8th Ed. Iowa State: University Press*. (1989).
20. Piechocka I. K., Sosa-Costa A., Mohan N., Lakadamyali M., Manzo C., and Garcia-Parajo M. F., Shear flow-driven actin re-organization regulates ICAM-1 nanopatterning on endothelial cells. (*In preparation*).
21. Hood J. D. and Cheresh D. A., Role of integrins in cell invasion and migration. *Nat. Rev. Cancer*, (2002) **2**, 91–100.
22. Ley K., Laudanna C., Cybulsky M. I., and Nourshargh S., Getting to the site of inflammation: the leukocyte adhesion cascade updated. *Nat. Rev. Immunol*., (2007) **7**, 678–689.
23. Makgoba, M. W., Sanders, M. E., Luce, G. E. G., Dustint, M. L., Springer, T. A., Clark, E. A., Mannoni, P., and Shaw, S., ICAM-1 a ligand for LFA-1-dependent adhesion of B, T and myeloid cells. *Nature*, (1988) **331**, 86–88.
24. Oppenheimer-Marks, N., Davis, L. S., Bogue, D. T., Ramberg, J., and Lipsky, P. E., Differential utilization of ICAM-1 and VCAM-1 during the adhesion and transendothelial migration of human T lymphocytes. *J. Immunol*., (1991) **147**, 2913–2921.
25. van Zanten T. S., Cambi A., Koopman M., Joosten B., Figdor C. G., and Garcia-Parajo M. F., Hotspots of GPI-anchored proteins and integrin nanoclusters function as nucleation sites for cell adhesion. *Proc. Natl. Acad. Sci. USA*, (2009) **106**, 18557–18562.
26. Kim M., Carman C. V., Yang W., Salas A., and Springer T. A., The primacy of affinity over clustering in regulation of adhesiveness of the integrin αLβ2. *J. Cell Biol*., (2004) **167**, 1241–1253.
27. Maheshwari, G., Brown, G., Lauffenburger, D. A., Wells, A., and Griffith L.G., Cell adhesion and motility depend on nanoscale RGD clustering. *J. Cell Sci*., (2000) **113**, 1677–86.
28. Bangasser B. L., Rosenfeld S. S., and Odde D. J., Determinants of Maximal Force Transmission in a Motor-Clutch Model of Cell Traction in a Compliant Microenvironment. *Biophys. J.,* (2013) **105**, 581-592.
29. Gelles, J., Schnapp, B., and Sheetz M., Tracking kinesin-driven movements with nanometre-scale precision. *Nature*, (1988) **331**, 450–453.

Chapter 4

Shear flow-driven actin re-organization regulates ICAM-1 nanopatterning on endothelial cells

Mechanical forces exerted by cells, the surrounding tissue and shear blood flow are capable of modifying cellular adhesions mediated by integrin receptors and their counterpart ligands. However, very little is known about the effect of shear forces on the spatial organization of ligand receptors that constitute along with integrins the main components of cellular adhesions. Here, using a parallel-plate flow chamber (PPFC) device together with confocal and super-resolution microscopy, we show that shear flow induces a global translocation of the Intracellular Adhesion Molecule-1 (ICAM-1) expressed on endothelial cell (ECs) to the upstream direction of flow. Remarkably, this change in ICAM-1 spatial distribution is accompanied by the formation of ICAM-1 nanoclusters that co-localize with shear-force induced actin-enriched "patch"-like structures. T cells adhered to mechanically pre-stimulated ECs develop a more pro-migratory phenotype and migrate faster with shorter EC interaction periods compared to their counterparts adhered to static ECs. We rationalize our results considering a model based on the motor-clutch hypothesis, whereby the strengthening of the clutches (ICAM-1-αLβ2 bonds) reduces the actin retrograde flow of T-cells, thus increasing their forward velocities, while an increase in substrate effective stiffness shortens the times of interaction with ECs. According to this hypothesis, T-cell velocity is increased as a result of the amplified strength of the clutches due to the increased number of integrin-ligand interactions brought about by shear forces. On the other hand, the reinforcement of ICAM-1 anchorage to the actin cytoskeleton induced by the shear flow promotes the early breaking of the bonds, which is translated in shorter times of interaction. Overall, our results reveal that continuous shear flow directly modulates the spatial organization of cell adhesion receptors influencing in turn leukocyte migration behavior.

This work is currently under preparation to be submitted in *J Cell Sci.:* I. K. Piechocka, A. Sosa-Costa, N. Mohan, M. Lakadamyali, C. Manzo and M. F. Garcia-Parajo. "Shear flow-driven actin re-organization regulates ICAM-1 nanopatterning on endothelial cells"

4.1 Introduction

Endothelial cells (ECs) form a natural barrier for regulating leukocyte migration within blood vessels. Leukocyte extravasation from the bloodstream to sites of inflammation or peripheral lymphoid organs involves a cascade of steps of leukocyte interactions with the activated endothelium. This multistep process includes initially low-affinity adhesive interactions (capture and rolling) (1), followed by firm adhesion (2), cell spreading and crawling (3), and finally leukocyte diapedesis through the endothelial barrier to the sites of inflammation (4, 5). Supported by different types of cellular adhesion molecules such as L-, P- and E-selectins, intracellular adhesion molecule-1 (ICAM-1; CD54), vascular adhesion molecule-1 (VCAM-1) and platelet-endothelial adhesion molecule (PCAM) (6) the endothelium plays therefore a pivotal role during inflammatory response.

The mechanism of leukocyte firm adhesion to the endothelium and subsequent migration is mainly mediated by specific interactions between the ligand ICAM-1 expressed by ECs and its leukocyte counter-receptor, the αLβ2 integrin lymphocyte function-associated antigen (LFA-1; CD11a/CD18) (7, 8). Although ICAM-1 is constitutively expressed on the EC surface at very low levels, its expression is enhanced in response to inflammatory cytokines such as tumor necrosis factor-α (TNF-α) or thrombin (9, 10), favoring in increased leukocyte adhesion to the endothelium. In addition, integrin-mediated leukocyte adhesion to such biochemically activated endothelium has been shown to generate a specific distribution of ICAM-1 into F-actin rich docking structures surrounding the basal membrane of tightly adherent leukocytes (11-13) and/or clustering of ICAM-1 in ring-like structures around leukocytes adherent sites (14-16) prior to diapedesis. Such an increase in ICAM-1 concentration in the leukocyte-EC contact area is believed, on the one hand, to enhance the stability of ICAM-1 platforms by decreasing ligand mobility (16, 17) and incorporating them into lipid rafts (18, 19). This potentially promotes more stable adhesion. On the other hand, continuous rearrangement of ICAM-1 upon leukocyte engagement and movement suggests a diffusive nature of ICAM-1 that stays in contact and continues to follow the leukocytes during the whole transmigratory process (8, 11, 14, 15).

Due to their localization on the EC surface, ICAM-1 molecules are continuously exposed *in vivo* to fluid shear stresses generated by blood flow. These ligands therefore not only have to withstand traction forces exerted by crawling leukocytes but also have to resist forces generated by flowing blood. It has been previously shown that shear force up-regulates the expression level of ICAM-1 (20, 21), modulates EC gene regulation (22, 23), induces cell shape and actin cytoskeleton organization (24), focal adhesions formation (25) and changes in membrane fluidity (26-28). Moreover, the initially formed ligand-integrin bonds (29-31) become enhanced as a result of integrin activation brought about by shear forces (2, 32-36). This leads to increased leukocyte binding to endothelium (21, 37), which in turn promotes transendothelial migration (38).

Although the influence of shear forces on ECs has been studied extensively, the direct effect of forces on the spatial distribution of adhesion molecules on the apical EC surface prior to leukocyte adhesion has received less attention. Moreover, it is also unclear how pre-exposure of ECs to fluid shear-stress affects leukocyte cell migratory behavior. To address these questions, we pre-exposed inflammatory challenged ECs to continuous shear flow prior to T-cell adhesion and followed over time the spatial distribution of ICAM-1 and the actin cytoskeleton. We show that ICAM-1 molecules are part of the shear-sensitive EC machinery that rearrange in the response to continuous flow forming nanoclusters on the EC surface that are highly localized upstream of flow. This particular spatial organization appears to be driven by actin-cytoskeleton re-arrangements induced by shear-forces. ICAM-1 nanoclustering might contribute to strengthen interactions with integrins expressed on T cells allowing T cells to exert larger traction forces needed for migration over the endothelium.

4.2 Results

ICAM-1 expression and membrane localization on ECs are sensitive to biochemical and mechanical stimulation. ECs together with their cell surface receptors are continuously exposed *in vivo* to fluid shear stress generated by blood flow. To first investigate the effect of flow-related shear stress on ICAM-1 expression and distribution at the single cell level, we exposed resting ECs to a continuous shear flow of 8 dyn/cm^2, similar to the flow values reported in blood vessels (39). We fixed ECs at different time points after shear flow stimulation, labelled ICAM-1 and visualized its overall distribution on individual cells by confocal microscopy. In static conditions, ICAM-1 was barely detectable, consistent with its low expression level (20, 21), and uniformly distributed along the basal and apical membranes as well as intracellularly (**Fig. 4.1A, left**). Application of shear stress did not induce noticeable changes on the overall ICAM-1 spatial distribution (**Fig. 4.1A, right**). Quantification of the total fluorescence intensity over multiple cells showed a gradual increase on the ICAM-1 signal as a function of shear exposure with a two-fold increase over the course of six hours **(Fig. 4.1B)**. These results indicate that exposure to shear flow up-regulates ICAM-1 expression on ECs, in agreement with earlier flow cytometry studies (20, 21).

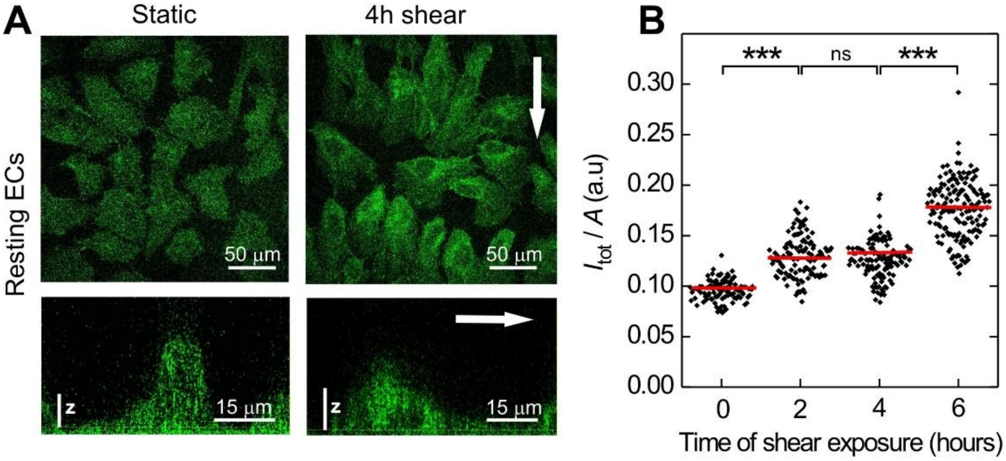

Figure 4.1 Effect of shear flow in the spatial organization of ICAM-1 (A) Single plane confocal microscopy images taken at the basal cell membrane (*top rows*) and 3*D* orthogonal views *(bottom rows*) of ICAM-1 expressed on resting ECs, in absence of shear flow (*left column*) and after 4h of continuous flow application (*right column*). White arrows indicate the direction of shear flow. Contrast has been adjusted so that the weak ICAM-1 signal can be observed in the images. **(B)** Fluorescence intensity of the ICAM-1 signal integrated over the entire cell and normalized to the cell area, for static conditions (0 h) and for different times of shear exposure (2, 4 and 6 h). Horizontal red lines indicate the mean values. In total, 100 to 180 ECs from two separate experiments were analyzed per condition.

Next, we tested the effect of prolonged shear stress exposure on the expression levels and spatial distribution of ICAM-1 in the presence of inflammatory conditions. For this, we stimulated ECs with TNF-α, an inflammatory cytokine that induces up-regulation of ICAM-1 expression (40). In the presence of shear flow TNF-α-stimulated ECs become elongated and aligned along the flow direction while in static conditions cells were randomly oriented (**Fig. 4.2,** *upper row*). To quantify the changes in cell orientation we calculated the angle formed between the major axis of the cell and the direction of the flow. While in static conditions the angle of ECs orientation respect to the flow was homogenously distributed between 0 and 90°, in the presence of shear flow stimulation it was confined between 0 and 60° (**Fig. 4.2,** *bottom row*).

Moreover, TNF-α treatment resulted in translocation of the cytoplasmic pool and *de novo* expression of ICAM-1 on the endothelial apical membrane (**Fig. 4.3A,** *left*) together with a six-fold increase in the total ICAM-1 intensity compared to resting (in the absence of TNF-α) ECs (compared **Fig. 4.1B** with **Fig. 4.3B**, at 0 hours). Application of shear flow did not substantially increase further ICAM-1 expression on TNF-α-treated cells, with only a modest but significant increase after six hours of shear exposure (**Fig. 4.3B**).

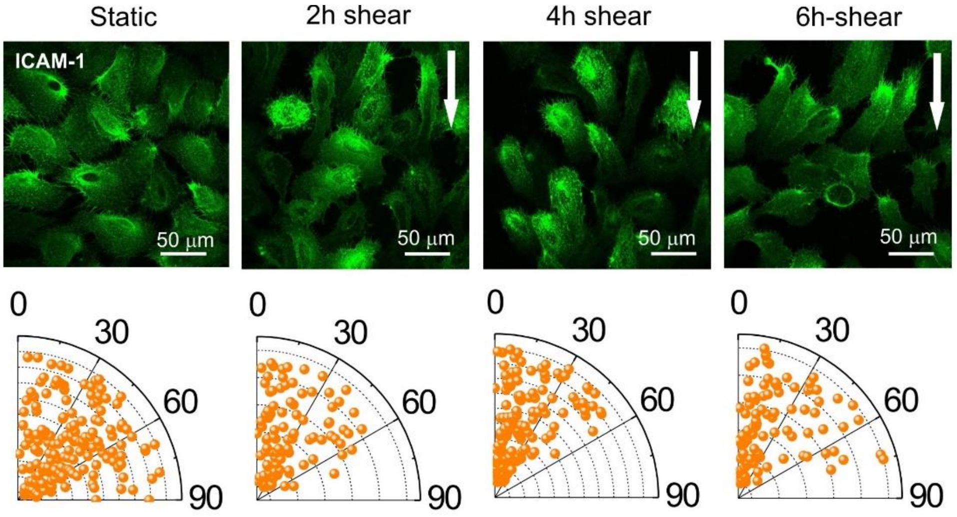

Figure 4.2 Effect of shear flow on cell alignment in TNF-α stimulated ECs. (*First row*) Confocal images of ICAM-1 in the absence of shear flow and after different times of shear exposure. The images are z-projections of 80 confocal frames over 8 µm distance. White arrows indicate the direction of the shear flow. (*Second row*) Distribution of the angles formed between the major axis of ECs and the direction of the flow, for static conditions and after different periods of shear flow stimulation. In total, 100 to 180 ECs from two separate experiments were analyzed per condition.

Interestingly, shear conditions induced a strong translocation of ICAM-1 at the apical membrane upstream of the flow direction (**Fig. 4.3A** *right*, yellow arrows). This specific ICAM-1 enrichment was already visible after two hours of shear exposure and it was maintained over six hours of shear flow measurements (**Fig. 4.4**). These results thus show a synergistic effect of biochemical and mechanical stimulation on the expression and spatial distribution of ICAM-1 on ECs. While TNF-α mainly up-regulates expression and induces translocation to the apical membrane, shear stress leads to cell elongation and pronounced re-location of ICAM-1 upstream of flow.

Shear stress modulates upstream ICAM-1 localization and actin cytoskeleton organization. It has been extensively documented that application of shear stress induces endothelial cell shape changes, elongation and formation of actin stress fibers aligned to the flow direction (41). Moreover, ICAM-1 can associate with several actin binding cytoskeletal proteins (42, 43). To investigate the potential relationship between actin cytoskeleton

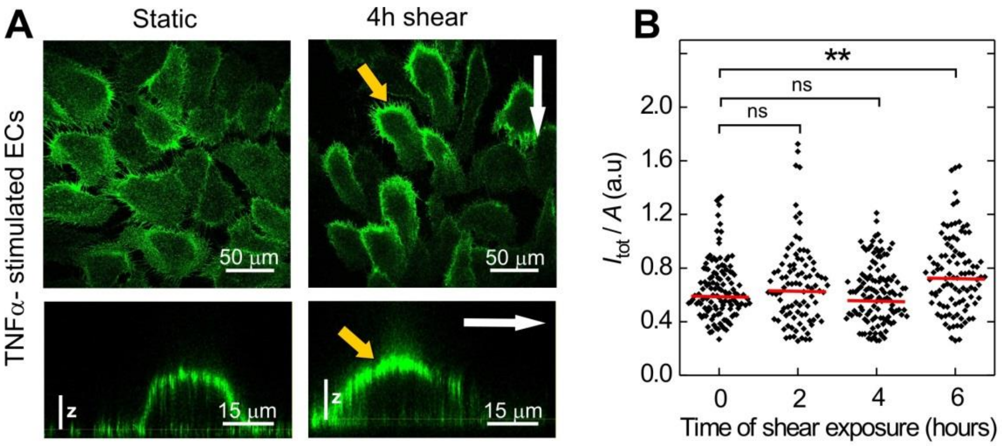

Figure 4.3 Effect of shear flow on TNF-α stimulated ECs. (A) Single plane confocal microscopy images taken at the basal cell membrane (*top rows*) and 3*D* orthogonal views *(bottom rows*) of ICAM-1 expressed on TNF-α stimulated ECs, in absence of shear flow (*left column*) and after 4h of continuous flow application (*right column*). White arrows indicate the direction of shear flow while yellow arrows point at the upstream accumulation of ICAM-1. **(B)** Fluorescence intensity of the ICAM-1 signal integrated over the entire cell and normalized to the cell area, for static conditions (0 h) and for different times of shear exposure (2, 4 and 6 h). Horizontal red lines indicate the mean values. In total, 100 to 180 ECs from two separate experiments were analyzed per condition.

reorganization and ICAM-1 upstream location induced by shear stress, we simultaneously visualized ICAM-1 and actin at different stimulation conditions by confocal microscopy. As expected, in static conditions and regardless of TNF-α treatment, ECs exhibit a characteristic polygonal morphology with numerous actin fibers arranged in a radial pattern or emerging from the cell edges, resulting from tensile forces to maintain cell spreading (**Figs. 4.5A-C,** *bottom rows*, *left columns*). Once subjected to shear stress for four hours, actin filaments bundled into thicker actin fibers and aligned along the flow direction, in agreement with previous reports (24). Yet, the formation of thick actin fibers occurred more prominently downstream of the flow direction (**Fig. 4.5A-C** *bottom rows*, *right columns*), while a finer actin mesh, difficult to resolve by diffraction-limited confocal microscopy, emerged upstream of the flow direction.

To better quantify the changes in ICAM-1 and actin distribution as a result of shear-force stimulation we calculated the fluorescence intensity on the 50% of the cell, located either up- or down-stream the direction of the flow, and divided by the total intensity calculated over the entire cell. While in static conditions ICAM-1 was homogenously distributed over the entire EC membrane (time=0h in **Fig. 4.5D**), shear-force application resulted in a steady increase of

ICAM-1 intensity upstream of flow. Indeed, after four hours of shear stimulation ~75% of the ICAM-1 signal was located upstream of flow (**Fig. 4.5D**, green closed symbols). A similar trend was also observed on resting ECs (i.e., without TNF-α stimulation) (**Fig. 4.5D**, green open symbols) indicating that ICAM-1 re-distribution was solely due to shear-force stimulation. In contrast, the overall actin intensity signal remained rather uniform as a function of shear-exposure (**Fig. 4.5D** *bottom*), despite the major changes observed in actin morphology, i.e., formation of actin fibers downstream of flow and a finer actin mesh upstream of flow (**Fig. 4.5A-C,** *bottom panels*).

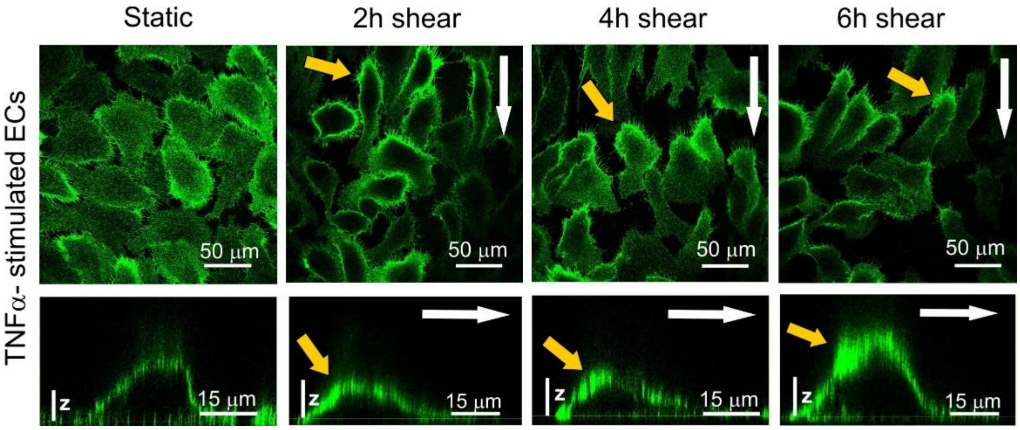

Figure 4.4 Effect of shear flow on the overall distribution of ICAM-1 on TNF-α-stimulated ECs over different exposure times. Single plane confocal microscopy images taken at the basal cell membrane (*top rows*) and 3*D* orthogonal views *(bottom rows*) of ICAM-1 on TNF-α-stimulated ECs in absence of flow (static) and upon different times of shear flow exposure (2h, 4h and 6h). White arrows indicate the direction of flow and yellow arrows point at the upstream accumulation of ICAM-1. The vertical scale *z* represents 3µm.

Shear flow induces ICAM-1 nanoclustering on TNF-α stimulated ECs. Having observed that shear flow promotes translocation of ICAM-1 upstream of flow, we next sought to investigate whether this global re-organization would also extend to the nanoscale by performing super resolution STED nanoscopy. Representative STED images of labeled ICAM-1 on TNF-α-stimulated ECs under static and after four hours of shear-flow application are shown in **Fig. 4.6A**. Individual fluorescent spots at different packing densities are resolved in all conditions, with more sparse fluorescent spots observed in the absence of shear-flow (left image) or in cell regions downstream of flow (most right image). On the other hand and consistent with the remarkable increase of ICAM-1 intensity upstream of flow, STED imaging

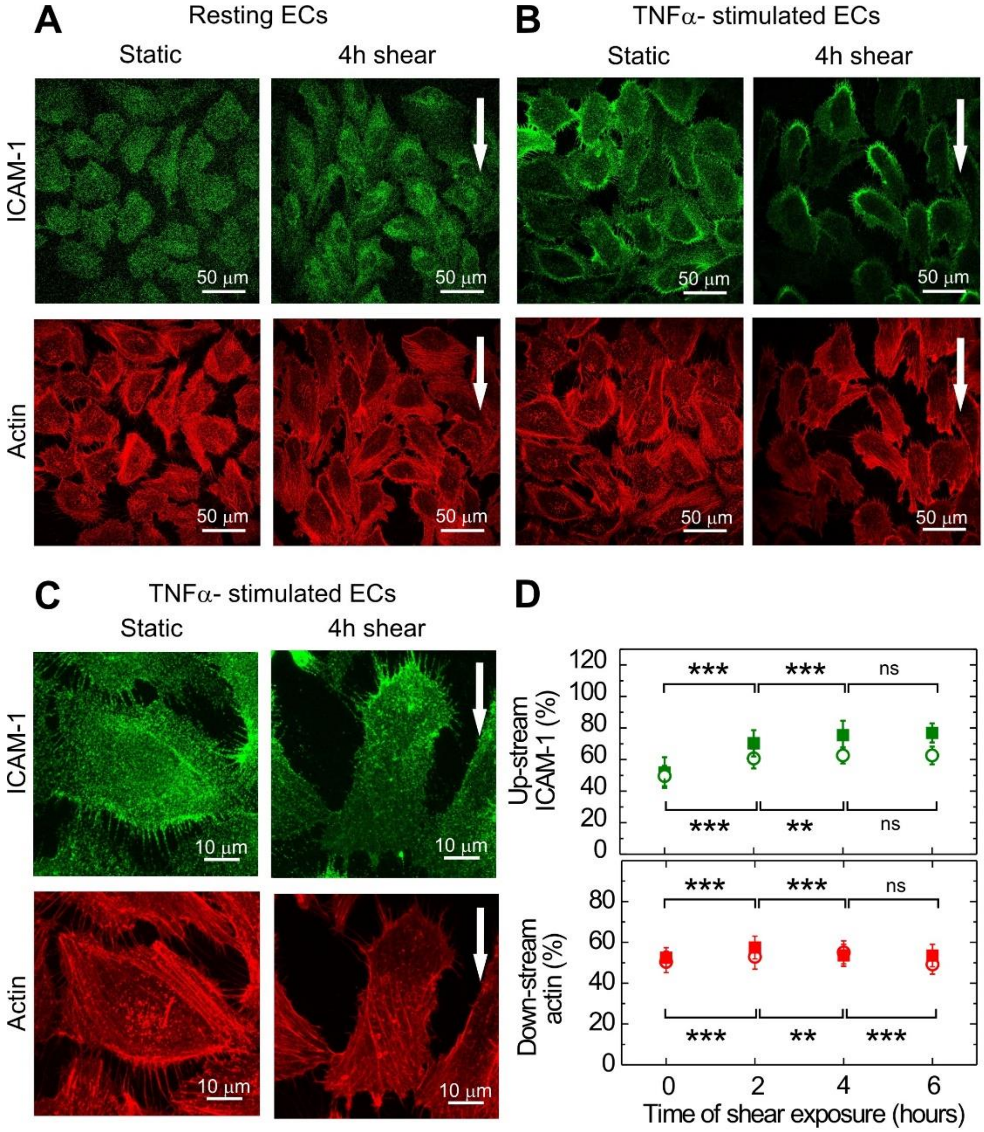

Figure 4.5 Effect of shear flow on the overall ICAM-1 and actin cytoskeleton reorganization. Single plane confocal microscopy images of ICAM-1 and actin cytoskeleton taken at the basal membrane of resting ECs **(A)** and TNF-α-stimulated **(B)** ECs in the absence of shear (static) and after 4 hours of continuous shear flow application at 8 dyn/cm^2. **(C)** Magnified confocal microscopy images of ICAM-1 and actin for the indicated conditions. Arrows indicate the direction of shear flow. **(D)** Percentage of ICAM-1 signal upstream of flow (*top graph*) and down-stream actin (*bottom graph*) taken from individual ECs under resting (open symbols) and TNF-α-stimulated (closed symbols) conditions. Time=0h corresponds to static conditions, i.e., no flow applied. For each cell, the total z-projected intensity of 80 frames over 8 µm distance is calculated. The intensity is normalized to the calculated area. In total, 100 to 180 ECs from two separate experiments were analyzed per condition.

on these regions showed a much higher packing density of spots (middle image). Spatially resolved individual spots were quantified over multiple cells in terms of their intensity (**Fig. 4.6B**) and local density (**Fig. 4.6C**) (See Methods). Under static conditions, the spots intensity showed on average a 2.7-fold increase in brightness compared to fluorescence spots localized outside the cell and corresponding to unspecific antibody binding (**Fig. 4.6B**). These results are entirely consistent with previous findings (44-46) confirming that on intact cells ICAM-1 expresses at least as a dimer.

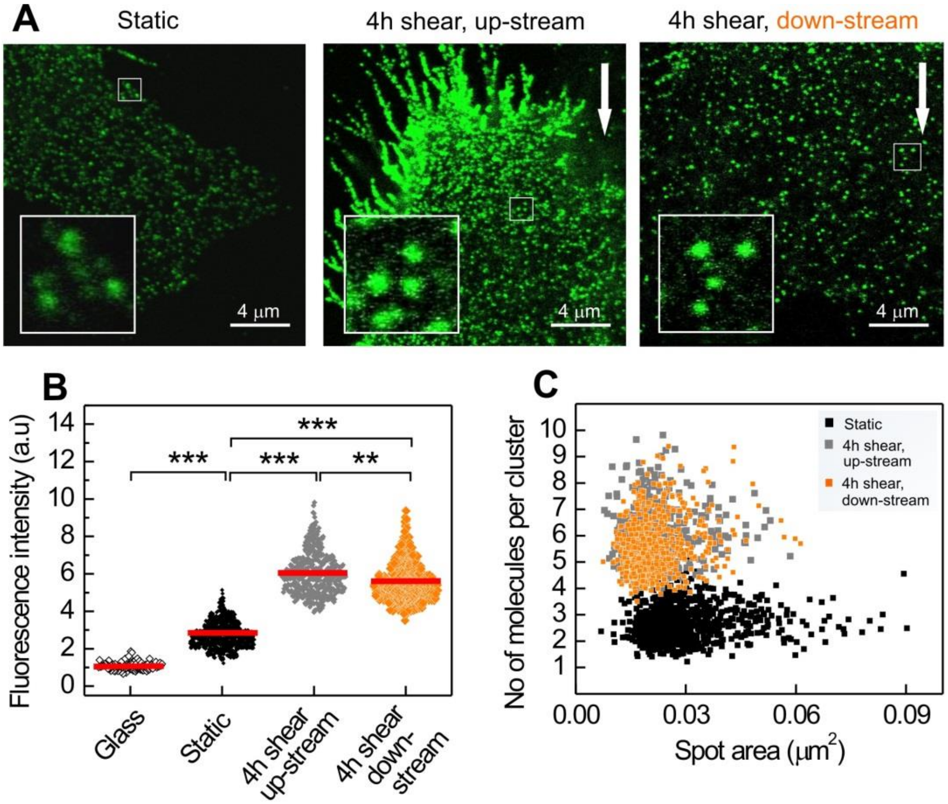

Figure 4.6 Effect of shear flow on ICAM-1 nanoclustering on TNF-α stimulated ECs. (A) Representative STED images of ICAM-1 at the basal membrane of ECs in static conditions and after 4 hours of shear flow exposure. (*Insets*) Magnified views of individual ICAM-1 fluorescent spots. Arrows indicate the direction of shear flow. The spatial resolution is ~100nm **(B)** Normalized intensity per spot and **(C)** density distribution (#molecules/spot area) of ICAM-1 under static and shear conditions, as extracted from the analysis of the STED images. Data from individual Abs non- specifically attached to the glass are represented in (B). Intensity of ICAM-1 spots under the different conditions has been normalized to the mean intensity obtained on glass. Horizontal red lines in (B) indicate the mean values. In total, 10-15 individual ECs from two separate experiments were analyzed per condition.

Remarkably, application of shear flow caused on average a further two-fold increase in spot brightness upstream of flow as compared to static conditions (**Fig. 4.6B**) demonstrating clustering of ICAM-1. Moreover the density of these nanoclusters became higher upon flow application as compared to static conditions (**Fig. 4.6C**). Interestingly, similar increase in nanoclustering and molecular density were also observed downstream of flow (**Fig. 4.6B**). Here however, ICAM-1 nanoclusters were much more sparsely distributed (**Fig. 4.6A**, *right*) and their intensity was slightly, but significantly, lower as compared to their ICAM-1 counterparts located upstream of flow (**Fig. 4.6B**). Overall, these results demonstrate that shear forces induce ICAM-1 spatial reorganization on the cell membrane of TNFα-stimulated ECs with the emergence of ICAM-1 nanoclustering.

Shear flow promotes the formation of actin patch-like structures upstream of flow that colocalize with ICAM-1. To bring some light into the molecular mechanisms leading to shear-flow induced ICAM-1 nanoclustering, we next visualized the co-distribution of ICAM-1 and actin on the apical membrane of TNF-α-treated ECs under static conditions and after four hours of shear-flow stimulation. Highly dense regions of actin patches enriched with ICAM-1 were observed by confocal microscopy upon shear-flow stimulation as compared to the more discrete puncta observed in static conditions (**Fig. 4.7A**). Indeed, image quantification showed more than a two-fold increase in the surface area occupied by these newly formed actin-like patches (**Fig. 4.7B**) and the amount of ICAM-1 significantly increased in these regions as compared to static conditions (**Fig. 4.7C**). These results indicate that in addition to the well-reported actin-fiber formation along shear flow direction (also shown in **Fig. 4.5C**), actin patch-like structures form at the rear end of cells upstream of flow, most probably retaining ICAM-1 molecules and increasing their location in these regions.

To gain more insight into the nanoscale re-arrangement of both actin and ICAM-1, we then turned to dual-color super-resolution STORM imaging. As this technique works best under TIRF-illumination, we restricted our imaging to regions closer to the basal membrane and particularly focused on the rear cell ends. In static conditions, actin forms a dense, uniformly distributed fine mesh together with stress fibers at the cell periphery and occasional actin puncta located at the middle of the cell (**Fig. 4.8A**, *left*), consistent with the confocal images taken at the basal cell membrane. Interestingly, application of shear flow led to the formation of many patch-like actin structures (**Fig. 4.8 A**, *right image* and *enlarged zooms* in **Fig. 4.8C, D**), similar to those observed on the apical membrane by confocal microscopy (**Fig. 4.7A**). These actin-patches are often interconnected by numerous thin actin strands (**Fig. 4.8B**, C). Concomitant to the reorganization of the actin cytoskeleton, we also observed that many ICAM-1 nanoclusters colocalized with these actin structures (**Fig. 4.8B, C**), although a robust quantification of the degree of colocalization between ICAM-1 and actin patches structures has proven to be very challenging.

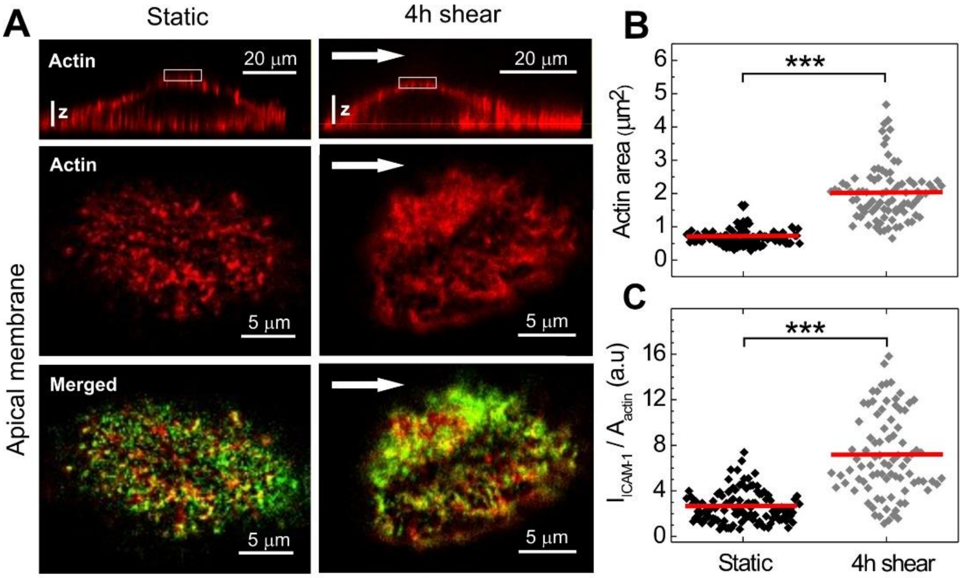

Figure 4.7 Formation of patch-like actin structures in ECs exposed to shear flow. (A) Ortogonal 3D view (*top row*) and single plane confocal images (*middle row*) at the apical membrane of the actin cytoskeleton in static conditions (*left column*) and after 4h of shear stimulation (*right column*). Merged confocal images of ICAM-1 (in green) and actin cytoskeleton (in red), in static conditions (*bottom left*) and after 4h of shear stimulation (*bottom right*). Arrows indicate the direction of shear flow. **(B)** Quantification of the area occupied by patch-like actin structures measured by manually outlining actin regions at the apical cell membrane. **(C)** Quantification of ICAM-1 fluorescent intensity normalized to corresponding actin area. In total 30 ECs from two separate experiments were analyzed per condition.

To further validate the strong relationship between shear-flow induced actin re-organization and ICAM-1 nanopatterning on TNF-α treated ECs, we used cytochalasin D (CytoD) to disturb the actin meshwork after shear stimulation and then imaged ICAM-1 distribution by means of STED nanoscopy. CytoD visibly perturbed the entire EC actin meshwork as evidenced by confocal imaging (**Fig. 4.9A**). While STED imaging showed no change in ICAM-1 organization after CytoD treatment in the absence of shear-flow stimulation, (**Fig. 4.9B, C**) dramatic changes in ICAM-1 nanoclustering occurred on the counterpart shear-flow stimulated cells. Indeed, perturbation of the actin cytoskeleton completely abrogated ICAM-1 nanoclustering (**Fig. 4.9B, C**) with fluorescence spots having intensities comparable to those of static conditions. Altogether, these results demonstrate that shear-forces induce massive actin-cytoskeleton reorganization on ECs and underscore the crucial role of the actin cytoskeleton in forming and maintaining ICAM-1 nanoclusters. Of note, CytoD treatment did not affect ICAM-1 dimer distribution on resting TNF-α treated ECs (**Fig. 4.9C**), a result that is fully consistent with the notion that ICAM-1 is constitutively expressed on the EC surface as a dimer (44-46).

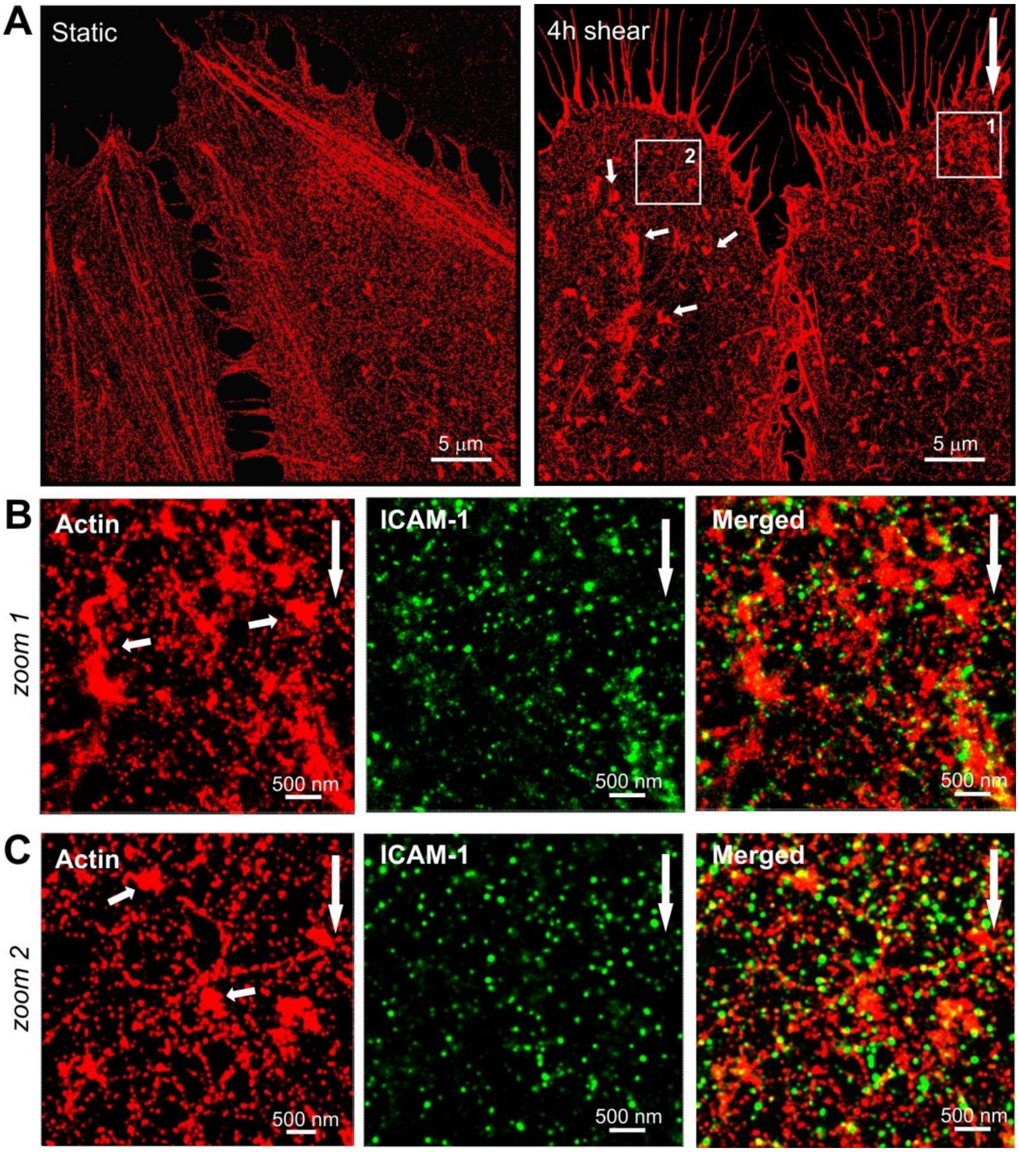

Figure 4.8 Organization of ICAM-1 nanoclusters within actin patch-like structures. (A) STORM images of the actin cytoskeleton at the basal EC membrane in static conditions and after 4 hours of shear flow exposure. Magnified view of the box 1 **(B)** and box 2 **(C)** of actin (*left*), the corresponding ICAM-1 (*middle*), and merged images (*right*). Large white arrows show the direction of applied shear flow and small white arrows in (A, *right*) point to actin patch-like structures.

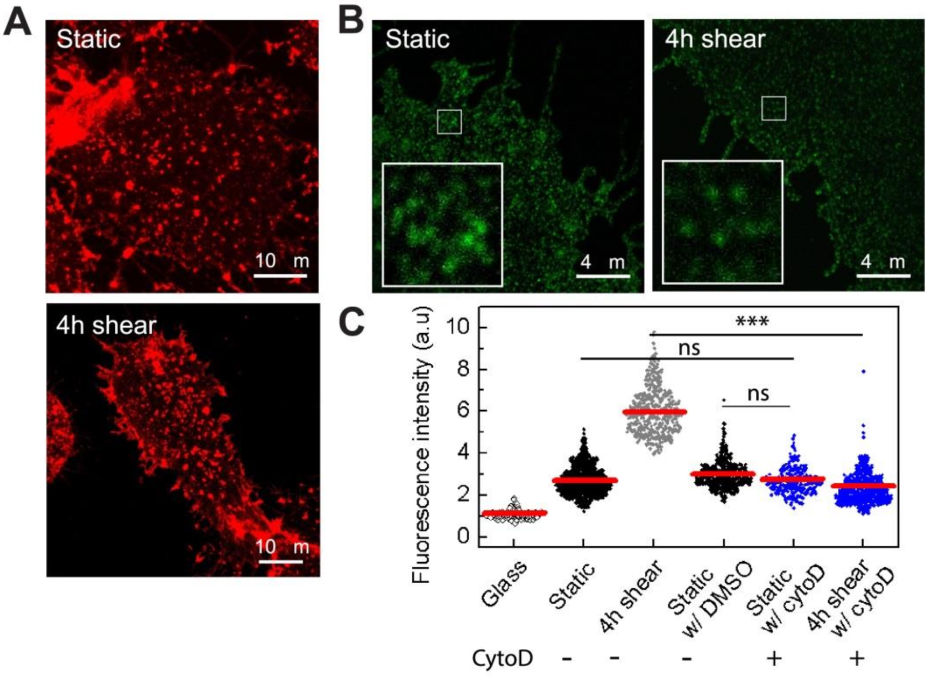

Figure 4.9 The effect of cytoD treatment on ICAM-1 and actin organization in TNF-α-stimulated ECs. (A) Confocal images of actin cytoskeleton after CytoD treatment on static (*top*) or 4h shear stimulated ECs (*bottom*). Images are z-projections of 80 confocal frames over 8 μm distance. **(B)** Representative STED images of ICAM-1 at the basal membrane of CytoD treated ECs for static (*left*) and after 4h of shear exposure (*right*). (*Insets*) Magnified views of ICAM-1. Arrows in A and B indicate the direction of shear flow. **(C)** Normalized intensity per spot of ICAM-1 on ECs no treated (-) and treated with CytoD (+) for the indicated experimental conditions. Signal from the glass represents the individual Abs non-specifically attached to substrate. Horizontal red lines indicate the mean values. In total, 10-15 ECs from one (upon CytoD treatment) or two separate (no cytoD traetement) experiments were analyzed per condition.

Changes in ICAM-1 organization correlate with changes in leukocyte migration across ECs. Upon inflammation, leukocytes migrate across the endothelium prior to extravasation in a process that is primarily mediated by interactions between ICAM-1 on the endothelium and its counterpart integrin receptor αLβ2 on the leukocyte membrane (7, 8). To study the potential relevance of shear-flow induced ICAM-1 nanopatterning on leukocyte behavior, we flowed non-activated Jurkat T cells on shear-flow stimulated, TNF-α-treated ECs and followed over time T-cell movement in the absence and presence of post-flow (**Fig. 4.10A**). Since it is well recognized that resting T-cells cannot be captured directly from the flow stream (47), we allowed these cells to settle on ECs for three minutes in absence of post-flow.

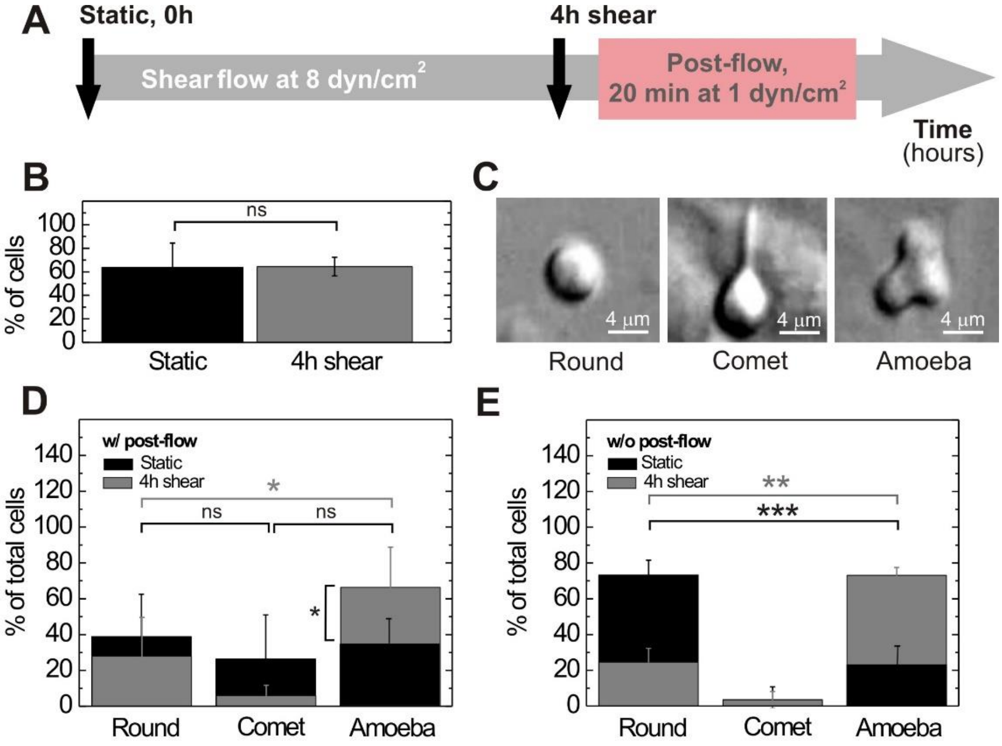

Figure 4.10 Effect of shear flow stimulation on the pro-migratory response of T-cells interacting with TNF-α-stimulated ECs. (A) Characteristic time scales of the experiments. ECs were initially subjected to continuous shear flow of 8 dyn/cm^2 for 4 h and then T-cells were flown onto ECs at 0.3 dyn/cm^2. The flow was stopped for 3 min allowing accumulation of T-cells on ECs. A post-flow of 1 dyn/cm^2 was then applied and kept constant for 20 minutes. Phase contrast images were taken prior to shear stimulation, i.e., static and before and after post-flow application, and the number of adherent Jurkat cells in the field of view was counted in each case. **(B)** Percentage of Jurkat T-cells that remained adhered after 20 min of post-flow on static or sheared ECs. **(C)** DIC images showing three characteristic cell morphologies: "round", "comet-like" and "amoeba-like". **(D)** Percentage of Jurkat T-cells with the indicated morphology developed during 20 minutes of post flow across ECs. **(E)** Corresponding morphology of Jurkat T-cells adhered to ECs in the absence of post-flow. *Black bars* represent static conditions and *grey bars* correspond to 4 hours of shear exposure. In total, 120 ECs from 10 separate experiments were analyzed under static conditions, while 60 ECs from 5 separate experiments were analyzed in presence of shear flow.

We then resumed the flow at 1dyn/cm^2 (post-flow), which is similar to the physiological levels of shear stress in post-capillary venues where leukocyte diapedesis takes place (48), and recorded cell movement for 20 minutes. We counted the number of cells prior to and after 20 minutes of post-flow application. Once subjected to post-flow, 64% of T-cells remained firmly adhered to ECs (**Fig. 4.10B**). These results were independent on whether ECs had been initially stimulated by prolonged shear-flow or not, suggesting that the elevated expression levels of

ICAM-1 on TNF-α-treated ECs are sufficient to support cell adhesion. Jurkat cells that withstood post-flow application stably adhered and migrated over the ECs surface. During this movement T-cells underwent noticeable morphological changes. We mainly observed three different morphologies, which we classified as "round", "comet-like" and "amoeba-like" (**Fig. 4.10C**). Whereas T-cells moving on static ECs showed no preference for any particular type of morphology (**Fig. 4.10D**, *black bars*), a majority of cells (ca. 66%) moving across shear-flow stimulated ECs showed amoeba-like morphology, consistent with a more pro-migratory phenotype (**Fig. 4.10D**, *grey bars*). Interestingly, this type of morphology dominated even in the absence of post-flow, as long as ECs had been previously subjected to shear-flow (**Fig. 4.10E**, *grey bars*), indicating that a mechanically pre-conditioned endothelium promotes the pro-migratory response of T-cells. In this case, however, cells do not show directional migration as post flow is missing, but instead move randomly over very short distances. On the other hand, the large majority (ca. 73%) of T cells adhered to ECs in the absence of post-flow and without previous shear-flow stimulation stay round (**Fig. 4.10E**, *black bars*) and move randomly. Thus, pre-stimulation of ECs with shear flow plays an important role in promoting T-cell pro-migratory response most probably due to the formation of functional adhesions sites. In addition, the presence of post-flow assures directional and long distance T-cell migration, possibly by facilitating changes in integrin conformational states (3, 32, 49, 50) that further strengthen ligand-integrin bonds.

To further investigate leukocyte migration across ECs we applied a tracking algorithm that allows us to reconstruct trajectories of individual T-cells (see details in Chapter 3) as they move in the presence of post-flow (**Fig. 4.11A**). Additionally, we used the PLANT algorithm described in Chapter 3 to detect changes in the velocity and time of interaction of T-cells with ECs (**Fig. 4.11B**). Time-trace curves of the cell motion in the direction parallel and perpendicular to the flow were separately analyzed and their respective velocities v_y and v_x were calculated. The total velocity was then determined as $V = \sqrt{v_x^2 + v_y^2}$. We defined regions of the trajectory with positive slope as positive velocities and regions with negative slopes as negative velocities. The total velocity was considered positive (V_+) when the cells were moving *along* the direction of the flow ($v_y > 0$), and negative (V_-) when the cell were moving *against* the direction of the flow ($v_y < 0$). Likewise, we defined (t_+) and (t_-) as the time periods during which the cell is interacting with ECs once moving *along* or *against* the direction of flow, respectively. Using the cumulative distribution function (CDF) we then quantified the mean values of V_+, V_-, t_+ and t_- for T-cells moving over shear flow pre-conditioned ECs or not (static conditions). On average, T-cells migrating across shear-flow stimulated ECs move faster compared to their counterparts moving across static ECs (**Fig. 4.11C**).

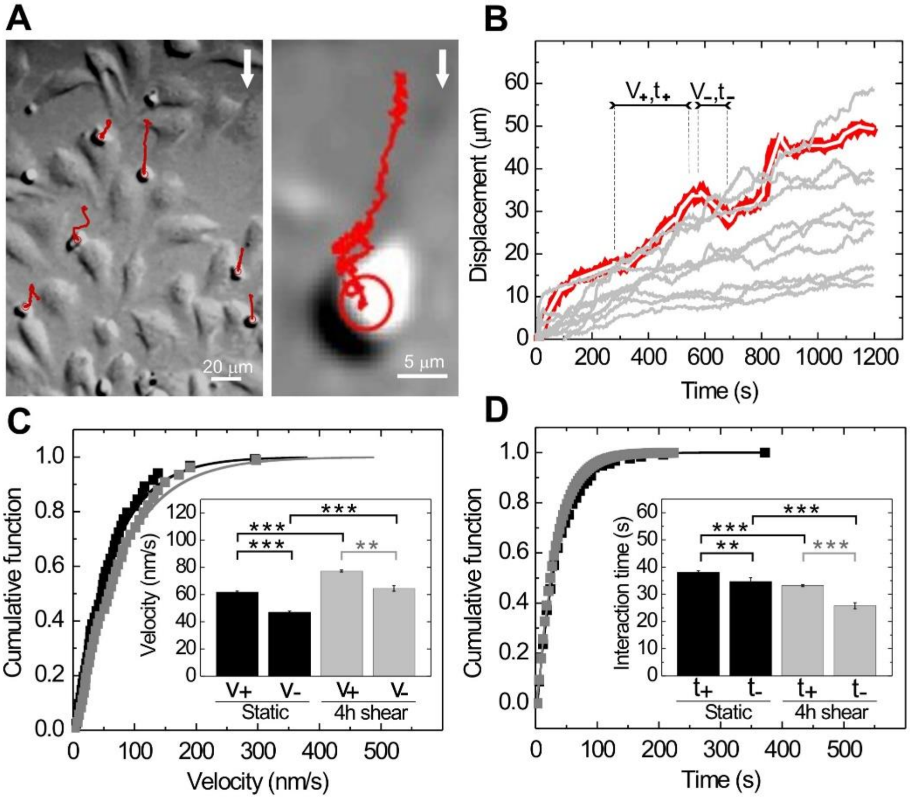

Figure 4.11 Effect of shear flow pre-stimulation on the T-cell migration across TNF-α-stimulated ECs. (A) Representative DIC image (*left*) of T-cells (smaller round cells) while moving on 4h pre-stimulated ECs (large elongated cells) with marked superimposed trajectories (*red lines*). Zoom-in of a T-cell with trajectory superimposed (*right*). White arrows indicate the direction of shear flow. **(B)** Characteristic time-trace plots (gray curves) of the of T-cell displacements in the direction parallel to the flow. The segmentation algorithm divides the curves in small straight traces (*red lines*) from which positive and negative slopes can be determined separately. **(C)** CDF of the positive velocities of T-cells moving on static ECs (black squares) and ECs sheared for 4 h (grey squares), fitted with single exponential functions (black and grey lines). **(D)** CDF of the interaction times of T-cells moving along the direction of the flow, on static ECs (black square) and ECs sheared for 4h (grey squares) fitted as in **(C).** Inset in (C) and (D) show the mean values of V_+, V_-, t_+, and t_- for the indicated conditions, obtained from the fittings. Data are expressed as mean ± SEM. In total 119 cell trajectories (approximately 60 per condition) collected from 6 independent experiments were analyzed.

Indeed, by fitting the experimental data to a single exponential function we estimated an average velocity for cell movement *along* the direction of flow to be V_+= (77.3 ± 0.7) nm/s and V_+= (61.9 ± 0.7) nm/s for shear-flow stimulated and static ECs respectively (**Fig. 4.11C**, *inset*). Interestingly, the mean interaction time between T-cells and ECs exhibited an opposite trend with respect to the velocity, being shorter in the case of shear-flow stimulated ECs, i.e., t_+= (33.2 ± 0.4) s and t_+= (38.1 ± 0.5) s for static ECs (**Fig. 4.11D**, *inset*). Moreover, when T-cells migrated against the direction of the flow, their velocity was reduced, i.e., $V_+>V_-$, regardless of whether the ECs were pre-exposed to shear flow or not (**Fig. 4.11C**, *inset*). In addition, the interaction times between T-cells and ECs were shorter for T-cells moving against the flow as compared to those ones moving along the flow ($t_+>t_-$), independently of the pre-stimulating conditions of ECs (**Fig. 4.11D**, *inset*). Altogether, these results indicate that while the directional motion of T-cells on ECs is driven by the post flow, the migration properties of T-cells depend on the pre-conditioning of ECs by shear stress.

4.3 Discussion

In this work we have used confocal and superresolution microscopy together with a PPFC device to study the effect of shear flow on the lateral organization of ICAM-1 on ECs, and its possible impact on leukocyte migration. Our data demonstrate that shear flow induces a massive reorganization of ICAM-1 on the EC membrane that directly correlates with specific changes in the migration behaviour of T-cells. Exposure of TNF-α-stimulated ECs to shear flow promoted translocation of the majority of ICAM-1 to the upstream direction of flow. Importantly, this global ICAM-1 redistribution was accompanied by the formation of local nanoclusters of the ligand over the entire EC membrane. Although it is well known that ICAM-1 organizes in microclusters upon engagement of integrins from the T-cell side (11-16), the nanoscale organization of ICAM-1 prior to T-cell engagement has not been reported yet (to the best of our knowledge). Here we show for the first time that mechanical stimulation driven by shear flow is sufficient to induce the formation of ICAM-1 nanoclusters and their global redistribution on the activated EC membrane, without requiring the presence of leukocyte interactions

Recent, *in-vitro* experiments have shown that remodelling of the actomyosin network can drive clustering of proteins on the lipid bilayer (51). Our experiments provide some evidence to support this idea as we observed that ICAM-1 organizes into dense nanoscale patterns that colocalize with actin cytoskeleton rich patchy regions. Moreover, perturbation of the actin cytoskeleton with CytoD highly impaired the nanocluster organization of ICAM-1 molecules on ECs pre-stimulated with shear flow. Thus, our data suggest that ICAM-1 reorganization might be driven by the actin cytoskeleton, which is in turn remodeled by the mechanical stress induced by the flow. This hypothesis is also in line with the known fact that ICAM-1 and actin cytoskeleton can interact by means of different adaptor proteins, such as α-actinin-4 and cortactin (43, 52, 53).

The migratory behavior of T-cells was also affected on ECs previously exposed to shear flow. Our data showed that a migratory phenotype is favoured in T-cells that adhere on mechanically stimulated ECs. In addition, using the algorithm described in Chapter 3 we found that T-cells move faster and interact for shorter periods of times on ECs pre-exposed to mechanical stress. As ICAM-1 is one of the main receptors implicated in the leukocyte-endothelium interaction we reasoned that these changes in the migratory behavior of T-cells are probably associated to the reorganization of the ICAM-1 molecules on the EC membrane brought about by the shear flow. Recently a theoretical motor- clutch model has been proposed in which the velocity of the cell at the front edge is regulated by the stiffness of the substrate and strength of the clutches (54, 55). Such model predicts that the increase of any of these two parameters leads to an increasing velocity of the cell front edge. The explanation for this is based on the fact that the advance of the T-cell is determined by the difference between the rate of actin polymerization, that pushes the cell membrane forward, and the velocity of the actin retrograde flow, which pulls the actin backward. The velocity of the cell is then increased due to the strengthening of the clutches that slow down the actin retrograde flow, thus increasing the effective velocity at the front edge. We can rationalize our results in the context of this motor-clutch model. Indeed, in our case, the clutches represent the bonds formed between ICAM-1 and its partner integrin on the T-cell side, αLβ2. Thus, the increase in the ICAM-1 nanoclustering induced by the shear flow strengthens the adhesion to αLβ2 integrins, reinforcing the clutch strength. According to the motor-clutch model, this effect will induce a faster advance of the T-cells on ECs, which agrees with our experimental observations.

On the other hand, according to the same model, stiffer substrates will induce the earlier break of the clutches, with a consequent reduction of the interaction times. In our experiments we have observed that ICAM-1 nanoclusters formed by shear stress colocalize with regions enriched with actin. Interaction between ICAM-1 and actin will most probably lead to ICAM-1 immobilization in the EC surface (56), effectively stiffening the regions of clutch anchoring. As the effective substrate for the clutches become stiffer, the bonds between fixed ICAM-1 and the actin cytoskeleton engaged integrins will break faster, reducing the time of interaction between T-cells and ECs as observed in our experiments. The model proposed to connect our overall results is summarized in **Fig. 4.12**. In summary, our results suggest a key role of mechanical forces in the organization of receptors on the EC membrane that further impacts the migratory behavior of leukocytes.

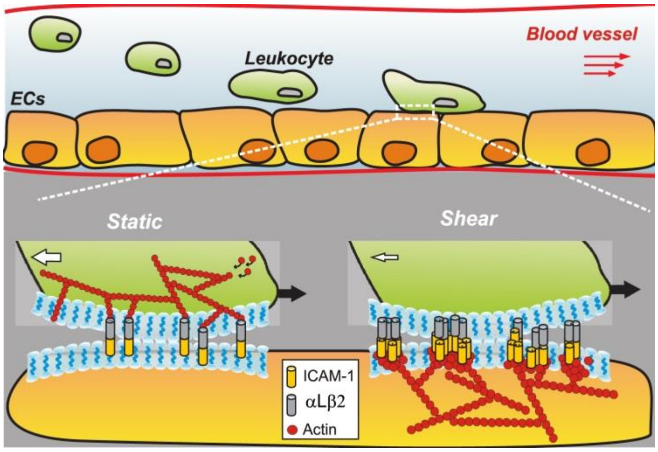

Fig. 4.12 Motor-clutch based model of leukocyte migration across ECs. Under shear-free conditions, leukocyte engagement leads to formation of bonds between individual ICAM-1 dimers and αLβ2. The strength of these bonds regulates leukocyte migration with the total velocity of the cell edge (black arrows) being determined by the difference between the speed of actin cytoskeleton polymerization and the speed of actin retrograde flow (white arrows). Shear flow pre-stimulation of ECs leads to local ICAM-1 nanoclustering and ICAM-1 nanopatterning within actin cytoskeleton rich patches which enhances the strength of ligand-integrin bonds by increasing avidity of ICAM-1 to αLβ2. This in turn reduces the retrograde flow rate of the actin cytoskeleton and thus increases the total velocity of the T-cell compared to the shear-free conditions. The size of white and black arrows indicates the resulting velocity power, with the thicker arrows corresponding to higher speed values.

4.4 Experimental procedures

Reagents, cytokines and antibodies. RPMI-1640 Dutch modification cell culture medium without phenol red and with glutamine (2mM) was purchased from Invitrogen. Medium was supplemented with 10% fetal bovine serum (FBS) and 1% actibiotic-antimycotic (AA). Mouse monoclonal primary antibody (anti-CD54, ICAM-1) was purchased from BD Pharmingen. Goat-anti-Mouse-AF488 secondary antibody was from Invitrogen. Phalloidin-TRITC, TNF-α and saponin were from Sigma and phalloidin-AF647 from Life Technologies. Goat-anti-mouse antibody conjugated to Cy3B was prepared in house.

Cell culture and sample preparation. Human endothelial cell lines (ECs) and Jurkat T lymphoblastoid (a T-cell model) were a gift from Alessandra Cambi (Nijmegen, The Netherlands). In a typical experiment ECs were plated on coverslips functionalized with fibronectin (20 μg/ml, Sigma-Aldrich, St Louis, MO) and grown to sub-confluence in RPMI-1640 medium (Lonza, Verviers, Belgium). To mimic inflammation conditions, samples were previously stimulated with TNF-α cytokine (10 ng/ml, Sigma-Aldrich, St Louis, MO) for 20 hours. Jurkat cells were adjusted to a concentration of $3\times10^{6}ml^{-1}$ prior to the experiments.

Shear flow experiments. The parallel-plate closed flow chamber (PPFC) described in Chapter 2 was used to apply shear stress on ECs. A 40 mm coverslip with a pre-formed endothelial sub-layer was assembled into the chamber and then mounted on the stage of an inverted microscope (Olympus IX71) equipped with 20×/0.5 NA air objective and a video camera (CMOS, Thorlabs). The flow chamber was connected on one end to an automated syringe pump (FCS2 Micro-Perfusion Pump) and on the other end to a medium reservoir. The microfluidic system was kept at 37ºC by means of a homemade box built around the microscope. 5% CO_2-enriched RPMI-1640 cell culture medium of 37ºC was perfused at constant shear flow of 8 dyn/cm^2 through the chamber. Shear stress (τ) of flowing medium was calculated using **Eq. 2.9**.

T-cell adhesion under flow. TNF-α-treated ECs were exposed to 4 hours of continuous shear flow of 8 dyn/cm^2, prior to T-cells adhesion. Next, Jurkat cells (3×10^6/ml) were flown on top of ECs at 0.3dyn/cm^2 for 3 minutes using RPMI-1640 perfusion medium. The flow was then stopped for 3 minutes to allow cells to accumulate. Next, a post-flow of 1 dyn/cm^2 was introduced and kept constant for 20 minutes. In static experiments Jurkat cells were flown on top of ECs that had not been subjected to shear flow. The entire period of T-cells perfusion was recorded by differential interference contrast microscopy (DIC) at 3 frame/s using 10×/0.25 NA air objective.

Immunofluorescence labeling. Following shear flow experiments, ECs were washed with warm PBS, fixed in ambient conditions with paraformaldehyde (PFA, 2%) for 15 minutes and immediately stained. Samples were incubated with blocking agents (3% bovine serum albumin, BSA; 10 mM glycine and 1% human serum, HS) for 30 minutes and washed. Next, cells were incubated with primary antibodies against ICAM-1 (5 µg/ml) for 30 minutes, washed and incubated further with the appropriate secondary antibody (2 µg/ml) for 30 minutes. In all cases, cells were stained simultaneously for F-actin with phalloidin-TRITC (0.25µg/ml) for 40 minutes, after initial permeabilization of the cell membrane with saponin (0.05%) for 10 minutes. Static ECs were double-stained for ICAM-1 and F-actin and used as a control. All individual labeling steps were carried out at room temperature. Samples for STORM imaging were immunostained as described above using phalloidin-AF647 for actin cytoskeleton labeling and antibody conjugated Cy3B for ICAM-1 staining, after initial membrane permeabilization with triton (0.002%) for 8 min.

Confocal microscopy. Fluorescence images of ECs were acquired using a laser-scanning confocal microscope (Eclipse TE2000, Nikon). Samples were excited at 488 nm and 561 nm to visualize ICAM-1 and F-actin, respectively. Crosstalk between detection channels was avoided by the use of appropriate excitation and emission bandpass filters. In addition, fluorescence images of ICAM-1 and F-actin were recorded separately by performing sequential scanning and merged afterwards. Three-dimensional image stacks were obtained by scanning through the z-direction in steps of 0.1 µm over a range of 20 µm with a piezo-driven 60×/1.49 NA oil immersion objective.

Stimulated emission depletion (STED) microscopy. Super-resolution images of ICAM-1 clusters were collected with a commercial CW-STED SP-5 microscope (see Chapter 2 for details). Images (1024×1024 pixels) were acquired with 12-bit pixel depth, recorded at speed of 8 kHz and averaged over 8 frames with line accumulation set at 8.

Dual colour stochastic optical reconstruction microscopy (STORM). Super-resolution images of actin cytoskeleton and ICAM-1 were acquired with a custom-made STORM microscope setup using a standard imaging buffer with PBS, 1M Cysteamine MEA, 50% Glucose in water and an oxygen scavenger system (14 mg of glucose oxidase + 50 ul of catalase in 200 ul PBS mixed well and centrifuged for 1 min) at a volume ratio of 80:10:10:1 respectively. Samples were excited with lasers at 647 nm (actin) and 560 nm (ICAM-1) and reactivation of dyes was done with a laser beam at 405 nm. The emitted light was collected with 100×/1.49N.A oil immersion objective, filtered by a quad band filter set (TRF89902-ET-405/488/561/647 Laser Quad Band Set for TIRF applications, Chroma) and imaged with an electron-multiplying CCD camera at an exposure time of 20 ms per frame. Images were analyzed using custom-written software (Insight3; provided by Bo Huang, University of California, San Francisco, CA).

Quantification of ICAM-1 and actin fluorescent intensity from confocal images. The total fluorescence intensity of ICAM-1 molecules and actin cytoskeleton were individually calculated as an integrated density signal extracted from individual ECs using ImageJ program. Z-projected intensity of 80 frames over 8 um distance, normalized to the cell surface area, are reported. The percentage of ICAM-1 and actin signal up- or downstream the flow was calculated as the intensity on half the cell up- or downstream the flow divided by the total intensity calculated over the entire cell.

Colocalization of ICAM-1 and actin signal was determined by the manual outlining of the patch-like actin structures and the subsequent quantification of ICAM-1 fluorescence intensity within these regions. The ICAM-1 fluorescent signal is normalized to the actin area.

Quantification of orientation angle of ECs. A straight line along the major axis of individual ECs was drawn manually, and the angle formed with respect to the direction of the flow was calculated using ImageJ. The distribution of angles was represented using a polar histogram.

Quantification of ICAM-1 cluster size from STED images. Unprocessed, superresolution STED images were analyzed by Gaussian fitting of individual nanoclusters as described in Chapter 2.

Generation of T-cells trajectories. The centroid position of T-cells was tracked using the algorithm described in Chapter 3. In total 119 cell trajectories (approximately 60 per condition) collected from 6 independent experiments were analysed. Only the regions in which the T-cells were interacting with the ECs were taken into account. Based on changes in cell shape during the entire tracking period Jurkat cells were classified as “round” (phase bright and circular morphology), “comet-like” (phase bright and circular morphology but with visible protrusion at the back of the migrating cell) and “amoeba-like” (phase bright and spread morphology in various orientations).

Analysis of T-cell migration on ECs. The PLANT algorithm (see Chapter 3 for details) was used to determine the changes in velocity and time of interaction from the individual time-trace curves of the X and Y coordinates of T-cell centroids; with X defined as the direction perpendicular to the shear flow and Y, the direction parallel to the flow. The total velocity was calculated as $V = \sqrt{v_x^2 + v_y^2}$. We then separated the total velocities in positives (V_+) and negatives (V_-) depending on whether the cell was moving *along* or *against* the flow respectively. Following the same criterion the interaction times were also divided in positives (t_+) and negatives (t_-). The distribution of positive and negative velocities and their corresponding times were each represented as a cumulative distribution function (CDF). The mean values of V_+, V_-, t_+ and t_- were retrieved by fitting the CDFs with single exponential functions.

Statistical analysis. Data are expressed as mean ± standard deviation (SD). Where indicated, the standard error of the mean (SEM) is reported. The statistical differences between the different experimental conditions were analysed using GraphPad Prism 6. The unpaired two-tailed Student test was used to determine the statistical differences between two data sets (Fig. 4.10B and 4.11C, D). When the mean of 3 or more data sets were compared, the statistical differences were evaluated using the One-way ANOVA, followed by the Tukey’s multiple comparison tests (Fig. 4.5B and 4.10D, E). In the case of non-Gaussian distributed data sets (Fig. 4.1B; 4.3B; 4.7B, C; 4.9C), the Kruskal-Wallis test, followed by Dunn’s multiple comparison test was conducted. Significance is represented using: *ns (*P>0.05); * (P<0.05); ** (P<0.001) and *** (P<0.0001).

4.5 References

1. Kansas, G.S., Selectins and their ligands: current concepts and controversies. *Blood*, (1996) **88**, 3259.
2. Campbell, J.J., Hedrick, J., Zlotnik, A., Siani, M.A., Thompson, D.A., and Butcher, E.C., Chemokines and the Arrest of Lymphocytes Rolling Under Flow Conditions. *Science*, (1998) **279**, 381.
3. Schenkel, A.R., Mamdouh, Z., and Muller, W.A., Locomotion of monocytes on endothelium is a critical step during extravasation. *Nat. Immunol.*, (2004) **5**, 393-400.
4. Dejana, E., The transcellular railway: insights into leukocyte diapedesis. *Nat. Cell. Biol.*, (2006) **8**, 105-107.
5. Ley, K., Laudanna, C., Cybulsky, M.I., and Nourshargh, S., Getting to the site of inflammation: the leukocyte adhesion cascade updated. *Nat. Rev. Immunol.*, (2007) **7**, 678-689.
6. Albelda, S.M., Smith, C.W., and Ward, P.A., Adhesion molecules and inflammatory injury. *The FASEB Journal*, (1994) **8**, 504-512.
7. Makgoba, M.W., Sanders, M.E., Luce, G.E.G., Dustint, M.L., Springer, T.A., Clark, E.A., Mannoni, P., and Shaw, S., ICAM-1 a ligand for LFA-1-dependent adhesion of B, T and myeloid cells. *Nature*, (1988) **331**, 86-88.
8. Oppenheimer-Marks, N., Davis, L.S., Bogue, D.T., Ramberg, J., and Lipsky, P.E., Differential utilization of ICAM-1 and VCAM-1 during the adhesion and transendothelial migration of human T lymphocytes. *The Journal of Immunology*, (1991) **147**, 2913-2921.
9. Mulligan, M.S., Vaporciyan, A.A., Miyasaka, M., Tamatani, T., and Ward, P.A., Tumor necrosis factor alpha regulates in vivo intrapulmonary expression of ICAM-1. *Am. J. Pathol.*, (1993) **142**, 1739-1749.
10. Nakashima, Y., Raines, E.W., Plump, A.S., Breslow, J.L., and Ross, R., Upregulation of VCAM-1 and ICAM-1 at Atherosclerosis-Prone Sites on the Endothelium in the ApoE-Deficient Mouse. *Arterioscler. Thromb. Vasc. Biol.*, (1998) **18**, 842.
11. Barreiro, O., Yáñez-Mó, M., Serrador, J.M., Montoya, M.C., Vicente-Manzanares, M., Tejedor, R., Furthmayr, H., and Sánchez-Madrid, F., Dynamic interaction of VCAM-

1 and ICAM-1 with moesin and ezrin in a novel endothelial docking structure for adherent leukocytes. *J. Cell Biol.*, (2002) **157**, 1233.

12. Carman, C.V., Jun, C.-D., Salas, A., and Springer, T.A., Endothelial Cells Proactively Form Microvilli-Like Membrane Projections upon Intercellular Adhesion Molecule 1 Engagement of Leukocyte LFA-1. *J. Immunol.*, (2003) **171**, 6135-6144.
13. Carman, C.V. and Springer, T.A., A transmigratory cup in leukocyte diapedesis both through individual vascular endothelial cells and between them. *J. Cell Biol.*, (2004) **167**, 377.
14. Shaw, S.K., Ma, S., Kim, M.B., Rao, R.M., Hartman, C.U., Froio, R.M., Yang, L., Jones, T., Liu, Y., Nusrat, A., Parkos, C.A., and Luscinskas, F.W., Coordinated Redistribution of Leukocyte LFA-1 and Endothelial Cell ICAM-1 Accompany Neutrophil Transmigration. *J. Exp. Med.*, (2004) **200**, 1571.
15. Millan, J., Hewlett, L., Glyn, M., Toomre, D., Clark, P., and Ridley, A.J., Lymphocyte transcellular migration occurs through recruitment of endothelial ICAM-1 to caveola- and F-actin-rich domains. *Nat. Cell Biol.*, (2006) **8**, 113-123.
16. Yang, L., Kowalski, J.R., Yacono, P., Bajmoczi, M., Shaw, S.K., Froio, R.M., Golan, D.E., Thomas, S.M., and Luscinskas, F.W., Endothelial Cell Cortactin Coordinates Intercellular Adhesion Molecule-1 Clustering and Actin Cytoskeleton Remodeling during Polymorphonuclear Leukocyte Adhesion and Transmigration. *J. Immunol.*, (2006) **177**, 6440-6449.
17. van Buul, J.D., van Rijssel, J., van Alphen, F.P.J., Hoogenboezem, M., Tol, S., Hoeben, K.A., van Marle, J., Mul, E.P.J., and Hordijk, P.L., Inside-Out Regulation of ICAM-1 Dynamics in TNF-α-Activated Endothelium. *PLoS ONE*, (2010) **5**, e11336.
18. Tilghman, R.W. and Hoover, R.L., E-selectin and ICAM-1 are incorporated into detergent-insoluble membrane domains following clustering in endothelial cells. *FEBS Letters*, (2002) **525**, 83-87.
19. Barreiro, O., Yáñez-Mó, M., Sala-Valdés, M., Gutiérrez-López, M.D., Ovalle, S., Higginbottom, A., Monk, P.N., Cabañas, C., and Sánchez-Madrid, F., Endothelial tetraspanin microdomains regulate leukocyte firm adhesion during extravasation. *Blood*, (2005) **105**, 2852.
20. Tsuboi H., Ando J., Korenaga R., Takada Y., and Kamiya A., Flow Stimulates ICAM-1 Expression Time and Shear Stress Dependently in Cultured Human Endothelial Cells. *Biochem. Biophys. Res. Commun.*, (1995) **206**, 988-996.

21. Nagel T., Resnick N., Atkinson W.J., Dewey C.F., and Gimbrone M.A., Shear stress selectively upregulates intercellular adhesion molecule-1 expression in cultured human vascular endothelial cells. *J. Clin. Invest.*, (1994) **94**, 885-891.

22. Chien S., Li S., and Shyy J.Y.J., Effects of Mechanical Forces on Signal Transduction and Gene Expression in Endothelial Cells. *Hypertension*, (1998) **31**, 162.

23. Topper J.N. and Gimbrone Jr M.A., Blood flow and vascular gene expression: fluid shear stress as a modulator of endothelial phenotype. *Mol. Med. Today,* (1999) **5**, 40-46.

24. Wojciak-Stothard B. and Ridley A.J., Shear stress-induced endothelial cell polarization is mediated by Rho and Rac but not Cdc42 or PI 3-kinases. *J. Cell Biol.*, (2003) **161**, 429-439.

25. Davies P.F., Robotewskyj A., and Griem M.L., Quantitative studies of endothelial cell adhesion. Directional remodeling of focal adhesion sites in response to flow forces. *J. Clin. Invest.*, (1994) **93**, 2031-2038.

26. Yamamoto K. and Ando J., Endothelial cell and model membranes respond to shear stress by rapidly decreasing the order of their lipid phases. *J. Cell Sci.*, (2013) **126**, 1227.

27. Sheikh S., Rainger G.E., Gale Z., Rahman M., and Nash G.B., Exposure to fluid shear stress modulates the ability of endothelial cells to recruit neutrophils in response to tumor necrosis factor-α: a basis for local variations in vascular sensitivity to inflammation. *Blood*, (2003) **102**, 2828.

28. Butler P.J., Norwich G., Weinbaum S., and Chien S., Shear stress induces a time- and position-dependent increase in endothelial cell membrane fluidity. *Am. J. Physiol.-Cell Physiol.*, (2001) **280**, C962.

29. Dustin M.L. and Springer T.A., T-cell receptor cross-linking transiently stimulates adhesiveness through LFA-1. *Nature,* (1989) **341**, 619-624.

30. Constantin G., Majeed, M. Giagulli, C. Piccio, L., Kim, J.Y., Butcher E.C., and Laudanna C., Chemokines trigger immediate beta2 integrin affinity and mobility changes: differential regulation and roles in lymphocyte arrest under flow. *Immunity*, (2000) **13**, 759-69.

31. Shamri R., Grabovsky V., Gauguet J.-M., Feigelson S., Manevich E., Kolanus W., Robinson M.K., Staunton D.E., von Andrian U.H., and Alon R., Lymphocyte arrest requires instantaneous induction of an extended LFA-1 conformation mediated by endothelium-bound chemokines. *Nat. Immunol.*, (2005) **6**, 497-506.

32. Woolf E., Grigorova I., Sagiv A., Grabovsk V., Feigelson S.W., Shulman Z., Hartmann T., Sixt M., Cyster J.G., and Alon R., Lymph node chemokines promote sustained T lymphocyte motility without triggering stable integrin adhesiveness in the absence of shear forces. *Nat. Immunol.*, (2007) **8**, 1076-1085.

33. Astrof N.S., Salas A., Shimaoka M., Chen J., and Springer T.A., Importance of Force Linkage in Mechanochemistry of Adhesion Receptors. *Biochemistry*, (2006) **45**, 15020-15028.

34. Marschel P. and Schmid-Schönbein G.W., Control of Fluid Shear Response in Circulating Leukocytes by Integrins. *Ann. Biomed. Eng.*, (2002) **30**, 333-343.

35. Zwartz G.J., Chigaev A., Dwyer D.C., Foutz T.D., Edwards B.S., and Sklar L.A., Real-time Analysis of Very Late Antigen-4 Affinity Modulation by Shear. *J. Biol. Chem.*, (2004) **279**, 38277-38286.

36. Orr A.W., Ginsberg M.H., Shattil S.J., Deckmyn H., and Schwartz M.A., Matrix-specific Suppression of Integrin Activation in Shear Stress Signaling. *Mol. Biol. Cell*, (2006) **17**, 4686-4697.

37. Morigi M., Zoja C., Figliuzzi M., Foppolo M., Micheletti G., Bontempelli M., Saronni M., Remuzzi G., and Remuzzi A., Fluid shear stress modulates surface expression of adhesion molecules by endothelial cells. *Blood*, (1995) **85**, 1696.

38. Cinamon G., Shinder V., and Alon R., Shear forces promote lymphocyte migration across vascular endothelium bearing apical chemokines. *Nat. Immunol.*, (2001) **2**, 515-522.

39. Papaioannou T. G. and Stefanadis C., Vascular Wall Shear Stress: Basic Principles and Methods. *Hellenic. J. Cardiol.* , (2005) **46**, 9-15.

40. Haraldsen G., Kvale D., Lien B., Farstad I.N., and Brandtzaeg P., Cytokine-regulated expression of E-selectin, intercellular adhesion molecule-1 (ICAM-1), and vascular cell adhesion molecule-1 (VCAM-1) in human microvascular endothelial cells. *J. Immunol.*, (1996) **156**, 2558-2565.

41. Galbraith C.G., Skalak R., and Chien S., Shear stress induces spatial reorganization of the endothelial cell cytoskeleton. *Cell Motil. Cytoskel.*, (1998) **40**, 317-330.

42. Schaefer A., te Riet J., Ritz K., Hoogenboezem M., Anthony E.C., Mul F.P.J., de Vries C.J., Daemen M.J., Figdor C.G., van Buul J.D., and Hordijk P.L., Actin-binding proteins differentially regulate endothelial cell stiffness, ICAM-1 function and neutrophil transmigration. *J. Cell Sci.*, (2014).

43. Carpen O., Pallai P., Staunton D.E., and Springer T.A., Association of intercellular adhesion molecule-1 (ICAM-1) with actin-containing cytoskeleton and alpha-actinin. *J. Cell Biol.*, (1992) **118**, 1223-1234.

44. Jun C.D., Carman C.V., Redick S.D., Shimaoka M., Erickson H.P., and Springer T.A., Ultrastructure and function of dimeric, soluble intercellular adhesion molecule-1 (ICAM-1). *J. Biol. Chem.*, (2001) **276**, 29019-29027.

45. Bene L., Balázs M., Matkó J., Möst J., Dierich M.P., Szöllösi J., and Damjanovich S., Lateral organization of the ICAM-1 molecule at the surface of human lymphoblasts: a possible model for its co-distribution with the IL-2 receptor, class I and class II HLA molecules. *Eur. J. Immunol.*, (1994) **24**, 2115-23.

46. Miller J., Knorr R., Ferrone M., Houdei R., Carron C.P., and Dustin M.L., Intercellular adhesion molecule-1 dimerization and its consequences for adhesion mediated by lymphocyte function associated-1. *J. Exp. Med.*, (1995) **182**, 1231-1241.

47. Sigal A., Bleijs D.A., Grabovsky V., van Vliet S. J., Dwir O., Figdor C.G., van Kooyk Y., and Alon R., The LFA-1 integrin supports rolling adhesions on ICAM-1 under physiological shear flow in a permissive cellular environment. *J. Immunol.*, (2000) **165**, 442-452.

48. Schmid-Schönbein H., Clinical Aspects of Blood Viscosity and Cell Deformability, (1981) *Springer-Verlag*, Berling Heiderberg.

49. Dixit N., Yamayoshi I., Nazarian A., and Simon S.I., Migrational Guidance of Neutrophils Is Mechanotransduced via High-Affinity LFA-1 and Calcium Flux. *J. Immunol.*, (2011) **187**, 472-481.

50. Smith A., Bracke M., Leitinger B., Porter J.C., and Hogg N., LFA-1-induced T cell migration on ICAM-1 involves regulation of MLCK-mediated attachment and ROCK-dependent detachment. *J. Cell Sci.*, (2003) **116**, 3123.

51. Köster D. V., Husain K., Iljazi E., Bhat A., Bieling P., Mullins R. D., Rao M., and Mayor S., Actomyosin dynamics drive local membrane component organization in an in vitro active composite layer. *Proc. Natl. Acad. Sci. USA,* (2016) **113**, E1645-E1654.

52. Durieu-Trautmann O., Chaverot N., Cazaubon S., Strosberg A. D., and Couraud P. O. Intercellular adhesion molecule 1 activation induces tyrosine phosphorylation of the cytoskeleton-associated protein cortactin in brain microvessel endothelial cells. *J. Biol. Chem.*, (1994) **269**, 12536-12540.

53. Schaefer A., Riet J., Ritz K., Hoogenboezem M., Anthony E.C., Mul F.P.J., de Vries C.J., Daemen M.J, Figdor C.G., van Buul J.D., and Hordijk P.L., Actin-binding

proteins differentially regulate endothelial cell stiffness, ICAM-1 function and neutrophil transmigration, *J. Cell Sci.*, (2014) **127**, 4470–4482.

54. Bangasser B. L. and Odde D. J., Master equation-based analysis of a motor-clutch model for cell traction force. *Cell Mol. Bioeng.*, (2013) **6**, 449-459.
55. Bangasser B. L., Rosenfeld S. S., and Odde D. J., Determinants of Maximal Force Transmission in a Motor-Clutch Model of Cell Traction in a Compliant Microenvironment. *Biophys. J.*, (2013) **105**, 581-592.
56. Comrie W., Boyle S., Li S., and Burkhardt J., Regulated cytoskeletal control of ICAM-1 mobility on the dendritic cell plasma membrane enhances T cell activation (P1205). *J. Immunol.*, (2013) **190**, 188-6.

Chapter 5

Lateral Mobility and Nanoscale Spatial Arrangement of Chemokine-activated α4β1 Integrins on T Cells

As discussed in Chapter 1, α4β1 is one of the main integrins mediating the adhesion of leukocytes during their process of trafficking. Chemokines play an important role in the activation of integrins and thus in the adhesion of T lymphocytes. A central question regarding α4β1 function is how its lateral mobility and organization influence its affinity and avidity following cell stimulation with chemokines and/or ligands. In this Chapter we have combined single particle tracking and super-resolution imaging approaches to explore the lateral mobility and spatial arrangement of individual α4β1 integrins on T cells exposed to different activating stimuli. We show that CXCL12 stimulation leads to rapid and transient α4β1 activation, measured by induction of the activation epitope recognized by the HUTS-21 anti-β1 antibody and by increased talin-β1 association. CXCL12-dependent α4β1 activation directly correlated with restricted lateral diffusion and integrin immobilization. Moreover, co-stimulation by CXCL12 together with soluble VCAM-1 potentiated integrin immobilization with a five-fold increase in immobile integrins as compared to unstimulated conditions. Our data indicate that docking by talin of the chemokine-activated α4β1 to the actin cytoskeleton favors integrin immobilization, which likely facilitates ligand interaction and increased adhesiveness. Super-resolution imaging showed that the nanoscale organization of high-affinity α4β1 remains unaffected following chemokine and/or ligand addition. Instead, newly activated α4β1 integrins organize on the cell membrane as independent units without joining pre-established integrin sites to contribute to cluster formation. Altogether, our results provide a rationale to understand how the spatiotemporal organization of activated α4β1 integrins regulates T lymphocyte adhesion.

This work has been published as A. Sosa-Costa*, S. Isern de Val*, S. Sevilla-Molina, K. J. E. Borgman, C. Manzo, J. Teixidó, and M. F. Garcia-Parajo, "Lateral mobility and nanoscale spatial arrangement of chemokine-activated α4β1 integrins on T cells", *J. Biol. Chem.,*(2016) **29**, 21053-21062. *Equally contributing authors.

5.1 Introduction

As previously described in Chapter 1, integrins are heterodimeric cell membrane adhesion receptors composed of non-covalently-associated α and β subunits which mediate cell-cell and cell-extracellular matrix adhesion (1). Integrins control morphogenesis, immunity, tissue healing, and tumor growth and metastasis. In particular, the α4β1 (VLA-4) and αLβ2 (LFA-1) integrins are key players for T lymphocyte trafficking from blood circulation to lymphoid tissues and to sites of injury and infection (2, 3). Their adhesiveness is rapidly and transiently activated by chemokines (4-6), allowing highly dynamic T cell interactions with the endothelium that facilitates crawling and diapedesis. Binding of chemokines to their receptors generates an inside-out signaling that impinges on the cytoplasmic domains of β subunits (7-9), leading to the extension of high-affinity conformations of the extracellular α4β1 and αLβ2 integrins, that are competent for binding to their ligands VCAM-1 and ICAM-1, respectively. It is generally accepted that interactions of talin and kindlin with specific cytoplasmic motifs on β1 and β2 integrin subunits represent critical steps for the generation of active α4β1 and αLβ2 integrins (9-12).

The role played by α4β1 is especially important during T lymphocyte trafficking to sites of inflammation. Its interaction with VCAM-1, as well as with the CS-1 region of fibronectin, allows optimal T cell migration that contributes to subsequent immune responses. In addition to the critical involvement of talin in stimulating active α4β1 conformations (13, 14), the characterization of the inside-out signaling required for chemokine-promoted α4β1 activation revealed that Vav1 plays a key role for the optimal stimulation of T cell adhesion mediated by this integrin (15).

A central question regarding integrin function on lymphocytes is how the lateral organization and mobility of α4β1 and αLβ2 influence their activation and adhesiveness after the contact with chemokines and/or ligands. Addressing this question is important in order to improve our understanding on how these integrins spatially regulate their affinity and avidity, and would ultimately allow interference in this process. Earlier reports showed that lateral mobility controls αLβ2 rearrangement into clusters upon leukocyte activation, which occurs following release of cytoskeleton constraints, allowing integrin motion (16). These studies led to the proposal that inactive αLβ2 integrins are anchored to the cytoskeleton and released to strengthen ligand binding (16), suggesting that αLβ2 integrin activation precedes clustering. However, high-affinity integrins are more prone to interact with the cytoskeleton via their cytoplasmic domains

(1), causing integrin immobilization and compromising their lateral diffusion. Indeed, high-affinity αLβ2 appears immobile in PMA-activated cells (17). Along the same lines, it has been recently shown that αLβ2 activation by extracellular cations or chemokine stimulation increased the percentage of immobile αLβ2 nanoclusters in dendritic cells, indicating that αLβ2 immobilization correlates with integrin activation (18, 19).

Little is known about the mobility of α4β1 integrins on lymphocytes. On undifferentiated human bone marrow derived progenitor cells (BMPCs), the lateral diffusion of α4 integrins was found to be slow and correlated with strong BMPC adhesiveness (20). Furthermore, α4 tail deletion significantly decreased the membrane diffusivity of α4β1, in CHO cells (21). No studies have been yet undertaken focusing on the membrane lateral organization of α4β1 following lymphocyte exposure to chemokines and/or ligands.

In this Chapter we applied single-molecule approaches and super-resolution microscopy together with reporters of β1 activation to study the potential lateral mobility alterations and spatial regulation of α4β1 in response to chemokine and/or soluble ligand stimuli. Moreover, we investigated the effect of immobilized VCAM-1 on the lateral diffusion of α4β1. Our work reveals that a tight correlation between α4β1 immobilization, integrin activation and talin-β1 association are required for strengthening integrin adhesiveness.

5.2 Results

Chemokine stimulation transiently restricts the lateral mobility of α4β1 integrins on T cells. It is known that the chemokine CXCL12 triggers an inside-out signaling that induces high affinity conformations of α4β1, leading to strengthening of α4β1-VCAM-1 interaction and to increased leukocyte adhesiveness (15). On the other hand, it has been previously shown that in the case of αLβ2, different conformational states correlate with specific diffusion profiles on the cell membrane of monocytes and dendritic cells (18, 19). Thus, we first sought to investigate the effect of chemokine stimulation on the α4β1 lateral mobility on T cells. To this aim we used single particle tracking (SPT) approaches as described in Chapter 2. Molt-4 cells were employed as a model, as α4β1 constitutes the predominant β1 integrin heterodimer in these cells with very low α5β1 expression (**Fig. 5.1**), and it is highly responsive to CXCL12 stimulation (15). Cells were stretched onto PLL-coated coverslips and labeled at low density with the conformation-independent anti-β1 clone 18 antibody previously biotinylated and conjugated with streptavidin (SAV)-coated QD655. The motion of individual QDs was recorded by using a SPT set-up working under oblique illumination and subsequently, trajectories were reconstructed and analyzed. To minimize effects of internalization of the conjugated antibodies, measurements were always performed during the first 20 min after labeling. Moreover, to prevent potential artifacts due to the relative large size of QDs and the proximity between the cell membrane and the substrate, we exclusively imaged the apical side of the cells (**Fig. 5.2A**, left). Experiments were carried out as follows: during the first 10 min, measurements of α4β1 integrin diffusion were performed with T cells kept in RPMI 1640 medium, i.e., untreated condition. Then, CXCL12 was added and maintained for another 10 min. Measurements during this period were further separated into three time windows: 0-2 min, 2-5 min and 5-10min.

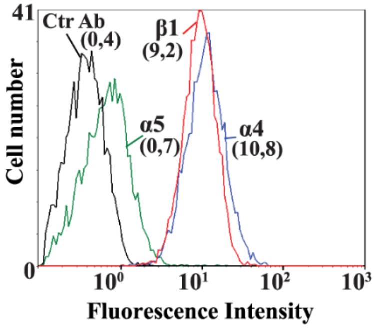

Figure 5.1 Expression of α4β1 and α5β1 on Molt-4 cells. Cells were analyzed by flow cytometry using control (black line), anti-α5 (green line), anti-α4 (blue line) or anti-β1 (red line) antibodies. Values denote mean fluorescence intensity measurements.

In general, the trajectories of individual α4β1 integrins under untreated conditions exhibited heterogeneous behavior, with some trajectories showing high mobility and others a more restricted motion (**Fig. 5.2A,** right). To quantitatively describe the diffusion of α4β1, mean square displacement (MSD) curves were generated per trajectory (examples shown in **Fig. 5.2B**). Different diffusion modes were detected: immobile, confined and Brownian motion (**Fig. 5.2A, B**). The diffusion coefficients at short time lags (D_{1-4}) were then determined by linear fitting of the MSD curves over the first four points, and their values were plotted as a semi-log histogram to show the full distribution of the α4β1 diffusive behavior.

On untreated cells, α4β1 integrins showed a broad variation over more than two orders of magnitude in the D_{1-4} values, with only a small fraction being immobile (~6%; **Fig. 5.2C**). The cut-off value to define the mobile population was calculated as previously explained in Chapter 2 ($D \leq 0.0025\ \mu m^2/s$ for these experimental conditions). On the other hand, the mean MSD curve of the total mobile population showed a linear relationship with time lag (**Fig. 5.2D**), indicating Brownian diffusion of the integrin on unperturbed cells, with a mean value of $D=(0.083 \pm 0.005) \mu m^2/s$.

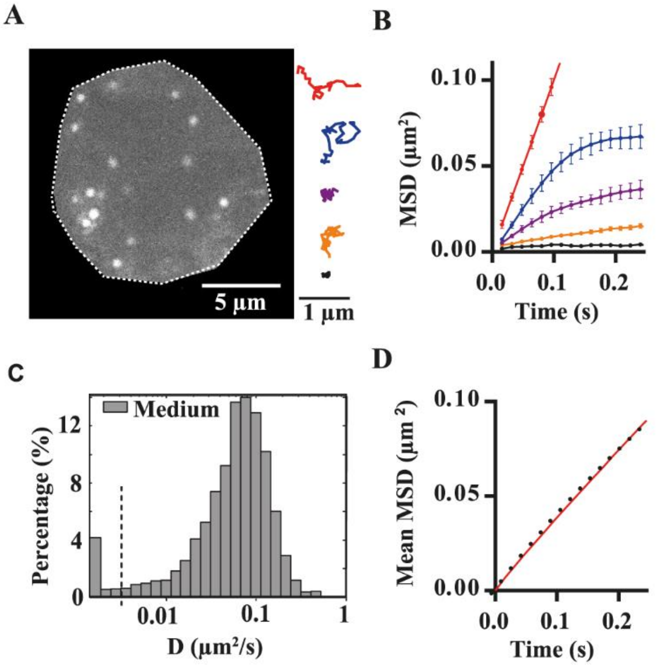

Figure 5.2 Characteri-zation of the lateral mobility of α4β1 on T cells (A) Representative frame from the tracking of individual α4β1 molecules on Molt-4 T cells using clone 18 anti-β1-QD-655 conjugates (an untreated cell is depicted). Examples of individual α4β1 trajectories displaying different types of motion are shown on the right. **(B)** MSD over time for representative trajectories displayed in A, using the same color code**. (C)** Semi-log histogram of D_{1-4} for α4β1. Values bel D_{1-4}=0.0025µm²/s (dash vertical line) correspond to immobile trajectories. **(D)** Overall MSD plot of the total mobile α4β1 population at different time lags. Statistics over 3 separate experiments: 4021 trajectories on 40 cells.

Addition of CXCL12 significantly altered α4β1 diffusion during the first two minutes after stimulation, with the appearance of a shoulder at lower D_{1-4} values and an increase of immobile trajectories, as compared to untreated samples (**Fig. 5.3A**). To better quantify these changes, we applied cumulative probability distribution (CPD) analysis on the mobile α4β1 population (22). By using this approach, two different α4β1 sub-populations having slow and fast diffusion were retrieved. For each sub-population we determined their relative occurrence (expressed in percentages), average diffusion coefficient D_i, and anomalous α_i exponents (where α indicates the type of motion, i.e., α=1 for Brownian diffusion and α<1 for anomalous diffusion) with the subscript *i*=*s*,*f* referring to the slow or the fast sub-population, respectively.

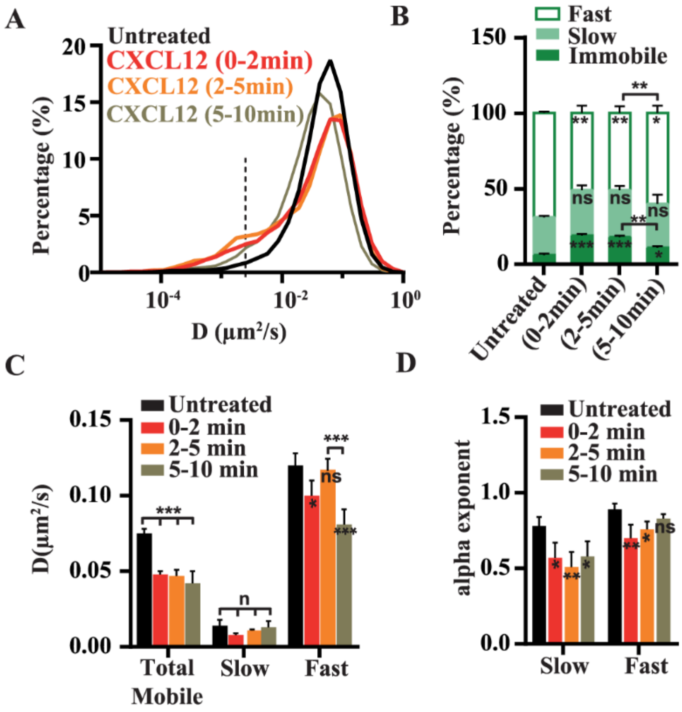

Figure 5.3 Effect of CXCL12 on the lateral mobility of α4β1 in T cells. **(A)** Overlay semi-log distributions of D_{1-4} for the indicated incubation conditions. The dash vertical line at D=0.0025µm^2/s denotes the threshold value for discriminating immobile (left) from mobile (right) trajectories. **(B)** Percentage of immobile, slow and fast α4β1 subpopulations for untreated or CXCL12-exposed cells. **(C)** Diffusion coefficient values of the total mobile population, and for the slow and fast α4β1 fractions. **(D)** Anomalous alpha exponents for the slow and fast α4β1 subpopulations under the indicated conditions. Unless indicated, statistical comparisons are done with respect to untreated cells. Statistics over 3 separate experiments: 20 untreated cells (1637 trajectories), 6 cells stimulated with CXCL12 for 0-2 min (816 trajectories), 9 cells stimulated with CXCL12 for 2-5 min (1014 trajectories) and 21 cells stimulated with CXCL12 for 5-10min (1937 trajectories).

A remarkable four-fold increase of immobile α4β1 trajectories (from 5% to 20%) was observed during the first two minutes of CXCL12 treatment as compared to untreated cells (**Fig. 5.3B**). This increase was mostly due to a reduction of the fast sub-population (from 70% to 50%; **Fig. 5.3B**). In addition, the D values for the total mobile and the fast sub-population were reduced with respect to unstimulated cells (**Fig. 5.3C**), together with a slight but significant increase in the anomalous diffusion of the fast sub-population (from α_f =0.89 to α_f =0.76; **Fig. 5.3D**). Moreover, while the percentage and diffusion coefficient of the slow mobile sub-population did not significantly change upon CXCL12 stimulation (**Fig. 5.3B, C**), its mobility became highly anomalous (from α_s=0.78 to α_s =0.57) (**Fig. 5.3D**). These major changes in α4β1 mobility were maintained during the subsequent 2-5 min of CXCL12 exposure (**Fig. 5.3A-D**).

During the 5-10 min time window after CXCL12 addition, the overall distribution of D_{1-4} remained shifted towards lower values with respect to untreated cells (**Fig. 5.3A**), with comparable values in terms of diffusion coefficients (**Fig. 5.3C**) and anomalous behavior (**Fig. 5.3D**) as those obtained during the first five minutes of CXCL12 stimulation. However, a partial recovery on the percentage of mobile molecules was observed in the 5-10 min period of CXCL12 treatment, concomitant with a decrease in the percentage of immobile α4β1 (around 11%) as compared to the first five minutes interval (**Fig. 5.3B**). Together, these results show that CXCL12 stimulation leads to both immobilization and slowing down of the overall lateral mobility of α4β1 integrins on the surface of T cells. Since CXCL12 promotes high-affinity α4β1, these results suggest the existence of a direct correlation between the integrin restricted diffusion and increased immobilization, and its activation. Moreover, the recovery in the mobile fraction in the 5-10 min period of exposure to CXCL12 is consistent with the reported transient effect of chemokines on integrin activation (19, 23-26).

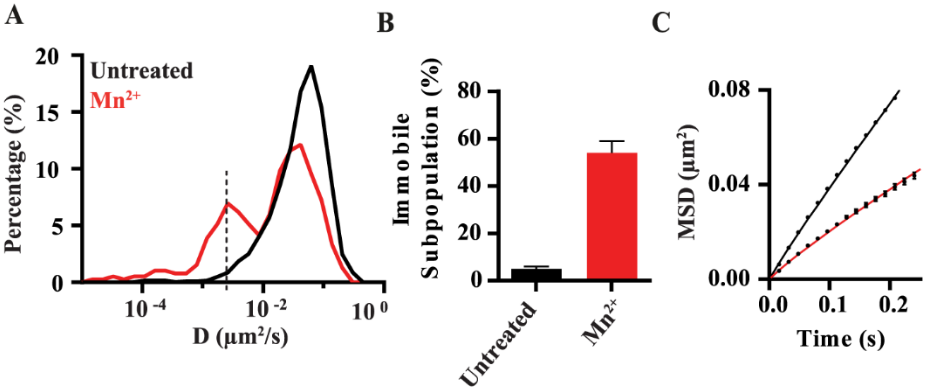

Figure 5.4 Effect of Mn^{2+} stimulation on the lateral mobility of α4β1 on T cells. (A) Overlay semi-log distributions of $D_{1\text{-}4}$ values for untreated Molt-4 cells (black line) or stimulated with Mn^{2+} for 10 min (red line). **(B)** Plot of the immobile trajectories for both conditions. **(C)** Mean MSD plot of mobile trajectories as a function of time for untreated (black line) and Mn^{2+}- treated cells (red line). 7 untreated cells (320 trajectories) and 8 cells stimulated with Mn^{2+} (223 trajectories) over 2 separate experiments.

α4β1 integrin immobilization correlates with integrin activation. To determine whether the level of integrin activation is indeed linked to α4β1 immobilization, we exposed Molt-4 cells to Mn^{2+}, a potent extracellular activator of integrin affinity (27). Activated α4β1 showed a high percentage of immobile integrins as compared to untreated cells (**Fig. 5.4A, B**), and nearly the same slower diffusion as obtained upon CXCL2 treatment, with mean D values of 0.040 ± 0.004 µm^2/s and D = 0.043 ± 0.009 µm^2/s for Mn^{2+} and CXCL2 treatment, respectively (**Fig. 5.4C**). These results thus confirm that immobilization and reduced mobility of α4β1 directly correlate with integrin activation.

Soluble VCAM-1 has a weak effect on the lateral diffusion of α4β1 integrins. Since ligands can activate integrins extracellularly (1, 28), we sought to investigate whether Molt-4 exposure to soluble VCAM-1-Fc would also influence the lateral mobility of α4β1. Surprisingly, no differences in the diffusivity of α4β1 molecules were observed after ligand addition (**Fig. 5.5A-D**). However, a nearly two-fold increase in the percentage of immobile trajectories, from 6% (untreated) to 11% upon VCAM-1 stimulation was observed during the first two minutes of VCAM-1 exposure (**Fig. 5.5B**), and this percentage remained constant up to 10 minutes (our observation time). Therefore, these data indicate that soluble VCAM-1-Fc is capable of inducing stable immobilization of a small sub-set of integrins, without altering the overall diffusion of the remaining mobile molecules.

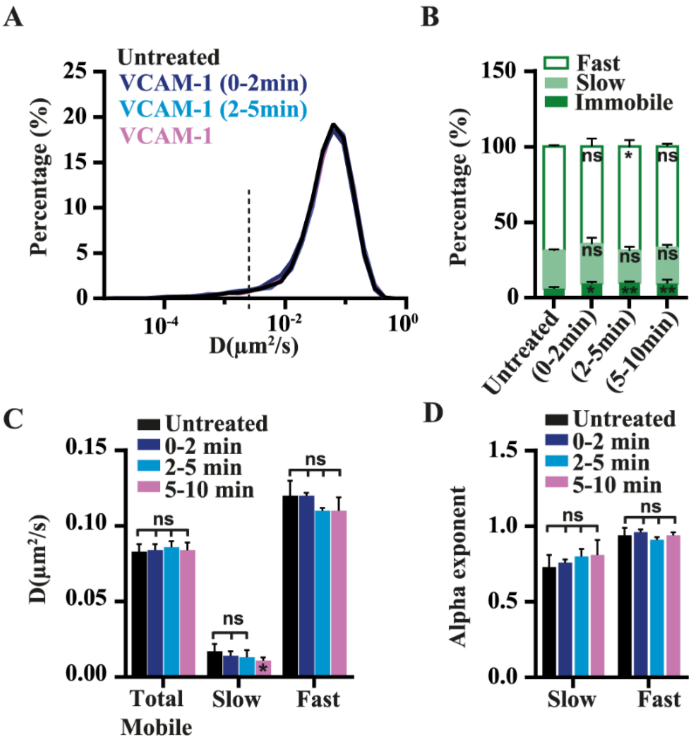

Figure 5.5 Effect of soluble VCAM-1 on the lateral mobility of α4β1 in T-cells. **(A)** Overlay semi-log distri-butions of D_{1-4} values for untreated cells or exposed to soluble VCAM-1-Fc in solution for 0-2, 2-5 and 5-10 min. **(B)** Percentage of immobile, slow and fast α4β1 sub-populations for un-treated or VCAM-1-exposed cells. **(C)** Diffusion coefficients of the total mobile population, and for the slow and fast fractions of α4β1. **(D)** Anomalous alpha exponents for the slow and fast α4β1 subpopulations. 10 untreated cells (1939 trajectories), 5 cells stimulated with VCAM-1 for 0-2min (787 trajectories), 8 cells stimulated with VCAM-1 for 2-5min (1582 trajectories) and 11 cells stimulated with VCAM-1 for 5-10min (1550 trajectories) over 3 separate experiments.

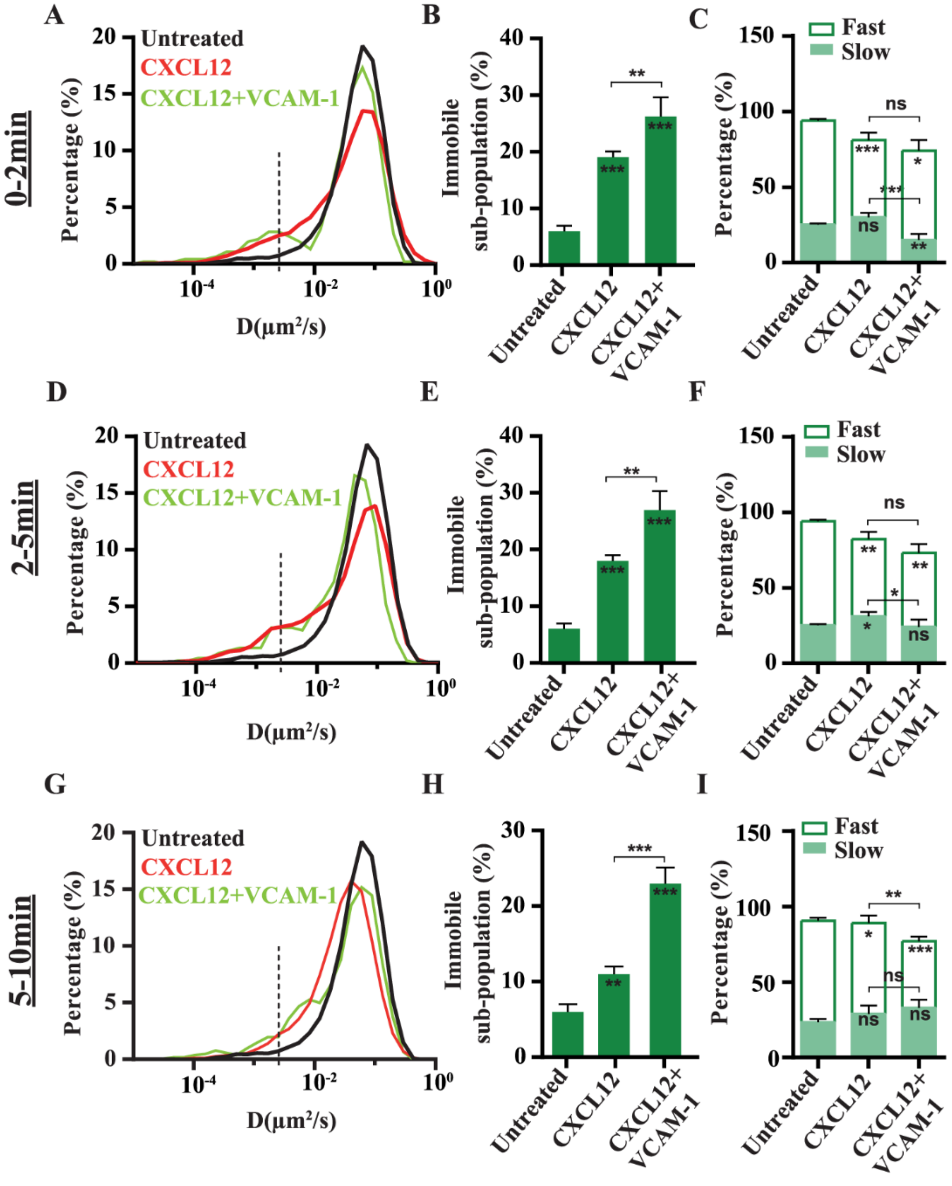

Figure 5. 6 Effect of CXCL12 and VCAM-1 co-stimulation on the lateral mobility of α4β1 in T-cells. (A-B) Data correspond to the first 0-2 min period of the different stimulating conditions. (A) Overlay semi-log distributions of D_{1-4} values for the indicated conditions. Data from the CXCL12 stimulation experiments (Fig. 1) are included to allow easier comparison of both conditions. (B) Percentage of immobile α4β1 subpopulation. (C) Percentage of slow and fast α4β1 subpopulations. (D-E) Same as (A-C) at the 2-5 min interval of stimulation. (G-I) Same as in (A-C) at the 5-10 min interval of stimulation. 29 untreated cells (2382 trajectories); 5 cells co-stimulated with CXCL12 and VCAM-1 (260 trajectories) during the 0-2 min, 7 cells co-stimulated with CXCL12 and VCAM-1 (301 trajectories) during the 2-5 min and 9 cells (587 trajectories) during 5-10 min, over 2 separate experiments.

Addition of soluble VCAM-1 to CXCL12 stimulation increases immobilization of α4β1 integrins. Given the strong relationship between CXCL12-induced α4β1 integrin activation and its restricted diffusion, we reasoned that the minor changes on α4β1 mobility observed after exposure to soluble VCAM-1 could indicate that the ligand alone is insufficient to fully activate the integrin. We thus enquired whether co-stimulation by both CXCL12 and soluble VCAM-1 could alter α4β1 diffusivity beyond that of VCAM-1 or CXCL12 alone. During the first 0-2 min treatment with CXCL12 and VCAM-1-Fc we detected a prominent shoulder at lower D_{1-4} values compared to unstimulated cells or those stimulated with VCAM-1-Fc or CXCL12 alone (**Fig. 5.6A**). Importantly, combined stimulation by CXCL12 and VCAM-1 resulted in a remarkable increase of α4β1 immobilization (~30% versus 6% for untreated cells and 20% for CXCL12 alone, **Fig. 5.6B**) that was maintained during the subsequent 2-5 min of combined stimulation (**Fig. 5.6D, E**). Notably, this increase in the percentage of immobile integrins was mostly due to a reduction of the slow sub-population (**Fig. 5.6C, F**), consistent with the hypothesis that the slow population corresponds to the intermediate conformational form of the integrins that become stabilized in the extended, activated form, upon CXCL12 co-stimulation with the ligand. A similar trend was observed during 5-10 min of co-stimulation with CXCL12 and VCAM-1-Fc (**Fig. 5.6G-I**), albeit more modest. That is, the percentage of immobile integrins in the presence of both stimuli was reduced from ~30% to 23% (**Fig. 5.6H**), as compared to cells co-stimulated for 0-5 min, suggesting that similar to CXCL12, the combined effect of CXCL12 and VCAM-1 is also transient. On the other hand, the diffusion of the slow and fast mobile α4β1 sub-populations did not significantly change during the first 2min of co-stimulation as compared to CXCL12 alone (**Fig. 5.7A**). Moreover, during the subsequent 2-5min of co-stimulation, the diffusion of the fast component decreased as compared to the case of CXCL12 stimulation alone (**Fig. 5.7B**), remaining constant during the last 5 min of co-stimulation (**Fig. 5.7C**). In addition, the type of mobility exhibited by the α4β1 upon co-stimulation was not significantly affected as compared to CXCL12 stimulation, between 2 and 10min of measurement (**Fig. 5.7B-F**). Note that during the first two minutes of co-stimulation the average diffusion coefficient of the total mobile trajectories does not appear to be affected by the stimuli. The reason for it is that the contribution of the slow population in this condition is very small (see **Fig. 5.6C**). Taken together, these results suggest that integrin binding to its soluble ligand alone does not lead to robust integrin immobilization and restricted diffusion, a condition best achieved upon simultaneous stimulation with CXCL12 and VCAM-1.

Immobilized VCAM-1 strongly arrests the mobility of α4β1 integrins, an effect that is potentiated by CXCL12 stimulation. It has been shown that multimeric and/or immobilized

ICAM-1 ligands increase the high-affinity form of αLβ2 integrins (29) and strongly affect their lateral mobility on the cell surface (19, 29). To investigate the effect of immobilized *vs.* soluble VCAM-1 on the diffusion profile of α4β1, we performed SPT experiments on Molt-4

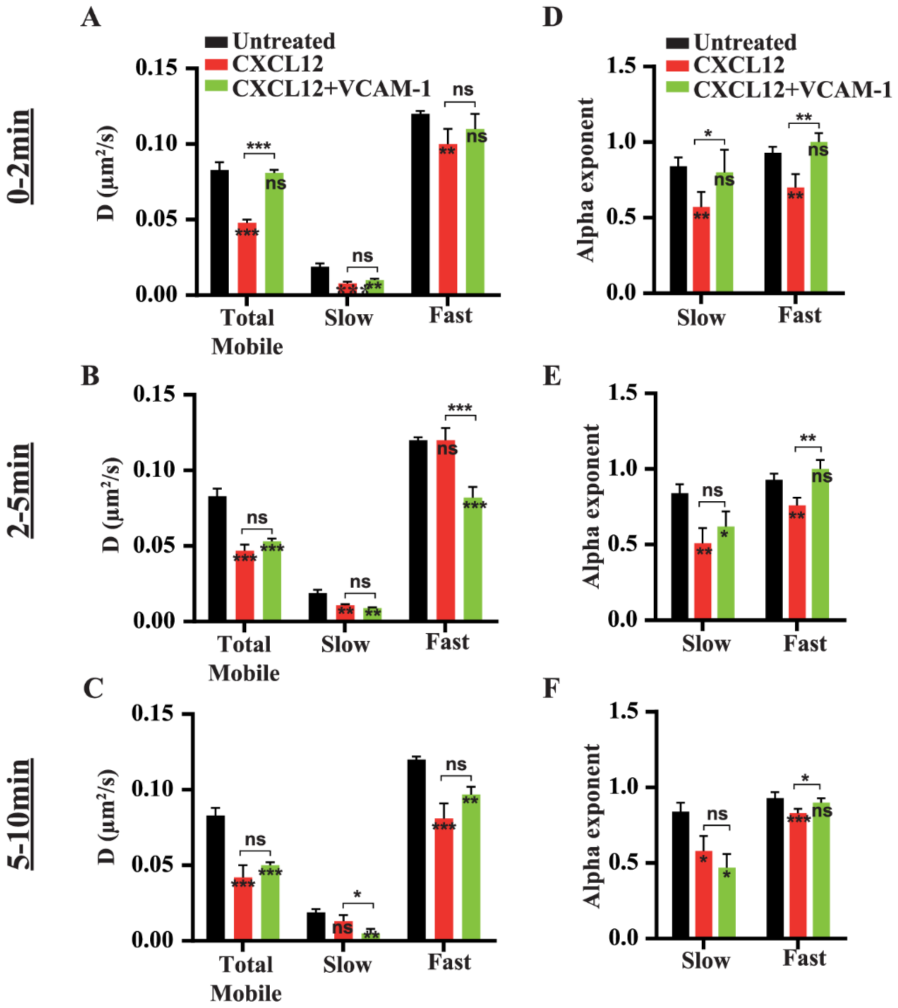

Figure 5.7 Effect of CXCL12 and VCAM-1 co-stimulation on the lateral mobility of α4β1 in T-cells. Diffusion coefficient of the total mobile trajectories, and slow and fast sub-populations (A-C) and alpha exponents (D-F) for the indicated stimulation conditions. (A, D) During 0-2 min. (B, E) During 2-5 min. (C, F) During 5-10 min.

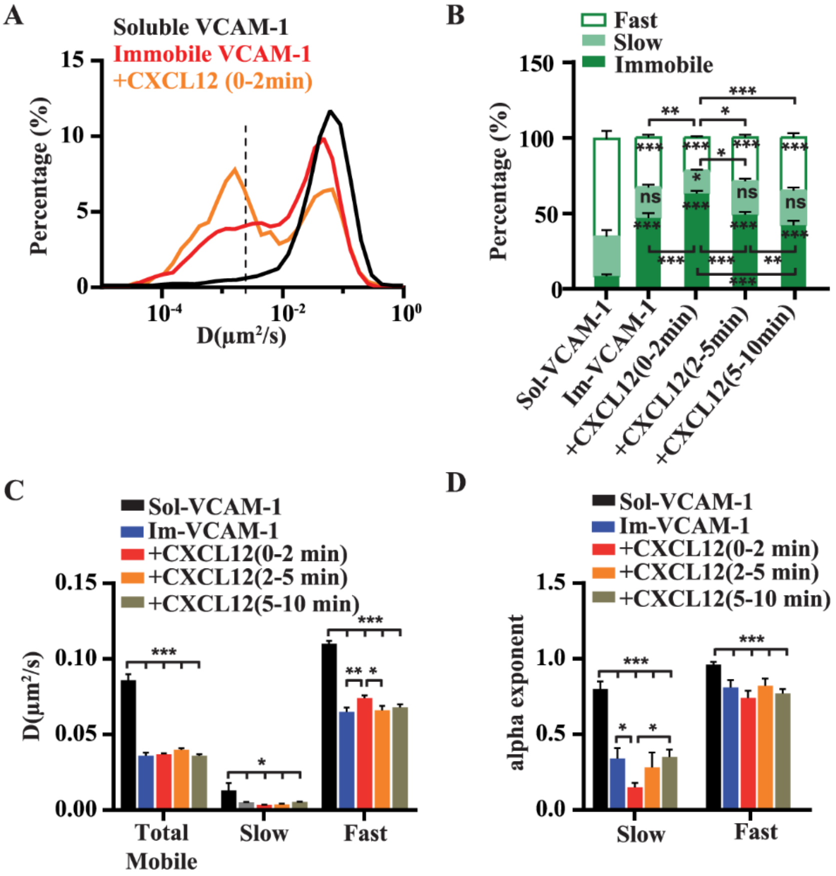

Figure 5.8 Effect of immobilized VCAM-1 and CXCL12 co-stimulation on the lateral mobility of α4β1 in T-cells. (A) Overlay semi-log distributions of D_{1-4} values for soluble VCAM-1 (black line), immobilized VCAM-1 (red), and immobilized VCAM-1 together with CXCL12 stimulation for 2 min (orange). Data from the soluble VCAM-1 stimulation experiments (Fig. 3) are included to allow easier comparison of both conditions. **(B)** Percentage of immobile, slow and fast α4β1 subpopulations for the different stimulating conditions and compared to soluble VCAM-1 (sol-VCAM-1). Im-VCAM-1 denotes immobilized VCAM-1. **(C)** Diffusion coefficients of the total mobile trajectories as well as the slow and fast subpopulations for the indicated conditions. **(D)** Alpha exponents of the slow and fast subpopulations for the indicated stimulations.18 untreated cells on immobilized VCAM-1 (1920 trajectories), 7 cells stimulated with CXCL12 for 0-2 min (759 trajectories), 8 cells stimulated with CXCL12 for 2-5min (865 trajectories) and 13 cells stimulated with CXCL12 for 5-10min (1588 trajectories) over 3 separate experiments.

cells seeded on immobilized VCAM-1. Immobilization of the ligand led to massive reduction of α4β1 mobility (**Fig. 5.8A**) and more than a four-fold increase on the percentage of immobilized integrins (**Fig. 5.8B**) compared to soluble ligand exposure (from 11% for soluble to 47% for immobilized VCAM-1). CXCL12 stimulation further increased α4β1 immobilization to 63% during the first two minutes of exposure (**Fig. 5.8B**). Once more, the effect of CXCL12 was transient such that after two minutes of chemokine stimulation, integrin immobilization progressively returned to similar values as to those without stimulation. Interestingly, ligand immobilization also reduced the diffusion of mobile integrins to values comparable to those obtained upon CXCL12 and Mn^{2+} treatments (compare **Fig. 5.8C, D** with **Fig. 5.3C** and **Fig. 5.4C**). Thus, these results indicate that immobilized but not soluble VCAM-1 triggers the activation of α4β1 integrins, which is further potentiated by chemokine stimulation.

Decrease in α4β1 lateral mobility by CXCL12 and CXCL12/VCAM-1 is linked to integrin activation. The results shown so far indicate that α4β1 immobilization is increased in T cells exposed to different integrin activating conditions. To further analyze if this increase is directly linked to α4β1 activation, we followed the time-dependent expression of a β1 activation epitope on CXCL12-exposed Molt-4 cells by means of flow cytometry. As activation reporter we used HUTS-21, an anti-β1 mAb that recognizes high-affinity β1 integrins (30). Since Molt-4 cells express predominantly α4β1 integrins (**Fig. 5.1**), HUTS-21 selectively reports on high-affinity α4β1. CXCL12 triggered a rapid induction of high-affinity α4β1 integrin conformations (**Fig. 5.9A**), with a strong reactivity to HUTS-21 already detected at 0.5 min of treatment. The induction of these high-affinity α4β1 forms decreased at longer times, although after 7.5 min, their expression levels were still notably higher as compared to untreated cells (**Fig. 5.9A**). VCAM-1-Fc alone was also able to induce high-affinity integrins at 0.5 min albeit to a lower extent as compared to CXCL12 (**Fig. 5.9B**). Importantly, co-stimulation by CXCL12 and VCAM-1-Fc resulted in a 2.5-fold increase in high-affinity integrins at 0.5 min, which remained remarkably above that of untreated conditions even after 7.5 min of co-stimulation (**Fig. 5.9B**). Of note, the activation of α4β1 by CXCL12/VCAM-1 remained higher up to 2.5 min than that of single CXCL12 or VCAM-1 at the 0.5 min time point.

Next, we assessed talin interaction with the β1 subunit as an additional measurement of integrin activation (31). To this purpose, we exposed Molt-4 cells for different times to CXCL12 and, following cell lysis, cell extracts were immunoprecipitated with the TS2/16 anti-β1 mAb and subjected to immunobloting using anti-β1 and anti-talin antibodies (14). Similar to the results obtained by flow cytometry using the HUTS-21 mAb, the immunoprecipitation data indicated that β1-talin association was rapid and transient, and was mainly detected in the first 5 min exposure to the chemokine, especially in the 0.5-1 min

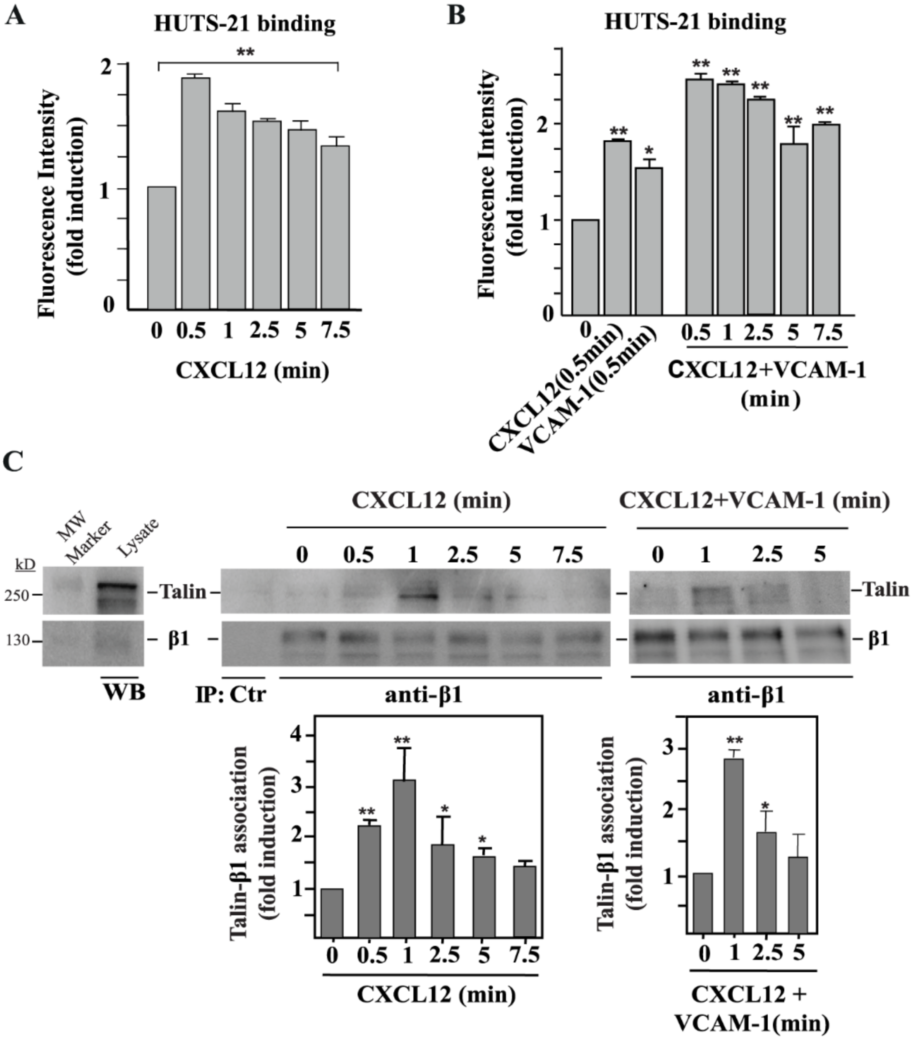

Figure 5.9 Analyses of α4β1integrin activation. (A, B) Molt-4 cells were exposed for the indicated times to CXCL12 or VCAM-1-Fc alone and subjected to flow cytometry with the HUTS-21 anti-β1mAb (N=3). **(C)** Cells were exposed to CXCL12 alone (middle panel) or combined with soluble VCAM-1-Fc (right panel) for the indicated times, and subsequently subjected to immunoprecipitation with the TS2/16 anti-β1 mAb followed by immunoblotting with antibodies to the indicated proteins. Also shown are densitometric analyses of gel bands from the immunoprecipitations displaying the mean ±SD of four independent experiments (bottom panels).

window, nicely coinciding (within the temporal accuracy of the experiments) with the reactivity to HUTS-21 (**Fig. 5.9C**, middle panel). Yet, under our experimental immunoprecipitation conditions, we were not able to detect further increase in β1-talin association upon addition of soluble VCAM-1 to CXCL12, as compared to incubation with CXCL12 alone (**Fig. 5.9C**, right panel). Together, these results further confirm that the reduction in α4β1 mobility upon CXCL12 stimulation observed by SPT directly correlates with the activation of this integrin. Furthermore, as talin connects the β subunits with the actin cytoskeleton, our data strongly suggest that the reduction observed on α4β1 mobility is the result of its increased talin-dependent interaction with the cytoskeleton.

The nanoscale spatial arrangement of α4β1 integrins is unaffected by integrin activation. To investigate the effect of integrin-activating conditions on the spatial regulation of α4β1, we performed high-resolution confocal and stimulated emission depletion (STED) super-resolution microscopy on Molt-4 cells. Cells were adhered onto PLL-coated slides, subjected to stimulation for 2.5 min by CXCL12, VCAM-1-Fc or a combination of both, followed by rapid fixation and staining using HUTS-21. To estimate changes in the number of high-affinity integrins as a function of the stimulating conditions, we performed extensive confocal imaging of individual cells (**Fig. 5.10A**), and analyzed the images in terms of their fluorescence intensity. The largest increase in fluorescent intensity, and therefore the largest enhancement in the number of high-affinity α4β1 molecules, was obtained upon co-stimulation with CXCL12 and VCAM-1-Fc (**Fig. 5.10B**). Stimulation with VCAM-1 or

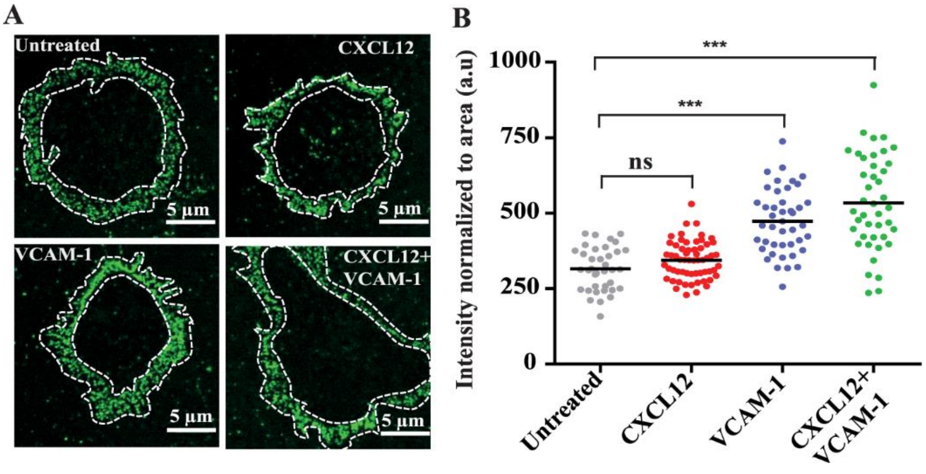

Figure 5.10 Effect of CXCL12 and/or VCAM-1 on the lateral organization of high-affinity α4β1 in T cells. (A) Representative confocal images of Molt-4 cells labeled with HUTS-21 mAb for different stimulating conditions. The white dash lines denote the regions of the cell membrane subjected to fluorescent intensity analysis. **(B)** Fluorescent intensity of HUTS-21 mAb normalized to the area for different conditions from confocal images of individual cells. Each dot corresponds to an individual cell. Unless indicated, statistical comparisons are being done with respect to untreated cells.

CXCL12 alone also led to an increase, albeit more modest, of activated α4β1. Surprisingly, stimulation with VCAM-1-Fc appeared to induce a higher number of high-affinity integrins than exposure to CXCL12, in apparent contradiction to the mobility data shown above.

To then map the nanoscale organization of high-affinity integrins under different stimulation conditions, we switched to STED imaging using the HUTS-21 mAb. With an increased spatial resolution of ~120nm (**Fig. 5.11**), individual fluorescent spots became clearly distinguishable from the images (**Fig. 5.12A**). Individual spots were identified and their intensity quantified and normalized to the mean spot intensity obtained for untreated cells. Interestingly, very little differences in spot intensities were observed amongst the different conditions (**Fig. 5.12B**).

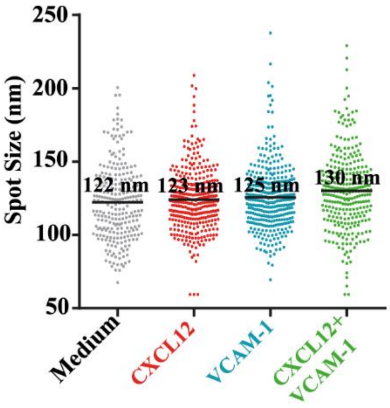

Figure 5.11 Nanoscale organization of high-affinity α4β1 integrins on T cells. Spot size distribution was obtained by STED imaging of high-affinity integrins using the HUTS-21 mAb on Molt-4 cells incubated under the indicated conditions. Spots sizes are in all cases around 120nm, which correspond to the STED resolution under our experimental conditions. Therefore, these data do not reflect the real sizes of the fluorescent spots, indicating that if nanoclustering occurs, their sizes are well below the STED resolution and thus not directly measurable.

Only co-stimulation of T-cells with CXCL12 and VCAM-1-Fc resulted in a slight but significant increase in the mean spot intensity, with an average number of high-affinity integrins per spot ~1.4 times larger than on unstimulated cells. As the fluorescence intensity in each spot is proportional to the number of molecules, these results indicate no major changes in the nanoscale organization of α4β1 for the different stimulating conditions. As additional quantification, we also measured the spatial proximity between adjacent fluorescent spots. Cells stimulated with CXCL12 or VCAM-1-Fc alone showed a modest but significant reduction in their spatial proximity that became more pronounced upon co-stimulation with CXCL12 and VCAM-1-Fc, as compared to untreated cells (**Fig. 5.12C**). Taken together, these results indicate that the nanoscale organization of high-affinity α4β1 remains largely unaltered under the investigated stimulating conditions. Instead, the increased proximity of individual spots upon co-stimulation with CXCL12 and VCAM-1 suggests that newly formed high-affinity α4β1 integrins distribute on the cell membrane as independent units instead of joining pre-established integrin sites to form nano- or microclusters.

5.3 Discussion

Using single molecule dynamic approaches together with super-resolution imaging, we have explored the lateral mobility and spatial arrangement of individual α4β1 integrins on T cells exposed to different stimuli that promote integrin activation, with a particular emphasis on the role of chemokines. Our data demonstrate that conditions that promote α4β1 activation, such as incubation with the chemokine CXCL12, trigger α4β1 immobilization, most probably through talin recruitment to the integrin. These results are fully in line with recent reports on other integrins, including β1 and β3 integrins associated to focal adhesion (FAs), and on αLβ2 on leukocytes, where integrin immobilization correlated with integrin activation (32). Also, in analogy to other integrins (19, 32), robust immobilization of α4β1, triggered in our case by CXCL12 stimulation, requires the tripartite interaction between α4β1, its ligand VCAM-1 and actin-binding proteins such as talin.

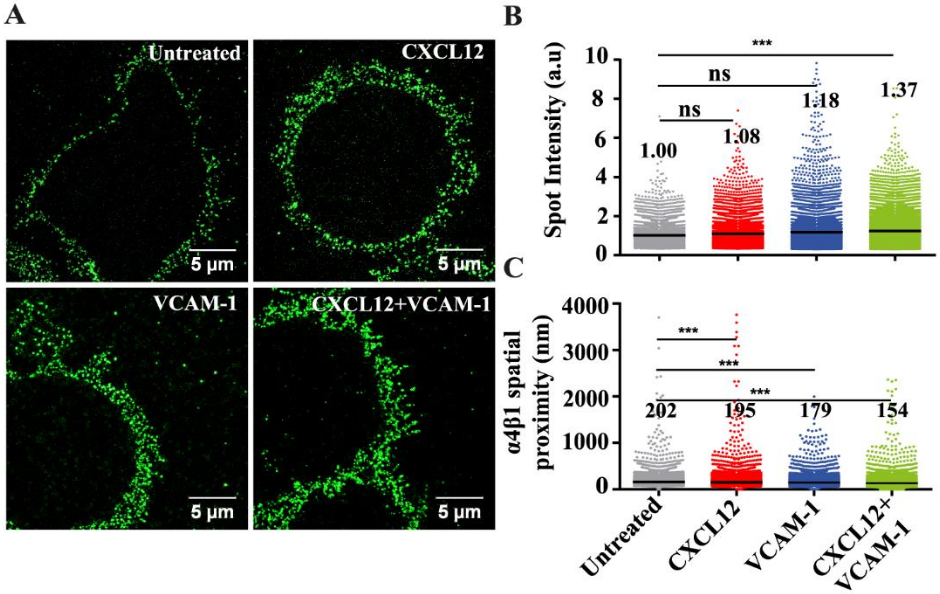

Figure 5.12 Nanoscale organization of high-affinity α4β1 integrins on T cells. (A) Representative STED images of Molt-4 cells subjected to the indicated stimuli and stained with the HUTS-21 mAb. **(B)** Distribution of spot intensity per condition (at least 10 cells per condition). Values displayed indicate the mean of the distribution. **(C)** Distribution of α4β1 spatial proximity on the different conditions (at least 10 cells per condition). Values displayed indicate the mean of the distribution.

While CXCL12 was able to trigger rapid immobilization and to restrict the diffusion of α4β1 integrins, co-stimulation by the chemokine together with soluble VCAM-1 resulted in a five-fold increase of immobile integrins as compared to untreated cells. Although SPT approaches revealed that T cell binding to soluble VCAM-1 was capable of inducing immobilization of a small-subset of α4β1, its overall effect on the integrin mobility was very modest. Surprisingly, confocal and STED imaging using the activation-reporter HUTS-21 anti-β1mAb showed the induction of a larger number of high-affinity integrins upon VCAM-1 stimulation as compared to CXCL12 stimulation. Together, these results suggest that while soluble VCAM-1 is able to induce high-affinity α4β1 integrins, this sub-set of integrins is most likely not bound to the actin cytoskeleton, remaining therefore mobile. As such, α4β1 true activation in the sense of generation of high- affinity forms and actin cytoskeleton anchorage (through recruitment of talin) mostly occurs upon CXCL12 stimulation, which is then potentiated by co-stimulation with VCAM-1. This effect is consistent with the role of ligands in stabilizing the active form of integrins brought about by chemokine-induced transient stimulation (33).

We also performed SPT experiments of α4β1 in the presence of immobilized VCAM-1. In stark contrast to soluble ligand, immobilized VCAM-1 led to a massive immobilization of the integrin and reduction of its lateral mobility. These results can be rationalized in the context of mechanical forces being exerted between the mobile integrin and the immobilized ligand. As the integrin laterally diffuses on the cell membrane, the fixed ligand resists translation of the integrin, increasing the force and resulting in extension of the β-subunit and activation of the integrin. This force-induced activation will then lead to integrin anchorage to the actin cytoskeleton and its immobilization. Addition of chemokines will further contribute to the activation of α4β1, so that the overall result is the generation of a large population of active integrins that anchor to the cytoskeleton via talin, and their concomitant immobilization on the cell surface as observed in our experiments. Such a traction force model has been already proposed for αLβ2 integrins to explain the substantially higher affinity of αLβ2 for ligand on substrates as compared to the solution phase (29).

The overall conclusions of our work are based both on the well-accepted role that talin plays in the transmission of inside-out signaling induced by chemokines for the generation of active α4β1 and αLβ2 integrins (13, 14, 34), and on our present results achieved using a combination of different techniques to link integrin activation and integrin immobilization. Thus, our data reveals a direct correlation between rapid and transient α4β1 immobilization with talin association with β1 and induction of HUTS-21 epitopes, which constitute clear indications of integrin activation. Therefore, talin anchors the activated integrin to the actin cytoskeleton, favoring receptor immobilization. Interestingly, while the generation by CXCL12 of high-affinity α4β1 integrins and their immobilization persisted for more than 5 min, as detected with the HUTS-21 mAb, association of talin to α4β1 after chemokine stimulation was short-lived. These results might indicate that talin is only involved in bridging the first contacts between α4β1 and the actin cytoskeleton, while other proteins, including kindlin-3 (10), could concomitantly or subsequently cooperate with talin to stabilize the active conformation and immobilization of α4β1 over several minutes.

To facilitate T cell adhesion, crawling and diapedesis on and across the endothelium for efficient cell trafficking towards sites of inflammation, integrin-mediated adhesion (mainly involving α4β1 and αLβ2) to their respective ligands must be brief and highly dynamic, which is contributed by chemokines. This process is phenomenologically different to that of cell adhesion involving FAs, where the formation of FA clusters involving β1 and β3 integrins is required (32). Our results provide novel insights on the different biophysical properties of integrin adhesion associated to these two processes. Whereas in both cases, integrin activation occurs, long-lived and robust integrin immobilization is observed on FAs as well as in the formation of large integrin-enriched microclusters (35-37). In remarkable contrast, our results indicate that physiological conditions that promote integrin activation, such as chemokines, lead to a modest but significant sub-set of transiently active and immobile α4β1 integrins on T cells, with no significant changes in their nanoscale spatial organization. As a low number of leukocyte integrins is involved in adhesive contacts with their ligands, their interaction is expected to be brief and highly dynamic, allowing effective T cell migration. In summary, our data indicate that fine-tuning and tight regulation of α4β1 immobilization and spatial arrangement on the cell surface, are crucial processes that modulate the integrin adhesiveness.

5.4 Experimental procedures

Cells, antibodies and reagents. The human Molt-4 T cell line was cultured in RPMI 1640 medium (Lonza, Verviers, Belgium) and 10% fetal bovine serum (Gibco, Paisley, UK). Control P3X63 and anti-β1 TS2/16 mAb were gifts from Dr. Francisco Sánchez-Madrid (Hospital de la Princesa, Madrid, Spain), and polyclonal anti-β1A antibodies were from Dr. Guido Tarone (Turin University, Italy). The clone 18 anti-β1 and the HUTS-21 anti-β1 mAb were from Becton Dickinson (Franklin Lakes, NJ), and the talin clone 8D4 antibody was from Sigma-Aldrich (St Louis, MO). CXCL12 was purchased from R&D Systems (Minneapolis, MN). Streptavidine-coated QD, biotin and the secondary antibody goat-anti-mouse conjugated to Alexa Fluor 488 were purchased from Invitrogen (Eugene, OR). PLL and PFA were from Merck (Darmstadt, Germany).

Flow cytometry. For detection of high-affinity β1 by flow cytometry, cells were stimulated for different times with CXCL12 and/or VCAM-1-Fc (R&D Systems) and fixed with 2% PFA before adding the HUTS-21 anti-β1mAb (10µg/ml) for 30 min at 4ºC. After washing, cells were incubated with Alexa fluor 488-conjugated rabbit anti-mouse IgG (Jackson Immunoresearch Lab.). Fluorescence intensity data indicate fold-induction values relative to those from control untreated cells, which were given an arbitrary value of one.

Immunoprecipitation. We essentially followed the same methodology as described (38). Briefly, cell lysate supernatants were incubated with antibodies followed by coupling to protein G-sepharose. Proteins were separated by SDS-PAGE, transferred to PVDF membranes, which were sequentially incubated with primary antibodies and with horseradish peroxidase-conjugated secondary antibodies. Protein visualization was achieved using Immobilon Western chemiluminescent substrate (Millipore, Billerica, MA).

QD-antibody conjugation. Streptavidine-coated QD655 were added to an equimolar solution of biotinylated clone 18 anti-β1antibody and a 5-fold excess of free biotin in order to obtain a 1:1 anti-β1-QD ratio. The mixture was then gently shaken for two hours at 4ºC and the concentration was finally adjusted to obtain sub-labeling conditions (~0.5 µg/ml).

Sample Preparation for SPT. Samples were prepared as described in Chapter 2. Briefly, Molt-4 cells were diluted to $8x10^5$ per ml in RPMI 1640 medium and spread on PLL coated coverslips (Fluorodishes; 35 mm, Menzel Glases) for 30 min. Subsequently, cells were blocked for 15 min and then 200µl of the clone 18 anti-β1-QD655 conjugate was added to the cells for 3min at room temperature. After washing the cells, samples were placed under a SPT microscope and after recording individual trajectories for 10 min, the medium was removed and 200µl of the different stimuli (either CXCL12 at 200ng/ml, $MnCl_2$ at 0.5mM, soluble VCAM-1-Fc at 20µg/ml, or combined CXCL12 and VCAM-1-Fc) were added to samples for the following 10 min.

VCAM-1-Fc immobilization and sample preparation for SPT. 100µl of goat-human IgG F $(ab')_2$ (100µg/ml, Jackson ImmunoResearch, PA) were passively absorbed onto the center of 35 mm glass coverslips by incubating for 60 min. The anti-Fc-coated area was then incubated with

100µl of VCAM-1-Fc (20µg/ml) for 60 min. Molt-4 cells were stretched onto immobilized VCAM-1 substrates for 30 min. labeling of α4β1 integrins for SPT experiments and CXCL12 stimulation were performed as described above.

Sample preparation for Confocal and STED imaging. Chambered cover glasses (8 wells, Nunc Lab-TekII, Rochester, NY) were coated with 0.2ml of PLL (10mg/ml) for 30 min at 37ºC. Cells were re-suspended in RPMI 1640 medium to a final concentration of $8x10^5$ per ml and attached to the bottom of glasses by incubation for 30 min. Subsequently, cells were incubated for 2.5 min with the different soluble stimuli using the same concentrations as for the SPT analyses. Immediately after, samples were fixed using 2% PFA and blocked for 1h at room temperature with 3% BSA, 2% HS and 20mM glycine in PBS. Next, 150 µl of the HUTS-21 mAb (5µg/ml) was added at room temperature for 30 min, followed by secondary labeling with Alexa-Fluor488 goat anti-mouse (5 µg/ml). Finally cells were fixed again with 2% PFA.

SPT set-up & trajectory analysis. Single QD655 tracking was performed using a custom setup built around an inverted microscope (IX70, Olympus) as described in Chapter 2. During a typical experiment, movies of 1000 frames were recorded every 60 s at a frame rate of 62 Hz. Individual trajectories were generated and analyzed as explained in Chapter 2.

Confocal and STED imaging. Both confocal and STED super resolution images of T cells were collected with a commercial microscope (CW-STED SP-5, Leica Microsystems) equipped with an oil immersion objective (HCX PL APO CS 100.0x, Leica) with 1.4 NA as described on Chapter 2.

Analysis of STED images. Analysis of STED images was performed using the algorithm described in Chapter 2 based on the decomposition of intensity peaks with PSFs obtained from single markers (39). Spatial proximity was quantified by determining for each spot, the distance at which the nearest neighbor was located.

Statistical Analysis. Results are displayed as mean ± SD, calculated from separate experiments. To determine statistical differences between the mean of different data sets, the One-way ANOVA test was used, followed by the Turkey's multiple comparison test (**Figs. 5.2, 5.4-5.8**). For non-Gaussian distributed data sets, statistical differences between the means were calculated using the Kruskal-Wallis test, followed by Dunn´s multiple comparison test (**Figs. 5.9B and**

5.11). The resulting P values are indicated as follows: ns (no significant: P >0.05); * (P<0.05); ** (P <0.01) and *** (P <0.001).

5.5 References

1. Hynes R.O., *Integrins: Bidirectional,* Allosteric Signaling Machines. *Cell* (2002) **110**, 673-687.
2. Alon R., Kassner P. D., Carr M. W., Finger E. B., Hemler M. E., and Springer T. A., The integrin VLA-4 supports tethering and rolling in flow on VCAM-1. *J. Cell Biol.,* (1995) **128**, 1243-1253.
3. Hogg N., Henderson R., Leitinger B., McDowall A., Porter J., and Stanley P., Mechanisms contributing to the activity of integrins on leukocytes. *Immunol. Rev.*, (2002) **186**, 164-171.
4. Luster A. D., Alon R., and von Andrian U. H., Immune cell migration in inflammation: present and future therapeutic targets. *Nat. Immunol.,* (2005) **6**, 1182-1190.
5. Ley K., Laudanna C., Cybulsky M. I., and Nourshargh S. Getting to the site of inflammation: the leukocyte adhesion cascade updated. *Nat. Rev. Immunol.*, (2007) **7**, 678-689
6. Alon R. and Feigelson S. W., Chemokine-triggered leukocyte arrest: force-regulated bi-directional integrin activation in quantal adhesive contacts. *Curr. Opin. Cell Biol.*, (2012) **24**, 670-676.
7. Laudanna C., Kim J. Y., Constantin G., and Butcher E., Rapid leukocyte integrin activation by chemokines. *Immunol. Rev.,* (2002) **186**, 37-46
8. Thelen M. and Stein J. V., How chemokines invite leukocytes to dance. *Nat. Immunol.,* (2008) **9**, 953-959.
9. Hogg N., Patzak I., and Willenbrock F., The insider's guide to leukocyte integrin signalling and function. *Nat. Rev. Immunol.,* (2011) **11**, 416-26.
10. Moser M., Legate K. R., Zent R., and Fässler R., The tail of integrins, talin, and kindlins. *Science,* (2009) **324**, 895-899
11. Kim C., Ye F., and Ginsberg M. H., Regulation of integrin activation. *Annu. Rev. Cell Dev. Biol.*, (2011) **27**, 321-345.
12. Calderwood D. A., Campbell I. D., and Critchley D. R., Talins and kindlins: partners in integrin-mediated adhesion. *Nat. Rev. Mol. Cell Biol.*, (2013) **14**, 503-517.

13. Manevich E., Grabovsky V., Feigelson S. W., and Alon R., Talin 1 and paxillin facilitate distinct steps in rapid VLA-4-mediated adhesion strengthening to vascular cell adhesion molecule 1. *J. Biol. Chem.,* (2007) **282**, 25338-25348

14. García-Bernal D., Parmo-Cabañas M., Dios-Esponera A., Samaniego R., Hernán-P d. l. O. D., and Teixidó J., Chemokine-induced Zap70 kinase-mediated dissociation of the Vav1-talin complex activates α4β1 integrin for T cell adhesion. *Immunity,* (2009) **31**, 953-964

15. García-Bernal D., Wright N., Sotillo-Mallo E., Nombela-Arrieta C., Stein J. V., Bustelo X. R., and Teixidó J., Vav1 and Rac Control Chemokine-promoted T Lymphocyte Adhesion Mediated by the Integrin α4β1. *Mol. Biol. Cell.,* (2005) **16**, 3223-3235

16. Constantin G., Majeed M., Giagulli, C., Piccio L., Kim J. Y., Butcher E. C., and Laudanna C., Chemokines trigger immediate β2 integrin affinity and mobility changes: Differential regulation and roles in lymphocyte arrest under flow. *Immunity,* (2000) **13**, 759–769

17. Cairo C. W., Mirchev R., and Golan D. E., Cytoskeletal regulation couples LFA-1 conformational changes to receptor lateral mobility and clustering. *Immunity,* (2006) **25**, 297–308

18. Bakker G. J., Eich C., Torreno-Pina J. A., Diez-Ahedo R., Perez-Samper G., van Zanten T. S., Figdor C. G., Cambi A., and Garcia-Parajo M. F. Lateral mobility of individual integrin nanoclusters orchestrates the onset for leukocyte adhesion. *Proc. Natl. Acad. Sci. USA,* (2012) **109**, 4869–4874

19. Borgman K. J. E., van Zanten T. S., Manzo C., Cabezón R., Cambi A., Benítez-Ribas D., and Garcia-Parajo M. F., Priming by chemokines restricts lateral mobility of the adhesion receptor LFA-1 and restores adhesion to ICAM-1 nano-aggregates on human mature dendritic cells. *PloS One,* (2014) **9**, e99589

20. Chen H., Titushkin I., Stroscio M., and Cho M. Altered membrane dynamics of quantum dot-conjugated integrins during osteogenic differentiation of human bone marrow derived progenitor cells. *Biophys. J,.* (2007) **92**, 1399-1408

21. Yauch R. L., Felsenfeld D. P., Kraeft S-K., Chen L. B., Sheetz M. P., and Hemler M. E., Mutational Evidence for Control of Cell Adhesion Through Integrin Diffusion/Clustering, Independent of Ligand Binding. *J. Exp. Med.,* (1997) **186**, 1347-1355.

22. Schütz G. J., Schinler H., and Schmidt T., Single-molecule microscopy on model membranes reveals anomalous diffusion. *Biophys. J.,* (1997) **73**, 1073-1080

23. Springer T.A., *Traffic signals for lymphocyte recirculation and leukocyte emigration: the multistep paradigm. Cell*, (1994) **76**, 301-14.

24. Butcher E.C. and Picker L. J., *Lymphocyte homing and homeostasis. Science,* (1996) **272**, 60-66.

25. Grabovsky V., Feigelson S., Chen C., Bleijs D. A., Peled A., Cinamom G., Baleux F., Arenzana-Seisdedos F., Lapidot T., van Kooyk Y., Lobb R. R., and Alon R., Subsecond induction of α4 integrin clustering by immobilized chemokines stimulates leukocyte tethering and rolling on endothelial vascular cell adhesion molecule 1 under flow conditions. *J. Exp. Med.*, (2000) **192**, 495-506

26. Sanz-Rodriguez F., Hidalgo A., and Teixido J., Chemokine stromal cell-derived factor-1alpha modulates VLA-4 integrin-mediated multiple myeloma cell adhesion to CS-1/fibronectin and VCAM-1. *Blood*, (2001) **97**, 346-351.

27. Dransfield I., Cabañas C., Craig A., and Hogg N., Divalent cation regulation of the function of the leukocyte integrin LFA-1. *J. Cell Biol.*, (1992) **116**, 219-226.

28. Takagi J., Petre B. M., Walz T., and Springer T. A., Global conformational rearrangements in integrin extracellular domains in outside-in and inside-out signaling. *Cell*, (2002) **110**, 599-611.

29. Schürpf T. and Springer T. A., Regulation of integrin affinity on cell surfaces. *EMBO J.*, (2011) **30**, 4712-4727.

30. Luque A., Gómez M., Puzon W., Takada Y., Sánchez-Madrid F., and Cabañas C., Activated conformations of very late activation integrins detected by a group of antibodies (HUTS) specific for a novel regulatory region (355-425) of the common β1 chain. *J. Biol. Chem.*, (1996) **271**, 11067-11075.

31. Tadokoro S., Shattil S. J., Eto K., Tai V., Liddington R. C., de Pereda J. M., Ginsberg M. H., and Calderwood D. A., Talin binding to integrin beta tails: a final common step in integrin activation. *Science*, (2003) **302**, 103-106

32. Rossier O., Octeau V., Sibarita J. B., Leduc C., Tessier B., Nair D., Gatterdam V., Destaing O., Albigès-Rizo C., Tampé,R., Cognet L., Choquet D., Lounis B., and Giannone G., Integrins β1 and β3 exhibit distinct dynamic nanoscale organizations inside focal adhesions. *Nat. Cell Biol.*, (2012) **14**, 1057-1067.

33. Shamri R., Grabovsky V., Gauguet J. M., Feigelson S., Manevich E., Kolanus W., Robinson M. K., Staunton D. E., von Andrian U. H., and Alon R., Lymphocyte arrest requires instantaneous induction of an extended LFA-1 conformation mediated by endothelium-bound chemokines. *Nat. Immunol.*, (2005) **6**, 497-506.

34. Lefort C. T., Rossaint J., Moser M., Petrich B. G., Zarbock A., Monkley S. J., Critchley D. R., Ginsberg M. H., Fassler R., and Ley K., Distinct roles for talin-1 and kindlin-3 in LFA-1 extension and affinity regulation. *Blood*, (2012) **119**, 4275-4282.

35. Schoenwaelder S. M., and Burridge K., Bidirectional signaling between the cytoskeleton and integrins. *Curr. Opin. Cell Biol.*, (1999) **11**, 274–286.

36. Gallant N. D., Michael K. E., and García A. J., Cell adhesion strengthening: contributions of adhesive area, integrin binding, and focal adhesion assembly. *Mol Biol. Cell.*, (2005) **16**, 4329–4340.

37. Wolfenson H., Lavelin I., and Geiger B., Dynamic regulation of the structure and functions of integrin adhesions. *Dev. Cell*, (2013) **24**, 447-458.

38. Ticchioni M., Charvet C., Noraz N., Lamy L., Steinberg M., Bernard A., and Deckert M., Signaling through Zap70 is required for CXCL12-mediated T-cell transendothelial migration. *Blood*, (2002) **99**, 3111-3118.

39. Manzo C., van Zanten T. S., Saha S., Torreno-Pina J. A., Mayor S., and Garcia-Parajo M. F., PSF decomposition of nanoscopy images via Bayesian analysis unravels distinct molecular organization of the cell membrane. *Sci. Rep.*, (2014) **4**, 4354.

Chapter 6

General discussion & Future perspectives

In this Chapter we summarize the main conclusions of this thesis and provide directions for future research. We first discuss the main imaging techniques, tools for cell mechanical stimulation and computational algorithms used throughout this thesis, highlighting the importance of using combined approaches. In particular, we examine the main advantages and drawbacks of performing single particle tracking on our stretching device. Moreover, we propose possible experiments to further assess the effect of mechanical forces on the activation, lateral mobility and spatial organization of the integrin receptor αLβ2 on T cells. We then present the main conclusions regarding the influence of shear flow on the lateral organization of the transmembrane receptor ICAM-1 expressed on endothelial cells (ECs) and its implications on the migration of leukocytes across mechanically stimulated ECs. Finally, we summarize the main findings on the diffusing behavior of the integrin receptor α4β1 expressed on T cells in presence of chemokines and/or ligand stimulation.

6.1 An emerging paradigm in cell biology: from qualitative to quantitative descriptions.

In this research we have combined a number of cutting-edge biophysical techniques, including single molecule dynamic approaches, super-resolution optical microscopies, novel algorithms for data quantification and devices that allow mechanical stimulation of cells to study the spatiotemporal organization of integrin receptors and their respective ligands in cells of the immune system under different stimulation conditions. Migration of leukocytes to sites of injury and/or infection is crucial for the proper development of the immune response in our body (1, 2). This complex process is orchestrated by the coordinated activation and spatiotemporal organization of cell membrane receptors, which in turn is modulated by biochemical and mechanical stimuli (3, 4). The identification and further characterization of the different steps and underlying molecular mechanisms taking place during the leukocyte migration process has been possible thanks to the innovation of diverse tools for cell mechanical stimulation and microscopy-based visualization techniques. Indeed, the possibility of combining tools that enable the simulation of the *in-vivo* cell conditions with state-of-art microscopy techniques constitutes the key to many discoveries realized in the last few years. Moreover, the development of computational algorithms capable of automatically extracting statistically relevant information from cell microscopy images has become essential during the last decade in the field of biophysics. Therefore, it is fair to say that these biophysical tools are contributing to a change in the way that cell biology is approached nowadays, from the more standard qualitative description of cellular phenomena to a much more quantitative picture of the molecular processes responsible for cell function.

In this thesis we have combined tools for cell mechanical stimulation with advanced microscopy techniques in order to investigate the molecular basis of cell mechanosensing and mechanotransduction. In Chapter 2 we offer a suitable approach to perform single particle tracking (SPT) on cells spread onto elastic substrates to which isotropic and controllable stresses can be applied. The use of quantum dots (QDs) as a fluorescence probe has been decisive in these experiments due to their photostability in time and high photon emission (5), which allowed a reasonable signal-to-background compromise in the fluorescence emission through the elastic (PDMS) substrate. However, QDs still have two major drawbacks: their characteristic blinking (6, 7) and their relative large size (8). While blinking prevents the acquisition of long trajectories, their size might interfere with the stoichiometry of the molecules targeted thus producing undesired artifacts. Recently, non-blinking QDs have been developed that allow recording longer trajectories than those obtained when using blinking QDs in SPT experiments

(9, 10). Moreover, the potential artifacts associated with the size of the QDs can be easily assessed by performing control SPT experiments using organic fluorescent dyes as a probe, whose size is ~60 times smaller (8). Nevertheless, in the context of the SPT experiments on cells subjected to mechanical stress, as performed in Chapter 2, the size of QDs might be introducing another artifact not related to a direct interference with the stoichiometry of the protein. In this particular case the relatively large size of QDs might lead to unwanted interactions with the underlying substrate due to an increased proximity of the cell membrane to the PDMS substrate after force application. This may lead to a reduction on the mobility of the tagged protein, as we observed in this thesis for the integrin αLβ2 expressed on T-cells. Unfortunately, the low brightness of most organic dyes makes them unsuitable for their visualization through PDMS membranes. Thus, additional experiments should be performed to discern whether the reduction observed in αLβ2 mobility upon stretching is a consequence of integrin activation or an artifact due to the size of the QDs. One possible experiment that could shed some light on this question is the disruption of the actin cytoskeleton. Previous works have shown that the reduced mobility of αLβ2 is correlated to an increased interaction with the cytoskeleton (11, 12). If that would be the case, the disruption of the cytoskeleton upon application of cell stress, will produce the release of the αLβ2 integrins, thus inducing the recovery of their mobility. In addition, one could use specific antibodies labeling the extended conformation of αLβ2 and assess whether there is an increase of the population of extended integrins as a result of mechanical stimulation. Unfortunately, we did not succeed in biotinlylating these specific antibodies, a condition that is necessary for QD attachment. A more direct and sophisticated test involves the use of elastic patterned substrates with alternating concave and convex architectures. By using such approach the cell will attach to the more elevated region of the substrate and the tracking of QDs would be performed within the deeper regions. This will increase the effective distance between the QDs and the substrate, thus avoiding undesired interactions.

In Chapter 4 we used a parallel-plate flow chamber (PPFC) to investigate the influence of laminar shear flow on the lateral distribution of the αLβ2 ligand ICAM-1 expressed on endothelial cells (ECs). Although the PPFC was able to induce shear flow conditions similar to the physiological ones, the rate of success in this type of experiments was quite low (<30%). This was mainly due to the formation of bubbles inside the PPFC upon the introduction of new reagents into the flow circuit, or due to high pressure values transmitted to the cell during assembly and disassembly of the PPFC. Both technical complications led to serious damage on the cell culture, thus invalidating the experiment. Moreover, the high volume of the chamber (~2ml) requires the use large amount of reagents which is ultimately translated in more costly experiments. An alternative approach to PPFC is the use of microfluidic devices. They offer both higher performance and reduced amount of reagent to use (13). However, the use of microfluidic devices introduces others challenges associated with the type of substrate used (usually PDMS) and the relatively high ratio of cell number to medium volume (14). While the first factor affects the attachment of some types of cells, the second might lead to insufficient medium supply required for the proper cellular functioning. Although the PDMS can be functionalized with specific ligands to promote cell adhesion, this extra step adds complexity to the microfluidic device. Thus, when using a microfluidic device, special caution must be taken in the compatibility between the substrate and the type of cells used as well as in finely adjusting the concentration of reagents used.

Superresolution STED nanoscopy has been another important technique used in this thesis as it allows assessing the changes in the lateral nanoscale organization of different cell membrane receptors under different stimulating conditions. Unfortunately, the poor temporal resolution of STED does not allow investigating the dynamics of single receptors at the cell membrane. Thus, in order to address the spatiotemporal behavior of transmembrane receptors, STED must be used in combination with others techniques like SPT, as both complement each other. Hence, in Chapter 5 we combined both approaches to investigate the dynamic and spatial organization of $\alpha4\beta1$ on T-cells exposed to different stimulating conditions. Nevertheless, a technique capable of unifying both high temporal and spatial resolution would be ideal to characterize dynamic events on the cell membrane. A plausible alternative would be performing STED with high temporal resolution. However, increasing the temporal resolution of STED is still challenging given the fact that it is a scanning technique. Moreover, it would be impossible, or at least very difficult, to reconstruct long trajectories of the diffusing molecules if the dye used as a probe photobleaches after a few images. In this sense, the development of more photostable fluorophores for STED applications is essential. In addition, the STED resolution of the setup used for the experiments presented in this thesis is ~100 nm, still larger than the size of many of the biological components localized on the cell membrane (15, 16). As mentioned in Chapter 1, the spatial resolution of STED can be improved by using pulsed instead of continuous wave (CW) STED lasers. However, this approach requires more complex and expensive setups. Nevertheless, many groups nowadays used pulsed STED and it could be readily implemented in our Facility.

Another distinctive feature in biophysical research nowadays is the use of sophisticated computational algorithms to analyze the imaging data collected experimentally. For instance, one cannot conceive SPT without taking into account the algorithms that perform the reconnection of trajectories and automatic algorithms for analysis of hundreds to thousands of individual trajectories. In the same way, is unthinkable to perform cluster analysis of STED images without the algorithms capable of quantifying the size and intensity of individual markers. Although there are several available softwares for biophysical data analysis, they are either too general or designed to work under specific experimental conditions focusing on particular applications. Thus, the implementation of algorithms for the analysis of particular experimental data is an emerging and growing requirement in biophysical research labs nowadays. Through this thesis we have used various existent algorithms (many of them custom-made in the Lab) to analyze the images obtained using the different microscopy techniques and to extract relevant statistical information from them. In addition, we have developed a new algorithm to track the centroid position of leukocytes migrating on ECs under shear flow conditions. In chapter 3 we have also described a new algorithm for the detection of changes of slopes in noisy trajectories, such as those obtained by tracking the T-cell displacement on ECs. The algorithm returns a piecewise linear segmentation of the data input, from where the different slopes and duration times can be extracted. Similar algorithms, grouped in the category of bottom-up algorithms, have been described in the literature (17). Most of them are based on partitioning the initial data in an arbitrary number of segments of equal length that are consecutively merged until some stopping criteria are met (17). Such stopping conditions are usually given by either the number of segments or by an error threshold fixed by the user, which are usually unknown quantities. To overcome this difficulty, the first part of our algorithm (WINLINFIT) uses a likelihood-based approach that estimates the points where there are potential changes of slopes, and thus provides an initial guess for the number of segments. Moreover, the algorithm includes a routine to estimate the error from the data. In addition, to reduce the number of possible false positive events, the method includes a second part (MERGING) that merges the consecutive segments with certain probability given by the parameter α. Although we showed that a value of $\alpha=0.95$ leads to a relatively good performance of the algorithm, further simulations focused on the influence of this parameter in the overall performance of the algorithm should be performed.

Since the only requirement of the algorithm is that the noise in the data is Gaussian, the method is quite general and therefore can be applied to different biophysical process, such as DNA elongation via magnetic and optical tweezers (18, 19) and myosin motor motility (19, 20). Thus, although it has not been presented in this thesis due to the lack of time, we also have successfully applied our algorithm to another dataset obtained from optical tweezers experiments on myosin motors (19). In fact, the binding and unbinding kinetics of the actin- myosin interactions obtained by our algorithm are similar to those reported by the authors, highlighting the strength of our method. However, since the algorithm was implemented in Matlab, its use requires basic knowledge of this programming language. Developing a graphical user interface for this method would make it more accessible to a wider group of researchers without any programming skills.

6.2 Role of shear flow on the lateral organization of ICAM-1 on ECs and its impact on the migration of T-cells

A key factor in the process of leukocyte migration on ECs is the presence of shear forces (21-24). In this thesis we showed that ICAM-1 undergoes to a massive relocation on the cell surface of TNF-α-treated ECs as a consequence of prolonged shear flow exposure. Specifically, we observed that shear flow stimulation induced a strong gradient in the ICAM-1 density distribution on the EC membrane with the highest concentration being located on the region of the EC membrane directly “facing” the impact of the flow. Importantly and independently of their location on the EC membrane, shear flow exposure induced the formation of ICAM-1 nanoclusters. Such changes in the overall distribution and nanoscale organization of ICAM-1 on the EC membrane are most probably driven by actin cytoskeleton re-modeling as a result of shear forces. In this thesis we showed, using confocal and STORM microscopy, the formation of patch-like actin structures enriched with ICAM-1 on the rear region of ECs as a consequence of shear flow stimulation. Moreover, we demonstrated that perturbation of the actin cytoskeleton after shear flow stimulation led to the dissociation ICAM-1 nanoclusters. Thus, our results indicate that flow-induced reorganized actin is required to maintain the nanoclustering of ICAM-1 and further suggest that actin could be involved in the ICAM-1 redistribution on the EC membrane. To further corroborate this hypothesis, a feasible experiment would be the knocking down of the different adaptor proteins that are known to mediate the interaction between ICAM-1 and the actin cytoskeleton, such as α-actinin-4 and cortactin (25, 26). Thus, if our hypothesis is true, these experiments should prevent the formation of ICAM-1 nanoclusters upon shear flow stimulation.

Using a reconstituted fluid lipid bilayer it has been recently demonstrated that depending on actin concentration, filament length, and actin/myosin ratio, actin undergoes different phases of organization, namely, linked, apolar asters and polar asters. In particular, apolar and polar asters curiously resemble our patch-like actin structures (27). In addition, the authors showed that this self-organization of the actin morphology into asters could lead to the clustering of actin-associated membrane components. Thus, the clustering of ICAM-1 observed upon shear flow stimulation could be the result of the actin reorganization in these patch-like structures. Moreover, the fact that we observe a higher concentration of ICAM-1 nanoclusters on the region of the cell that directly face the shear flow is likely because this region has to resist higher stress compared to its opposite side. These higher tensile forces might preferentially alter the balance of actomyosin components such that the phases of actin patches (or asters), which drive the clustering of ICAM-1, are favored. Hence, it would be interesting to experimentally demonstrate this model in our system. Since the recruitment and activity of myosin II is required for the actin asters formation (27), experiments in which we label this molecule simultaneously with the actin cytoskeleton and/or ICAM-1, will provide some evidence to test our hypothesis. Thus, if our model is correct, we should observe colocalization between the actin patches structures and myosin II after 4 hours of shear flow stimulation. Moreover, if the global relocation of ICAM-1 on the EC membrane is driven by the formation of these actin patches structures, we should also observe a gradient of myosin II distribution along ECs from upstream to downstream after shear flow stimulation. In contrast, drugs, such as blebbistatin, affecting the activity of myosin II, should prevent both the formation of the actin patches structures and as a result, the nanoclustering of ICAM-1.

Another interesting finding of this thesis is that pre-exposure of ECs to continuous shear stress modulates the migratory behavior of T-cells. Indeed, we observed that T-cells move faster on ECs pre-exposed to shear flow. Since the migration of leukocytes on the endothelium is mainly mediated by ICAM-1-αLβ2 interactions and the size of ICAM-1 nanoclusters increased upon shear flow stimulation, we hypothesize that a direct link between the increased T-cell velocities and the increased ICAM-1 nanoclustering should exist. To rationalize this apparent connection between ICAM-1 nanoclustering and T-cell migration we appeal to the so-called motor-clutch model (28, 29). In this model the motion of T-cells is determined by the difference between the rates at which F-actin is self-assembled on the cell front and the velocity of F-actin retrograde flow generated by myosin motors pulling rearward. The adhesion molecules and their ligands (as ICAM-1-αLβ2 complex) act as molecular clutches that “sense” the mechanical properties of the extracellular environment by modulating the actin retrograde flow and, therefore, the motion of the cell. Hence, according to this model, there are two main factors affecting the retrograde flow of F-actin, namely the stiffness of the substrate and the strength of the clutches (integrin-ligand bonds). The increase of any of these parameters leads to the reduction in the actin retrograde flow, thus resulting in a faster advance of the cell edge. In the context of our experiments, the increased size of ICAM-1 nanoclusters induced by shear flow would likely strengthen the ICAM-1-αLβ2 bonds, thus reducing actin retrograde flow and increasing the velocity of T cells. To further validate our experimental data additional experiments could be performed. For instance, one could perturb the actin cytoskeleton of ECs after shear flow exposure and track the motion of T-cells on these cytoskeleton compromised ECs. Since we observed that ICAM-1 nanoclusters are abrogated upon cytoskeleton perturbation, we should then observe a reduction in the velocity of T-cell migration due to the weakening of ICAM-1-αLβ2 bonds, with values that should be comparable to those obtained on static ECs.

In addition, according to the motor-clutch model actin retrograde flow can be affected not only by the bond strength but also by changes in the substrate stiffness. In fact, the motor-clutch also predicts the early break of the clutches as a consequence of the increased substrate stiffness, which could explain the reduced time of interaction observed between T-cells and ECs stimulated with shear flow for 4 h. Indeed, previous experiments have shown that the exposure of ECs to 24 h of increasing shear stress leads to a two-fold increase in the EC membrane stiffness (30). However, TNF-α stimulation conditions as used in our experiments induced a similar two-fold increase in the stiffness of ECs in shear-free conditions (31). Since, in our shear-flow experiments involving T cells, ECs were always stimulated with TNF-α, it is unlikely that the exposure to only four hours of shear flow would increase the EC stiffness beyond that induced by TNF-α stimulation. Therefore, we discard the changes in the stiffness of the EC membrane as a possible cause of the different T cell behavior on static and shear-flow stimulated ECs.

However, we observed that ICAM-1 nanoclusters colocalize with regions enriched with actin patch-like structures upon shear flow stimulation. This increased interaction between the actin and ICAM-1 would probably lead to the immobilization of ICAM-1, which would in turn increase the effective local stiffness of the clutches, thus inducing their earlier breaking. Following the mobility of individual ICAM-1 molecules using SPT will directly reveal if indeed immobilization of ICAM-1 occurs as a function of applied shear-flow. Still, one would still have to demonstrate that ICAM-1 immobilization also leads to local increased stiffness of the membrane. Techniques that can directly assess local stiffness, such as AFM, will be of particular interest, but it is difficult to envisage how such techniques could be implemented together with our shear-flow system.

An important point to take into account in the context of these experiments is the fact that TNF-α not only upregulates ICAM-1 but also VCAM-1, although to a much lesser extent (32, 33).

VCAM-1 is also known to play an important role in leukocyte migration across the endothelium by binding to α4β1 integrins on leukocytes, as we described in Chapter 5. Although in this thesis we exclusively focused on the organization of ICAM-1, similar type of experiments could be equally conducted on VCAM-1. In any case, even if VCAM-1 also forms nanoclusters upon shear-flow stimulation by a similar mechanism of actin cytoskeleton interactions (34), the overall model put forward in this thesis would not conceptually change. That is, ligand-integrin clutches (either involving ICAM-1-αLβ2 and/or VCAM-1- α4β1 bonds) would still get re-enforced upon shear-stimulation and be responsible for the increased T cell velocities observed in our experiments. To accurately assess the role of each type of clutch, one could specifically block either VCAM-1 or ICAM-1 prior to T cell adhesion and then determine the effect of the unblocked ligand on T cell velocity and interaction time with the ECs.

6.3 Effect of integrin activators in the spatiotemporal organization of the integrin receptor α4β1

As αLβ2, α4β1 is one of the main integrins mediating the trafficking of leukocytes across the endothelium (35). Its adhesiveness is finely regulated by chemokines released on the sites of injury and infection. Using SPT and super-resolution techniques we have investigated the influence of chemokines and/or ligands stimulation on the spatiotemporal behavior of α4β1 on T-cells. We showed that on resting conditions, α4β1 is highly mobile and exhibited a Brownian diffusion behavior. Moreover, we demonstrated that CXCL12 stimulation induced a rapid and transient immobilization in a percentage of α4β1 integrins while restricting the diffusion of the remaining mobile population. Both findings are most probably consequence of an increasing interaction with the cytoskeleton through talin association. A possible scenario that could explain these results is that the most CXCL12-responsive integrins interact with the cytoskeleton for long periods of time (at least the duration of a typical trajectory), so they are detected as immobile. On the other hand, the remaining integrins -less sensitive to CXCL12 stimulus- shortly interact with the cytoskeleton, thus alternating between periods of Brownian diffusion and periods of immobilization. As a result, given the time resolution of our experiments (16ms/frame) the overall diffusion of trajectories exhibiting this dual diffusive behavior is virtually reduced. Those regions where the molecule remains transiently trapped (attached to the actin cytoskeleton) have been previously referred as to transient confinement zones (TCZ) (36). However, we only observed a very small percentage of TCZs (around 20%) in our experiments. An alternative possibility is that some intracellular adaptors and/or signaling proteins, recruited upon CXCL12 stimulation, might initially bind to the integrin without yet full activation of the integrin and anchoring to the cytoskeleton. As a result, the mobile integrins would have to drag these adaptors proteins reducing their mobility. Experiments using multi-color SPT of the integrin together with different potential adaptors could shed some light into this question. In fact, although many of the molecular actors involved in integrin activation are known, the order of events leading to full integrin activation have not yet been resolved. Multi-color SPT might constitute a key technique to dynamically visualize the architecture of integrin activation and downstream signaling events occurring after activation.

By combining SPT with biochemical experiments we observed a direct correlation between transient α4β1 immobilization and talin association with β1. This is consistent with the known role of talin in the transmission of inside-out signaling induced by chemokines that ends with the activation of integrins (37). In this context, dual color experiments of the integrin together with talin would unequivocally demonstrate if talin recruitment to β1 directly colocalizes with immobile integrins. In addition, SPT experiments knocking down the talin protein or perturbing the cytoskeleton may provide direct evidence to confirm that the observed immobilization of α4β1 is a consequence of the anchorage to actin cytoskeleton through talin recruitment. Moreover, it would be also interesting to investigate the role of other adaptors proteins such as kindlin-3 (38) in the dynamics of α4β1.

We also showed in this thesis that soluble VCAM-1 is capable of inducing the high-affinity state of α4β1 beyond the one induced by CXCL12, without significantly affecting the overall mobility of the integrin. These results suggest the existence of a conformational state in which the integrin is bound to its ligand but not to the actin cytoskeleton, thus remaining mobile. This is in contrast to others integrins such as αLβ2, in which monomeric soluble ligands are not sufficient to induce the high affinity state of the integrin (39). Moreover, previous studies have shown that in absence of inside-out stimulation, the ligand binding rate of α4β1 is 10 times faster than for αLβ2 (40), indicating that contrary to αLβ2, α4β1 in the bent conformation might be able to bind to its ligand. This enhanced binding capability of α4β1 respect to αLβ2 may have its origin in the structural differences between both integrins, due to the lack of the αI domain on the first one (40). In addition, our experiments showed that co-stimulation with CXCL12 and VCAM-1 further increased the percentage of immobilized α4β1 and the number of high-affinity integrins as compared to each individual stimulus. Moreover, the high-affinity form of the integrin was kept for longer time in the case of co-stimulation as compared to the application of individual stimuli. These findings therefore suggest that while chemokines are required for rapid α4β1 activation, ligands play a major role in stabilizing the high-affinity conformation.

In contrast to soluble VCAM-1, the use of fixed VCAM-1 led to a dramatic immobilization of α4β1 integrins together with an important reduction in the diffusion of the remaining mobiles. We rationalized these results based on a traction force model (39) in which the mechanical forces being exerted between the diffusing integrins and the fixed ligands contribute to stabilize the high affinity of the integrin, reinforcing the strength of α4β1-VCAM-1 interactions. This force-induced integrin activation leads to the anchorage to the cytoskeleton and its consequent immobilization. To validate this traction force model one could perform similar experiments using artificial lipid bilayers where the diffusion of ICAM-1 molecules can be controlled. If our model is correct, SPT experiments with T-cells attached to this type of substrates should reveal changes in the mobility of α4β1 that are directly related to the degree of freedom of the underlying ligand.

In our STED experiments we did not observe increased nanoclustering upon activation of α4β1 although we did find a small but significant reduction in the distance between individual α4β1 molecules upon activation. This increased proximity is fully in line with the increase in the number of molecules with an active conformation as observed in the confocal staining upon the same type of stimulation conditions (CXCL12, ligand, combination). These results are remarkably different to those observed in focal adhesions (FAs), in which integrins organize in large clusters and their immobilization is long-lived (41). From the functional point of view, the absence of large clusters of active integrins as observed in our case, could facilitate dynamic interactions between integrins and ligands, which is required for effective T-cell migration. Along the same lines, cells that form FAs can establish stronger adhesion between integrins and ligands and move using different type of migration patterns as compared to cells of the immune system. Interestingly, both types of cells are equipped with the same molecular machinery required for cell adhesion and migration, indicating that integrin cluster size might be a key modulator for these processes. In this framework, an important question that remains open is what molecular and/or physical factors regulate the clustering of integrins in different cell types and with different functions. A long way still will have to be traveled before answering this fundamental question. Indeed, the use and development of new biophysical techniques as those presented in this thesis will play a major role in unrevealing this question.

6.4 References

1. Luster A. D., Alon R., and von Andrian U. H., Immune cell migration in inflammation: present and future therapeutic targets. *Nat. Immunol.,* (2005) **6**, 1182-1190.
2. Ley K., Laudanna C., Cybulsky M. I., and Nourshargh S., Getting to the site of inflammation: the leukocyte adhesion cascade updated. *Nat. Rev. Immunol.,* (2007) **7**, 678-689.
3. Laudanna C., Kim J. Y., Constantin G., and Butcher E. C., Rapid leukocyte integrin activation by chemokines. *Immunol. Rev.,* (2002) **186**, 37-46.
4. Thelen M. and Stein J. V., How chemokines invite leukocytes to dance. *Nat. Immunol.,* (2008) **9**, 953-959.
5. Walling M. A., Novak J. A., and Shepard J. R. E., (2009) Quantum Dots for Live Cell and In Vivo Imaging. *Int. J. Mol. Sci.* , (2009) **10**, 441-491.
6. Nirmal M., Dabbousi B. O., Bawendi M. G., Macklin J. J., Trautman J. K., Harris T. D., and Brus L. E., Fluorescence intermittency in single cadmium selenide nanocrystals. *Nature,* (1996) **383**, 802-804.
7. M. Kuno, Fromm D. P., Hamann H. F., Gallagher A., and Nesbitt D. J., Nonexponential “blinking” kinetics of single CdSe quantum dots: A universal power law behavior. *J. Chem. Phys.* , (2000) **112**, 3117.
8. Resch-Genger U., Grabolle M., Cavaliere-Jaricot S., Nitschke R., and Nann T., Quantum dots versus organic dyes as fluorescent labels. *Nat. Methods,* (2008) **5**, 763-775.
9. DeVore M. S., Stich D. G., Keller A. M., Ghosh Y., Goodwin P. M., Phipps M. E., Stewart M. H., Cleyrat C., Wilson B. S., Lidke D. S., Hollingsworth J. A., and Werner J. H., Three dimensional time-gated tracking of non-blinking quantum dots in live cells. *Proceedings of SPIE,* (2015) **9338**, 933812.
10. Marchuk K., Guo Y., Sun W., Vela J., and Fang N., High-Precision Tracking with Non-blinking Quantum Dots Resolves Nanoscale Vertical Displacement. *J. Am. Chem. Soc.,* (2012) **134**, 6108-6111.
11. Cairo C. W., Rossen M., Golan D. E. , Cytoskeletal Regulation Couples LFA-1 Conformational Changes to Receptor Lateral Mobility and Clustering. *Immunity* (2006) **25**, 297–308.
12. Bakker G. J., Eich C., Torreno-Pina J. A., Diez-Ahedo R., Perez-Sampera G., van Zanten T. S., Figdor C. G., Cambi A. , Garcia-Parajo M. F., Lateral mobility of

individual integrin nanoclusters orchestrates the onset for leukocyte adhesion. *Proc. Natl. Acad. Sci. USA*, (2012) **109**, 4869–4874.

13. Whitesides G. M., The origins and the future of microfluidics. *Nature*, (2006) **442**, 368-373.
14. Halldorsson S., Lucumi E., Gómez-Sjöberg R., and Fleming R. M. T., Advantages and challenges of microfluidic cell culture in polydimethylsiloxane devices. *Biosens. Bioelectron*., (2015) **63**, 218-231.
15. Cambi A., Joosten B., Koopman M., de Lange F., Beeren I., Torensma R., Fransen J.A., Garcia-Parajó M., van Leeuwen F.N., and Figdor C.G., Organization of the Integrin LFA-1 in Nanoclusters Regulates Its Activity. *Mol. Biol. Cell*, (2006) **17**, 4270-4281.
16. van Zanten T. S., Cambi A., Koopman M., Joosten B., Figdor C. G., and Garcia-Parajo M.F., Hotspots of GPI-anchored proteins and integrin nanoclusters function as nucleation sites for cell adhesion. *Proc. Natl. Acad. Sci. USA*, (2009) **106**, 18557-18562.
17. Keogh E. J., Chu S., Hart D., and Pazzani M. J., An Online Algorithm for Segmenting Time Series, *Proc. of the IEEE International Conference on Data Mining*. (2001) 289-296.
18. Haber C. and Wirtz D., Magnetic tweezers for DNA micromanipulation. *Rev. Sci. Instrum*., (2000) **71**, 4561-4570.
19. Capitanio M., Canepari M., Maffei M., Beneventi D., Monico C., Vanzi F., Bottinelli R., and Pavone F. S., Ultrafast force-clamp spectroscopy of single molecules reveals load dependence of myosin working stroke. *Na.t Methods*, (2012) **9**, 1013-1019.
20. Yildiz A., Forkey J. N., McKinney S. A., Ha T., Goldman Y. E., and Selvin P. R., Myosin V Walks Hand-Over-Hand: Single Fluorophore Imaging with 1.5-nm Localization. *Science*, (2003) **300**, 2061.
21. Tsuboi H., Ando J., Korenaga R., Takada Y., and Kamiya A., Flow Stimulates ICAM-1 Expression Time and Shear Stress Dependently in Cultured Human Endothelial Cells. *Biochem. Biophys. Res. Commun.*, (1995) **206**, 988-996.
22. Nagel T., Resnick N., Atkinson W. J., Dewey C. F., Jr., and Gimbrone M. A. Jr. Shear stress selectively upregulates intercellular adhesion molecule-1 expression in cultured human vascular endothelial cells. *J. Clin. Invest.*, (1994) **94**, 885-891.
23. Wojciak-Stothard B. and Ridley A. J., Shear stress–induced endothelial cell polarization is mediated by Rho and Rac but not Cdc42 or PI 3-kinases. *J. Cell Biol*., (2003) **161**, 429.

24. Campbell J. J., Hedrick J., Zlotnik A., Siani M. A., Thompson D. A., and Butcher E. C., Chemokines and the Arrest of Lymphocytes Rolling Under Flow Conditions. *Science,* (1998) **279**, 381.

25. Schaefer A., te Riet J., Ritz K., Hoogenboezem M., Anthony E. C., Mul F. P. J., de Vries C. J., Daemen M. J., Figdor C. G., van Buul J. D., and Hordijk P. L., Actin-binding proteins differentially regulate endothelial cell stiffness, ICAM-1 function and neutrophil transmigration. *J. Cell Sci.*, (2014) **127**, 4470-4482

26. Carpen O., Pallai P., Staunton D. E., and Springer T. A., Association of intercellular adhesion molecule-1 (ICAM-1) with actin-containing cytoskeleton and alpha-actinin. *J. Cell Bio.l*, (1992) **118**, 1223-34.

27. Köster D. V., Husain K., Iljazi E., Bhat A., Bieling P., Mullins R. D., Rao M., and Mayor S., Actomyosin dynamics drive local membrane component organization in an in vitro active composite layer. *Proc. Natl. Acad. Sci. USA*, (2016) **113**, E1645-E1654.

28. Bangasser B. L. and Odde D. J., Master equation-based analysis of a motor-clutch model for cell traction force. *Cell Mol. Bioeng.*, (2013) **6**, 449-459.

29. Bangasser B. L., Rosenfeld S. S., and Odde D. J., Determinants of Maximal Force Transmission in a Motor-Clutch Model of Cell Traction in a Compliant Microenvironment. *Biophys. J.*, (2013) **105**, 581-592.

30. Mathur A. B., Reichert W. M., and Truskey G. A., Flow and High Affinity Binding Affect the Elastic Modulus of the Nucleus, Cell Body and the Stress Fibers of Endothelial Cells. *Ann. Biomed. Eng.*, (2007) **35**, 1120-1130.

31. Lee S.-Y., Zaske A.-M., Novellino T., Danila D., Ferrari M., Conyers J., and Decuzzi P., Probing the mechanical properties of TNF-α stimulated endothelial cell with atomic force microscopy. *Int. J. Nanomedicine,* (2011) **6**, 179-195.

32. Zhou Z., Liu Y., Miao A.-D., and Wang S.-Q., Protocatechuic aldehyde suppresses TNF-α-induced ICAM-1 and VCAM-1 expression in human umbilical vein endothelial cells. *Eur. J. Pharmacol.*, (2005) **513**, 1-8.

33. Qi Y., Liang J., She Z.-G., Cai Y., Wang J., Lei T., Stallcup W. B., and Fu M., MCP-induced protein 1 suppresses TNFα-induced VCAM-1 expression in human endothelial cells. *FEBS letters*, (2010) **584**, 3065-3072.

34. Barreiro O., Yáñez-Mó M., Serrador J. M., Montoya M. C., Vicente-Manzanares M., Tejedor R., Furthmayr H., and Sánchez-Madrid F., Dynamic interaction of VCAM-1 and ICAM-1 with moesin and ezrin in a novel endothelial docking structure for adherent leukocytes. *J. Cell Biol.*, (2002) **157**, 1233-1245.

35. Alon R., Kassner P. D., Carr M. W., Finger E. B., Hemler M. E., and Springer T. A., The integrin VLA-4 supports tethering and rolling in flow on VCAM-1. *J. Cell Biol.*, (1995) **128**, 1243.

36. Chen Y., Yang B., and Jacobson K., Transient confinement zones: A type of lipid raft? *Lipids*, (2004) **39**, 1115-1119.

37. Tadokoro S., Shattil S. J., Eto K., Tai V., Liddington R. C., de Pereda J. M., Ginsberg M. H., and Calderwood D. A., Talin Binding to Integrin ß Tails: A Final Common Step in Integrin Activation. *Science*, (2003) **302**, 103-106.

38. Moser M., Nieswandt B., Ussar S., Pozgajova M., and Fassler R., Kindlin-3 is essential for integrin activation and platelet aggregation. *Nat. Med.*, (2008) **14**, 325-330.

39. Schürpf T. and Springer,T. A., Regulation of integrin affinity on cell surfaces. *EMBO J.*, (2011) **30**, 4712-4227.

40. Chigaev A. and Sklar L. A., Aspects of VLA-4 and LFA-1 regulation that may contribute to rolling and firm adhesion. *Front. Immunol.*, (2012) **3**, 44-52.

41. Rossier O., Octeau V., Sibarita J.-B., Leduc C., Tessier B., Nair D., Gatterdam V., Destaing O., Albigès-Rizo C., Tampé R., Cognet L., Choquet D., Lounis B., and Giannone G., Integrins β1 and β3 exhibit distinct dynamic nanoscale organizations inside focal adhesions. *Nat. Cell Biol.*, (2012) **14**, 1057-1067.